PHYSICS REPORTS (Review Section of Physics Letters) 238, No. 4 (1994) 173–243.
North-Holland

PHYSICS REPORTS

Spin-polarized electron tunneling

R. Meservey and P.M. Tedrow

Francis Bitter National Magnet Laboratory, Massachusetts Institute of Technology, Cambridge, MA 02139, USA

Received September 1993; editor: J.I. Budnick

Contents:

1. Introduction 175
   1.1. Superconducting behavior in a magnetic field 175
   1.2. Electron tunneling spectroscopy 176
   1.3. Fabrication of tunnel junctions 180
   1.4. Design of this review 182
2. Spin paramagnetism in superconductors 182
   2.1. Critical magnetic field of Al thin films 182
   2.2. Fluctuations 185
   2.3. Zeeman splitting of the density of states 187
   2.4. Spin–orbit scattering 190
   2.5. Spin–orbit scattering and weak localization 199
3. Metallic ferromagnets 200
   3.1. Measurements of 3d transition metals 200
   3.2. Interpretation of the 3d tunneling results 208
   3.3. Rare-earth metals 211
   3.4. Ultra-thin films of ferromagnets 212
   3.5. Single-crystal experiments and artificial tunnel barriers 213
   3.6. Tunneling between ferromagnets 214
4. Fermi-liquid effects 217
5. Exchange effects at interfaces and barriers 222
   5.1. Exchange interaction proximity effects 222
   5.2. Spin-filter tunnel barriers 229
6. Relation to other techniques 235
   6.1. Field emission 235
   6.2. Photoemission 235
   6.3. Electron capture spectroscopy 236
   6.4. Secondary electron emission 236
   6.5. Spin-polarized metastable-atom de-excitation spectroscopy 237
   6.6. Photodetection of injected electron spins 237
7. Summary 237
8. Future directions 238
References 239

SSDI 0370-1573(93)E0051-O

SPIN-POLARIZED ELECTRON TUNNELING

R. MESERVEY and P.M. TEDROW

Francis Bitter National Magnet Laboratory, Massachusetts Institute of Technology, Cambridge, MA 02139, USA

NORTH-HOLLAND

1. Introduction

Spin-polarized electron tunneling is an experimental technique which has used special properties of the superconducting state to probe spin-dependent features of the electron density of states of superconductors, magnetic metals, and magnetic semiconductors. The development of this technique and application of the method to the study of various superconducting or magnetic systems are described here from an experimental point of view. Brief summaries of theoretical ideas are presented as needed for an understanding of the various experiments; detailed theoretical treatment of these topics is provided by the references. A review by Fulde [1] describes earlier work on spin-polarized electron tunneling and much of the theory of spin effects in superconductors. Wolf [2] gives an extensive review of the general field of electron tunneling spectroscopy. Books by Burstein and Lundqvist [3] and Duke [4] are sources of earlier work on tunneling in solids. Conventional superconductivity is treated in books by Tinkham [5], Rickayzen [6], de Gennes [7], and Schrieffer [8]; *Superconductivity*, edited by Parks [9], is still an excellent reference. Discussions of superconductivity from a more applied point of view can be found in books by Solymar [10], Van Duzer and Turner [11] and by Delin and Orlando [12].

Because an understanding of the experiments requires some knowledge of electron tunneling and of the response of superconductors to applied magnetic fields, a brief discussion of these topics is included in the introduction. In addition, some basic concepts of the Bardeen–Cooper–Schriefer (BCS) [13] theory of superconductivity are required, such as singlet pairing, the energy gap in the density of electron states, the coherence length, and the magnetic penetration depth. In this review, mostly superconductors that are known to be of the conventional BCS type are considered, since in the more recently discovered high-temperature or heavy-fermion superconductors, spin effects are not well understood or have not yet been observed experimentally.

1.1. Superconducting behavior in a magnetic field

In discussing the response of superconductors to a magnetic field it is useful to divide the materials into two classes, type I and type II. The type I materials are usually pure single-element metals, which can have a relatively long electron mean free path l, and a low transition temperature in zero field, T_{c0}. When placed in a magnetic field, these materials support a surface current that generates a magnetic field which cancels the applied field within the body of the superconductor. The current flows in a surface layer whose thickness, the penetration depth λ, is the depth to which the external field penetrates into the superconductor. At some critical value of the applied magnetic field $H_c(T)$, the energy associated with this surface current equals the condensation energy of the superconducting state at the temperature T, the surface current disappears, and the superconductor reverts to the normal state via a first-order transition. Type I superconductors are characterized by a penetration depth λ which is shorter than the coherence length ξ. The coherence length is a measure of the average size of the electron pairs and the minimum length scale over which the superconducting wave function can change. It is roughly proportional to T_{c0}^{-1} and can range from about a nanometer to a micrometer.

Type II materials are generally alloys, compounds, or dirty (short mean free path) materials in which $\lambda > \xi$. When the applied field exceeds a value H_{c1}, these materials admit the external field in

the form of units of magnetic flux called vortices. These vortices have a normal core with a diameter $\approx \xi$ and a distribution of circulating currents surrounding the core which has a characteristic size given by λ. As the field increases, more vortices enter until the cores are close packed. At that field, the superconductor becomes normal via a second-order transition. Since the vortices each contain one quantum of magnetic flux $\phi_0 = h/2e$, the critical field for $T \ll T_{c0}$ is

$$H_{c2} \approx \phi_0/2\pi\xi^2 \,. \tag{1}$$

Type II materials generally have much higher critical fields than type I materials for the same value of T_{c0}. A description of the energetics involved in type I and type II behavior can be found in refs. [5–12] and in many elementary solid state physics texts. The critical fields in bulk materials and thin films are often best calculated by using the phenomenological equations of the Ginzburg–Landau theory [5, 7, 9, 14] which preceded the microscopic theory.

Thus far in the discussion, we have considered only the interaction between the field and the motion of the electrons. If the critical field is high enough, however, the interaction between the field and the spin magnetic moment μ of the electrons must be taken into account. If $\mu H_{c2} \geq kT_{c0}$, the spin energy is comparable to the superconducting condensation energy when a field near the critical value is applied. It is materials that fall into this regime that are of interest for this review.

A further complication arises if the superconductors are in thin-film form. If the film thickness d is less than the penetration depth λ and the field is applied in the plane of the film, the Meissner [15] screening currents are greatly reduced and the field penetrates the film nearly uniformly. As a result, the critical field $H_{c2\parallel}$ can be much higher than for a bulk sample of the same material. These additional spin and thin-film effects on the response of a superconductor to an applied magnetic field will be discussed more fully in section 2.

1.2. Electron tunneling spectroscopy

The tunneling experiments of Giaever [16] in 1960 followed by those of Shapiro et al. [17] introduced a technique which has proved to be an extremely powerful and subtle probe of the superconducting state. The theoretical justification of Giaever's intuitive interpretation of the experimental results was furnished by Bardeen [18]. An introductory sketch of the phenomenological theory and experimental technique is presented here.

Electron tunneling is a quantum phenomenon in which electric current can pass from one electrode through a thin insulating barrier layer into a second electrode. This three-layer system – electrode, barrier, and counterelectrode – is referred to as a tunnel junction. For technical reasons, these junctions usually have been fabricated using a thin metal film as the first electrode with an oxide providing the barrier. Although other geometries are possible, most of the significant spin-polarized tunneling effects have been observed in planar thin-film junctions.

The quantity usually measured in a tunneling experiment is the current or its derivative as a function of applied voltage. The starting point for the calculation of the tunnel current is similar to that used in describing semiconductor junctions. With no voltage applied, the Fermi levels of the two electrodes must be equal. An applied voltage manifests itself as a difference in energy between the two Fermi levels. The current is found using Fermi's golden rule; that is, the number of electrons tunneling is given by the product of the density of filled states at a given energy in one electrode and the density of empty states in the other electrode at the same energy multiplied by the square of a matrix element describing the probability of tunneling. Usually, this matrix element is

taken to be independent of energy. Because the energies involved in superconductivity are only of the order of millivolts, while the oxide barriers are usually a few volts in height, any change in the barrier with voltage is ignored, in contrast to the semiconductor case where the bias voltages are much larger. For this model, [2, 3, 16] the current of tunneling electrons at energy E flowing from electrode 1 to electrode 2 is then,

$$I_+(V, E) \sim N_1(E - eV)N_2(E)|M|^2 f(E - eV)[1 - f(E)] . \tag{2a}$$

Here V is the voltage on the first electrode with respect to the second, N_1 and N_2 are the densities of states of the first and second electrodes, and f is the Fermi function, and the energy E is measured from the Fermi energy. Similarly, the tunnel current from electrode 2 to electrode 1 is given by

$$I_-(V, E) \sim N_1(E - eV)N_2(E)|M|^2 [1 - f(E - eV)] f(E) . \tag{2b}$$

Assuming that $|M|^2$ is independent of energy in the region of interest, the total current then is given by $I_+ - I_-$ integrated over all energies which reduces to

$$I(V) \sim |M|^2 \int_{-\infty}^{\infty} N_1 (E - V)\, N_2(E)\, [f(E - V) - f(E)]\, \mathrm{d}E . \tag{3}$$

There are three cases to be considered: (i) both electrodes normal metals, (ii) one electrode normal and one superconducting, and (iii) both superconducting. Remembering that the effect of the applied voltage is to slide the density of states of one electrode past that of the other as the electron potential energy is changed and that electrons tunnel at constant energy from a full state on one side of the barrier to an empty state on the other, one can predict the voltage dependence of the tunneling current with the help of figs. 1–3.

When both electrodes are normal (fig. 1), eq. (3) becomes

$$I \sim N_{n1} N_{n2} \int_{-\infty}^{\infty} f(E - eV) f(E)\, \mathrm{d}E . \tag{4}$$

For $T = 0$, one can easily deduce graphically that eq. (4) gives $I \sim V$, that is, ohmic behavior. Equation (4) can also be evaluated analytically for $T \neq 0$ if V is not too large, and again, $I \sim V$. Using the diagrams in fig. 1, one can see that increasing the bias voltage simply increases the number of full states facing empty states across the insulator, giving a linear increase in current with voltage.

The most important tunneling case for this review arises when one electrode is superconducting and one is normal. The BCS superconducting density of states has a gap in the excitation spectrum of Δ on each side of the Fermi level and characteristic singularities in $N_s(E)$ for $E = \pm \Delta$. The BCS density of states for the superconductor has the form [13]

$$N_s(E) = \begin{cases} (N_n(E)\, E)/(E^2 - \Delta^2)^{1/2} & |E| \geq \Delta , \\ 0 & |E| < \Delta , \end{cases} \tag{5}$$

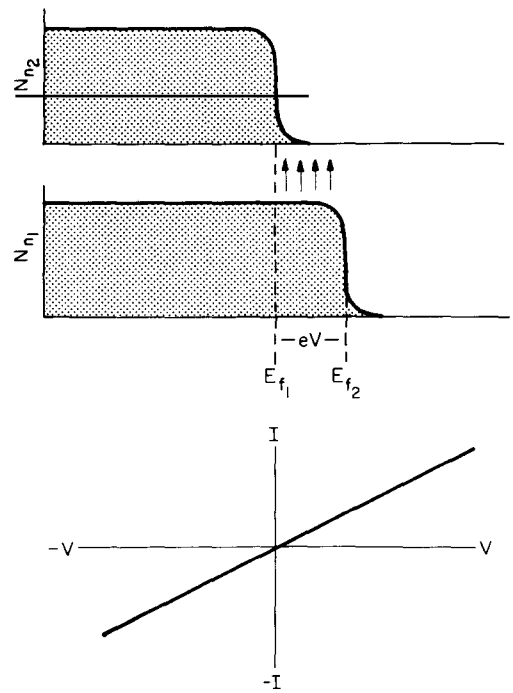

Fig. 1. Schematic representation of the density of states near E_F of two closely spaced normal metals with a potential difference and the resulting linear current–voltage tunneling characteristic.

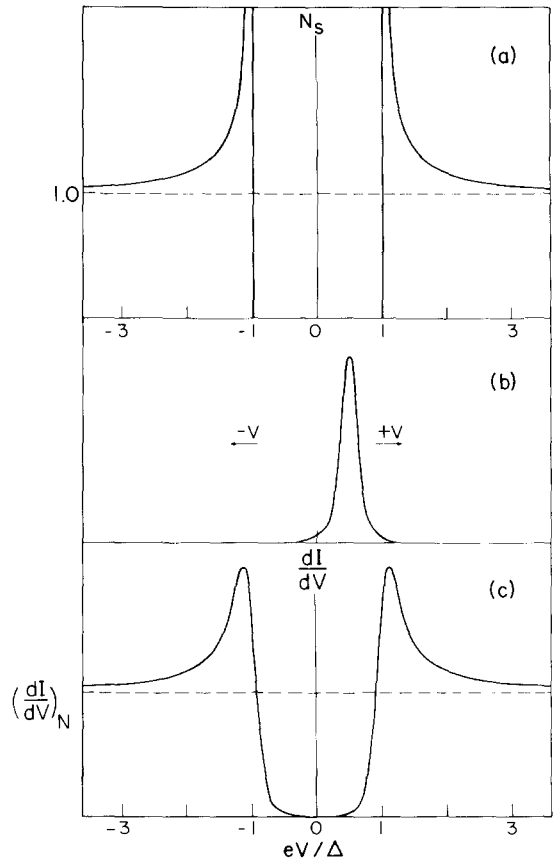

Fig. 2. Superconductor–normal-metal tunneling. (a) BCS density of states of a superconductor as a function of voltage. (b) Temperature-dependent kernel in the integral expression for the conductance. (c) Theoretical normalized conductance dI/dV. Voltage is measured from the Fermi energy of the superconductor. Note that the electron energy decreases as the voltage increases. After [92].

where N_n is the density of states of the metal in the normal state. For simplicity, the normal state density of states is assumed to be independent of energy and can be removed from the integral in eq. (3). In this case, eq. (3) becomes [16]

$$I \sim N_n \int_{-\infty}^{\infty} N_s(E)\,[f(E+eV) - f(E)]\,dE\,. \tag{6}$$

Little current can flow when $|eV| < \Delta$ because there are only a few thermally filled states in one electrode facing a similar number of empty states in the other. When eV exceeds the gap energy, the current rapidly increases. At higher voltages, the current again approaches a linear dependence on V.

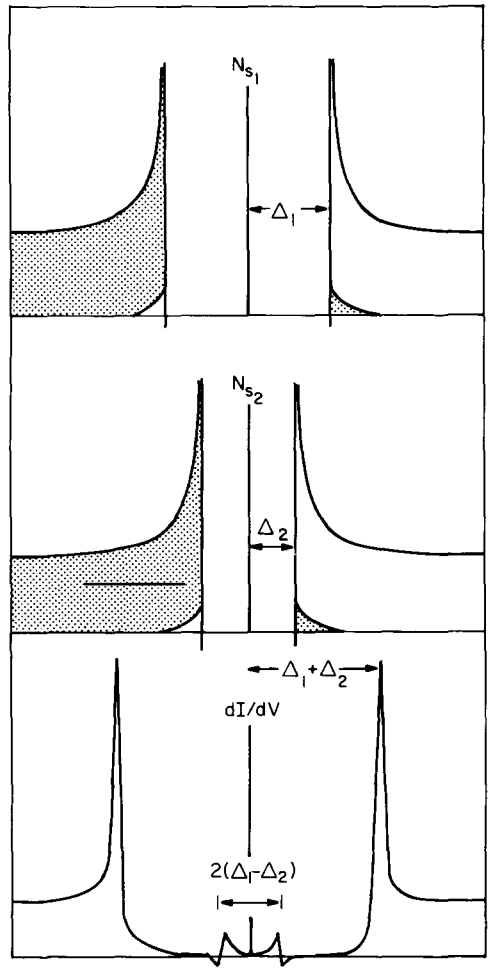

Fig. 3. Semiconductor model of tunneling between two superconductors. The upper diagrams show the density of states near E_F of two superconductors with different energy gaps at a finite temperature well below T_c. The shaded regions correspond to filled electron states. The bottom diagram shows the conductance near E_F as a function of voltage about E_F. At the sum of the half gaps there is a very sharp peak and at the difference of the half gaps there is an inflection point caused by the temperature-excited states.

The importance of this experimental configuration can be appreciated by taking the derivative of I with respect to V in eq. (6). The result can be written in the form

$$\frac{\mathrm{d}I}{\mathrm{d}V}(V) \sim \int_{-\infty}^{\infty} N_s(E) K(E + eV)\,\mathrm{d}E\,. \tag{7}$$

Thus, $\mathrm{d}I/\mathrm{d}V$ is the convolution of the superconducting density of states $N_s(E)$ and $K(E - V)$, the derivative the Fermi function $f(E - eV)$ with respect to V,

$$K = \beta \exp[\beta(E + eV)]/\{1 + \exp[\beta(E + eV)]\}^2\,.$$

Here $\beta = 1/kT$. The function k peaks at $E = eV$ and approaches a δ-function as the temperature $T \to 0$. Thus, in the limit of low temperature, the conductance $dI/dV(V)$ approaches $N_s(V)$ and a measurement of tunneling conductance closely reflects the density of excited states of the superconductor. Indeed, by a deconvolution the density of states can (at least in theory) be reconstructed from the conductance data [19]. Figure 2, based on the semiconductor model of the excited states of a superconductor, shows the directness and power of this sort of measurement.

The third case of interest involves two superconducting electrodes. The mathematics now becomes too involved for this introduction [2, 16, 17] because of the singularities in N_s, so we rely on the semiconductor model. At $T = 0$ no current can flow if $|eV| < (\Delta_1 + \Delta_2)$, one half of the sum of the energy gaps of the two superconductors. For $T \ll T_c$ there is a very small current for $|eV| < (\Delta_1 + \Delta_2)$ and at $|eV| \approx (\Delta_1 + \Delta_2)$ there is a very sharp increase in current. For higher voltages, ohmic behavior is again approached. At higher temperatures, a peak appears in the current at $|eV| \approx (\Delta_1 - \Delta_2)$, the difference of the gap energies. This peak is caused by the presence of thermally excited quasiparticles in the otherwise empty states just above the gap energy and the consequent holes in the filled states just below the gap. These thermally filled and empty states line up at the same energy when the bias voltage reaches $(\Delta_1 - \Delta_2)/e$. Figure 3 again shows the conductance dI/dV that is observed in this sort of measurement. The inflection points are at $|eV| \approx \pm(\Delta_2 - \Delta_1)$ and the very sharp sum peaks are at $eV \approx \pm(\Delta_2 + \Delta_1)$.

Most of the data in this review are in the form of dI/dV plots versus V for S/I/N junctions because they reflect most directly the density of states of the superconductor. However, conductance curves for N/I/N and S/I/S junctions are included in some topics.

1.3. Fabrication of tunnel junctions

The experimental difficulties in making tunnel junctions generally fall into two categories. First, there is the problem of making a barrier that is uniform and free from holes and is not too thick to allow tunneling. The thickness required is of the order of 1–2 nm. The second problem is to make the surface of the superconductor good enough so that the junction characteristics represent the interior properties of the metal and not those of a surface layer whose composition, structure and electrical properties are not well characterized. This requirement for surface quality generally means that any undesirable surface conditions must extend much less than a coherence length into the superconductor. However, for ferromagnetic metals the tolerance to surface degradation is of the order of a monolayer.

These two problems can be solved most easily if the first-deposited electrode forms an oxide layer whose thickness is suitable for tunneling. Aluminium has been the most useful and reliable material because the oxide layer is chemically self-limiting in the tunneling thickness range, besides being uniform and pinhole-free. Tin, indium, and lead are also useful, although more difficult than Al. Compounds and alloys are more challenging. Often an "artificial" barrier must be used, that is, a deposited insulating film not related to the electrode material [2]. Aluminium oxide and amorphous silicon are two materials widely used for this purpose [2, 20, 21]. Materials such as Nb, which has a metallic oxide phase, and magnetic materials, which form magnetic oxide layers, create special problems in barrier formation [2]. When thermal processing constraints are not prohibitive, it is usual to use Al or Pb as the first-deposited electrode and to provide the barrier when more complicated materials are being studied. Compounds and alloys often have short coherence lengths $\lesssim 10$ nm, so the demands on the surface preparation can be severe. The very short coherence lengths in high-T_c compounds are often cited as the reason for the difficulties in tunneling studies of these materials. Nearly all of the junctions described in this review are planar thin-film junctions,

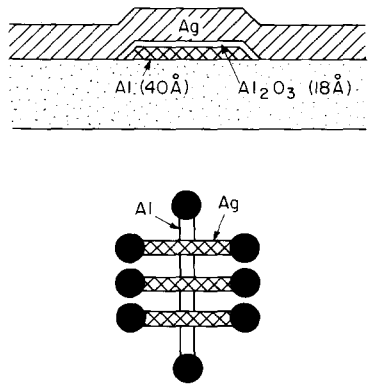

Fig. 4. Cross-section of an $Al/Al_2O_3/Ag$ tunnel junction and plan view of a set of three junctions with contact pads.

and most of them involve Al as one electrode and Al_2O_3 as the barrier. For most of these measurements, the magnetic field must lie as closely as possible in the plane of the tunnel junction to minimize orbital depairing. This alignment is most easily accomplished if a horizontal field is available so that the cryostat can simply be rotated to bring the vertically mounted film sample into coincidence with the field direction. More commonly, however, a vertical solenoid provides the field so that a sample holder with angular adjustment is required.

Typical junction fabrication is as follows. First, an Al film is deposited through a mask to form a long, narrow strip (usually about 0.2 mm wide). Next, the Al film is subjected to an oxygen glow discharge to form the tunnel barrier. Then a counter-electrode material is evaporated through a mask to form a series of cross strips, making a number of junctions. Finally, some material such as In solder or Au is evaporated through a mask to make contact pads at the ends of all the electrodes for attaching wires for the electrical measurements. A schematic representation of a tunnel junction is shown in fig. 4. Variations on this procedure are incorporated to take into account the properties of the materials to be studied. For instance, in many of the experiments reported here, the Al film must be deposited on a substrate cooled to liquid-nitrogen temperature in order to make uniform and continuous 4 nm-thick films.

Many tunneling results have been obtained with circuits which measure the derivatives of I or V [2]. Most of the data presented here are in the form of plots dI/dV as a function of V. These data are obtained by biasing the junction with a voltage source that consists of a slow ramp and a small constant amplitude, audio frequency modulation. The AC current through the junction is measured using a lock-in detector. The output of the lock-in detector is then proportional to dI/dV. Many workers prefer measuring dV/dI, the incremental resistance of the junction, because this technique involves a true four-terminal measurement. Measuring dV/dI requires two current sources, one a slow ramp, and the other a small, constant-amplitude AC signal. The AC voltage across the junction is measured using a lock-in amplifier. The output can then be inverted to yield dI/dV for comparison with theory. The advantage of this technique is that the lead resistance does not enter into the measurement. The disadvantages are that high-resistance junctions are difficult to measure, and features like the difference-of-the-gaps peak in S/I/S tunneling cannot be studied because the voltage becomes a double-valued function of the current and, hence, cannot be resolved using a current bias. In addition, a very large dynamic range is needed to examine both conductance maxima and the gap regions of the tunneling conductance. The disadvantage of the dI/dV technique is that junctions must have resistance much larger than the lead resistance to be measured accurately because the dI/dV measurement is a two-terminal one.

1.4. Design of this review

Because the central body of experimental work described here is the authors' own, the development of each topic has a historical point of view, with complexity and details added as the narrative progresses. We feel that this type of organization presents more clearly the power of the spin-polarized tunneling technique. The required specialized knowledge of superconductivity, magnetism, or experimental methods is introduced with each topic in brief form, along with references to more detailed and rigorous treatments of the material.

2. Spin paramagnetism in superconductors

The BCS theory [13] established that the superconducting electron pairs involved time-reversed states. One consequence of this assumption of $(k\uparrow, -k\downarrow)$ pairing was shown by Yoshida [23] to be that the spin susceptibility χ_s of superconducting electrons should approach zero exponentially as T approaches zero. The vanishing of χ_s implied that the Knight shift should vanish well below T_c. However, the experimental values of the change in Knight shift in Hg by Reif [24] and in Sn by Androes and Knight [25] were found to be very small. In a related theoretical study it was pointed out by Clogston [26] and Chandrasekhar [27] that the spin pairing of the BCS theory implied an upper limit of the critical field called the Pauli or paramagnetic limit H_p, which often was exceeded in high-field superconductors.

To explain why a vanishing of the Knight shift had not been observed in experiments, Ferrell [28] and Anderson [29] introduced the concept of spin–orbit scattering into the theory, a mechanism which could eliminate the effect of superconductivity on the normal-state paramagnetism without destroying the time-reversal invariance of the superconducting state. The mathematical technique of incorporating spin–orbit scattering into the microscopic theory was provided by Abrikosov and Gor'kov (AG) [30] and was applied to the critical field of type II superconductors by Maki [31] and Werthamer et al. [32]. The AG theory suggested that spin–orbit scattering should increase approximately as Z^4, where Z is the atomic number of the superconducting element. For this reason Al was expected to have strong spin effects similar to those implied by the BCS theory. Indeed Hammond and Kelly [33] and later Fine et al. [34] observed in Al a substantial fraction of the knight shift change predicted by Yoshida [23].

2.1. Critical magnetic field of Al thin films

These earlier experiments and theory suggested that measurements of the critical field of thin Al films might be a crucial test of the microscopic theory including spin effects. It is ironic that aluminium should prove to be the ideal material for elucidating the spin properties of high-field superconductors. Its transition temperature T_c is only 1.18 K and its critical field in bulk is about 100 g! However, the confluence of several material properties make Al unique in its suitability for this high-field study. Aluminium films can be made as thin as 4 nm with little difficulty, and the fact that for such thin films $T_c = 2.5$ K [35, 36] allows low reduced temperatures to be reached without the need of dilution refrigeration. For such thin films the critical field increases by orders of magnitude to allow measurements in substantial magnetic fields (see fig. 5) [35, 37]. In addition, the electrons in Al have long spin lifetimes, [38] allowing the full range of spin effects to be studied. Of great importance is the fact that the self-limiting oxide thickness of Al is ideally suited to making

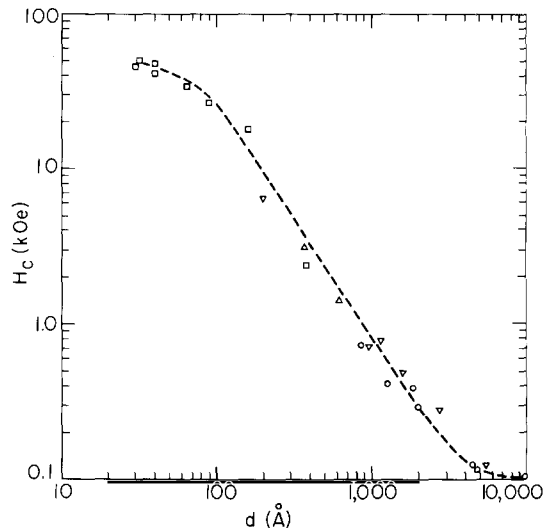

Fig. 5. Critical magnetic field $H_{c_\parallel}$ of Al thin films as a function of d. The dashed line has a slope of $-3/2$ in the region from 2000 to 200 Å [35].

tunnel junctions. Finally, being a pure element, films of Al can be repeatedly and reproducibly made without extensive metallurgical experience or equipment.

The most familiar response of a superconductor to a magnetic field is the Meissner effect [15] in which circulating currents are established, much like eddy currents in a normal conductor. These currents, being non-dissipative, raise the free energy of the superconductor and lead to the critical field. For superconducting films of thickness d, when $d \ll \lambda$ and $d < \xi$, a magnetic field parallel to the plane of the film penetrates the film almost uniformly and the screening currents are minimal. From a microscopic point of view, the magnetic field breaks the time-reversal symmetry and tends to break up superconducting pairs. Maki [31, 39] showed that in the short-mean-free-path limit the strength of an interaction detrimental to superconductivity can be included in the theory in terms of the depairing parameter α. In thin films, the orbital depairing parameter α has two forms depending on whether the field is parallel or perpendicular to the film plane. Thus $\alpha_{\text{perp}} = eDH/3$ while $\alpha_{\text{parallel}} = e^2d^2DH^2/6\hbar$ [1, 39, 40]. When the thickness and the mean free path l (and hence the diffusion constant $D = v_F l/3$) are small, α_{parallel} is small and $H_{c2\parallel}$ becomes large. Here Δ is the superconducting order parameter and v_F the Fermi velocity. In this case the qualitative criterion for the critical field is that there is one flux quantum in an area $\approx \xi d$. In addition, if the mean free path $l \ll \xi_0$ and $l \approx d$, then $\xi \approx (\xi_0 d)^{1/2}$, where $\xi_0 = \hbar v_F/\pi\Delta$. Thus eq. (1) becomes

$$H_{c2\parallel} \approx \frac{\phi_0}{2\pi\xi_0^{1/2}d^{3/2}} \,. \tag{8}$$

Figure 5 shows that the $d^{-3/2}$ dependence of $H_{c\parallel}$ predicted by eq. (8) was found in Al films from 200 to 10 nm, but for the thinnest films $H_{c2\parallel}$ becomes independent of d [35]. At $d = 4$ nm, $H_{c2\parallel} = 4.8$ T, whereas, for orbital effects only, we would expect $H_{c2\parallel} \approx 20$ T. This limitation in $H_{c2\parallel}$ is mainly attributable to the electron-spin magnetic moment.

In the very thin film limit, $d \ll \lambda$, the orbital effects of screening currents become small, and electron spin effects can dominate. Clogston [26] and Chandrasekhar [27] proposed that when an

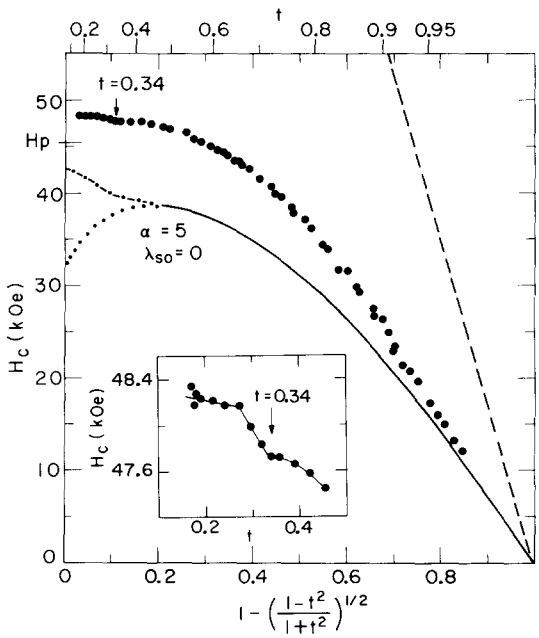

Fig. 6. Experimental values of H_c for a 5 nm Al film as a function of $1 - [(1 - t^2)/(1 + t^2)]^{1/2}$ (the two-fluid temperature dependence). Corresponding values of $t = T/T_c$ are shown at the top of the figure. Dashed line assumes $d^{-3/2}$ dependence of $H_{c\parallel}$ and no paramagnetic limiting. Solid line is the theoretical second-order transition curve for $\alpha = 5$, $\lambda_{so} = 0$; dash-dotted line, first-order transition; dotted line, supercooling field curve. The inset shows the small, but sudden increase at $t = 0.34$ that probably marks the first-order transition [45].

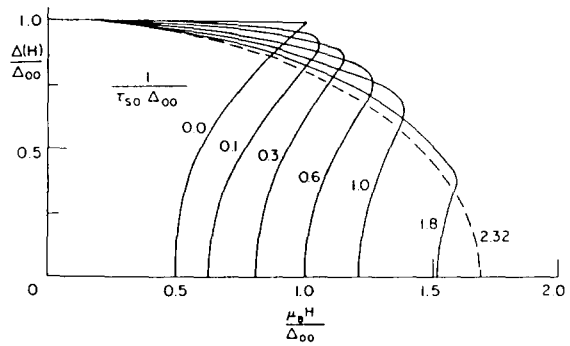

Fig. 7. Theoretical field dependence of the order parameter as a function of spin–orbit scattering. For $1/\tau_{so}\Delta < 2.32$ the order parameter is double valued due to the first-order nature of the transition giving rise to a superheating and supercooling transition as well as the thermodynamic transition. After [50].

applied magnetic field acting on the magnetic moments of the electrons lowers the energy of the paramagnetic normal state by an amount equal to the superconducting condensation energy, a transition to the normal state should occur. This critical field caused by Pauli paramagnetism is given, at $T = 0$, by

$$H_p = \Delta_0/\sqrt{2}\mu = 1.86 T_{c0} \text{ (teslas)} \tag{9}$$

where $2\Delta_0$ is the energy gap at $T = 0$ and μ is the magnetic moment of the electron. Pauli limiting of H_{c2} was first demonstrated by Strongin and Kammerer [37] by a measurement of $H_{c2\parallel}$ versus T of Al thin films. The effect is also shown in fig. 5 where the critical field at low thickness is caused by Pauli limitation [35]. In this case $H_p = 4.6\,T$ from eq. (10), which agrees qualitatively with H_{c2} as measured at low value of thickness and temperature.

Further theoretical work by Sarma [41] and Maki and Tsuneto [42, 43] showed that the transition to the normal state should be a first-order phase transition at sufficiently low temperature and high magnetic field. The field and temperature at which the order of the transition changes is a tricritical point. The tricritical temperature is denoted T_1 [44]. Measurements of the temperature dependence of H_{c2} of thin Al films (fig. 6) showed the presence of this first-order transition as predicted [45]. Suzuki et al. [46] have made a detailed study of the resistance of thin

Al films as a function of thickness in the neighborhood of the tricritical point. This work demonstrates the movement of the tricritical point with increasing orbital depairing.

The theory was further developed for bulk type II materials by Werthamer et al. (WHH) [32] (see also ref. [47]) and by Maki [31,42,43] to include the temperature dependence of H_{c2} and the effect of spin–orbit scattering. Engler and Fulde [1,40,48,49] extended this work to the tunneling properties of superconducting thin films. Figure 7 shows theoretical values of the order parameter as a function of field and spin–orbit scattering [1,48,50]. In this theory, $H_{c2\parallel}(T)$ is calculated as a function of several parameters: the transition temperature in zero magnetic field, T_{c0}; the normalized spin–orbit scattering rate $b \equiv \hbar/3\Delta\tau_{so}$; and a normalized orbital depairing parameter, $c \equiv e^2d^2D\Delta/6\hbar\mu^2$. (The normalized spin–orbit scattering rate is denoted by λ_{so} in the WHH paper and in most experimental work on bulk materials; $\lambda_{so} \equiv 2\hbar/3\pi kT_{c0}\tau_{so}$ or $\lambda_{so} = 1.12b$ for a BCS superconductor.) [47] Here Δ is the superconducting order parameter and τ_{so} is the spin lifetime caused by spin–orbit scattering. In comparisons of the theory with experiment (see, for instance, Hake [51] and Neuringer and Shapira [52]), the spin–orbit scattering parameter b could not be measured independently and was used only as a fitting parameter. This problem and its resolution are discussed below and in later sections. The theory is only qualitatively correct in this form, because many-body effects have been neglected. Later sections will examine the procedures for obtaining quantitative calculations of the critical field.

2.2. Fluctuations

In the late 1960s, it was realized that thermodynamic fluctuations of the order parameter could play a major role in determining the shape of the resistive transition of a superconducting thin film as it passed from the normal to the superconducting state. Such fluctuation effects had been expected to be small in superconductors because of the large coherence volume ξ_0^3. However, thin films with thickness d much less than ξ_0 were easily made and had a much-reduced coherence volume of $\xi^2 d$, allowing fluctuation effects to be easily observable. Since the temperature-dependent coherence length diverges at $T = T_c$ as $(T - T_c)^{-1/2}$ [53], the quantities affected by fluctuations in thin films tend to diverge with a $(T - T_c)^{-1}$ dependence. This divergence takes place along a second-order phase boundary; since films less than the penetration depth λ have a second-order transition in an applied magnetic field [54], the resistive transition as a function of H at constant T similarly shows fluctuation broadening. This property of thin films then can be used to study the Pauli-limited regime because, as in section 2.1, the phase boundary between the normal and superconducting states for such films is of first order at low T and of second order at high T. Thus, if the resistance R of a film is measured as a function of H at various temperatures, it will show a broadened transition for $T > T_1$, the tricritical temperature, and a much less broadened transition for $T < T_1$.

The theory of the fluctuation conductivity was addressed by Aslamazov and Larkin [55], who found, for a thin film in zero field, a conductivity

$$\sigma_{AL}(\tau) = e/16\hbar\tau d\,, \tag{10}$$

where $\tau = \ln(T/T_c) \simeq (T - T_c)/T_c$ for T not too far from T_c. With a field applied in the plane of the thin film at constant temperature, this expression took the form [56]

$$\sigma_{AL}(H) = \frac{e^2}{2\pi d}\,\frac{3kT}{De^2d^2\,[H^2 - H_c^2(T)]}\,. \tag{11}$$

Another contribution to the fluctuation conductivity described by Maki [57] and Thompson [58] is suppressed at low temperatures and high fields and will not be important for this discussion. Fluctuations in superconductors whose critical field is limited by Pauli paramagnetism was first considered by Fulde and Maki [59]. Aoi et al. extended these results and showed that in the case of a paramagnetically limited film, the d^2 factor in the denominator of the second parenthesis of eq. (11) should be replaced by an expression for effective thickness [53, 60]

$$d^{*2} = d^2 + 3\mu\hbar T_c/De^2H_pT\,. \tag{12}$$

For the thin films used in these studies, the second term is much larger than d^2, so d^{*2} is independent of d and eq. (11) can be written as

$$\sigma_{AL}(H) = \frac{e^2}{2\pi\hbar d}\frac{H_p k T^2}{\mu T_c}\left[H^2 - H_c^2(T)\right]^{-1}\,. \tag{13}$$

Thus the dependence of σ_{AL} on H is not changed in the Pauli-limited case, but the prefactor involving temperature is different from that in eq. (11). Aoi et al. [53] also analyzed the angular dependence of H_c of Pauli-limited superconductors.

The first experimental evidence that there was a change in the order of the phase transition in thin Al films was obtained by Tedrow et al. [45] from measurements of the resistive transition at various temperatures as a function of field applied in the plane of the films. Typical data are shown in fig. 8, where R is plotted against H. For high temperatures, the transitions are quite broad but, for $T \lesssim 1.5$ K, the transitions become sharp, even rising above the curves for higher T. This sudden sharpening of the transition also coincides with the slight rise in H_c at a reduced temperature of 0.34 shown in fig. 6.

For $T < T_1$, the critical field measured by the resistive transition corresponds to the first-order transition; however, the critical field calculated by the Fulde theory (see refs. [1, 48] and references therein) corresponds to the second-order transition which is often called the supercooling field H_{sc} in analogy with similar phenomena in the thermodynamics of fluids. Here, H_{sc} is the lowest field in which the normal state can be microscopically stable at a given temperature. Using the fluctuation phenomena described before, one can measure this supercooling field.

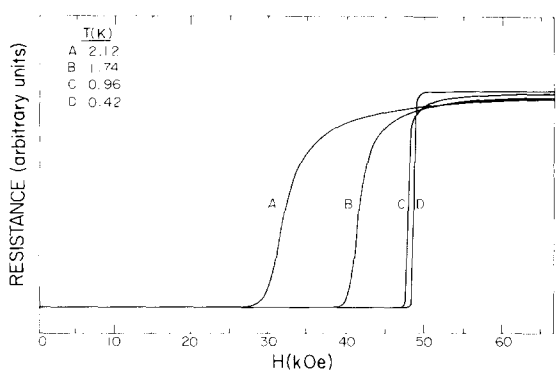

Fig. 8. Recorder traces of R versus H for a 5 nm Al film at several temperatures [45].

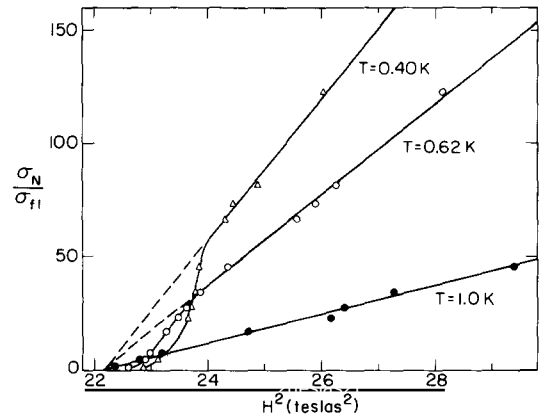

Fig. 9. σ_N/σ_{fl} versus H^2 for a thin Al film at three temperatures. T_1 for this film is 1.08 K [60].

Equation (13) implies that σ_{AL}^{-1} plotted against H^2 is a straight line whose slope varies as T^{-2}. The intercept on the H^2 axis is H_c^2 if T is greater than T_1 and it is H_{sc}^2 for $T < T_1$. To obtain σ_{AL} from raw data such as those shown in fig. 8, a parallel conductance model is used in which the measured conductance $\sigma(H)$ is given by the parallel combination of the (constant) normal-state conductance σ_n and the fluctuation conductance σ_{fl} so that

$$\sigma(H) = \sigma_n + \sigma_{fl} \,. \tag{14}$$

Then

$$\sigma_n/\sigma_{fl} = \sigma_n/[\sigma(H) - \sigma_n] = R(H)/[R_n - R(H)] \,, \tag{15}$$

where the resistances $R(H) = \sigma(H)^{-1}$ and $R_n = \sigma_n^{-1}$ are the quantities actually measured. Figure 9 shows the result of plotting the data such as in fig. 8 in this way [60]. As expected, the data, represented by solid lines, lie on straight lines at high field. The line for $T = 1.0$ K reaches the H^2 axis, but the lines for low temperatures are interrupted by the first-order transition. The extrapolation of these lines to the H^2 axis gives values for H_{sc}^2 which can be plotted on an H versus T diagram as shown in fig. 10. Thus, both the first- and second-order critical fields can be measured, and the second-order field can be compared with theory even for temperatures below T_1. Figure 10 shows a fit of Fulde's critical field theory to the data. We see that the thermodynamic fluctuations of the order parameter, although not fundamentally a spin effect, can be used to probe the spin-paramagnetically-limited state.

2.3. Zeeman splitting of the density of states

Near T_{c0}, the theory predicts that at H_{c2} the transition to the normal state is of second order, whereas at low temperatures the transition is of first order, as discussed in the previous section. The small rapid change in H_{c2} versus T in fig. 6 and the behavior of the fluctuation conductivity in fig. 8 are subtle consequences of this first-order transition. A more convincing test is to measure the energy gap as a function of field at low temperatures. Theory predicts that for $T \ll T_{c0}$ and for no

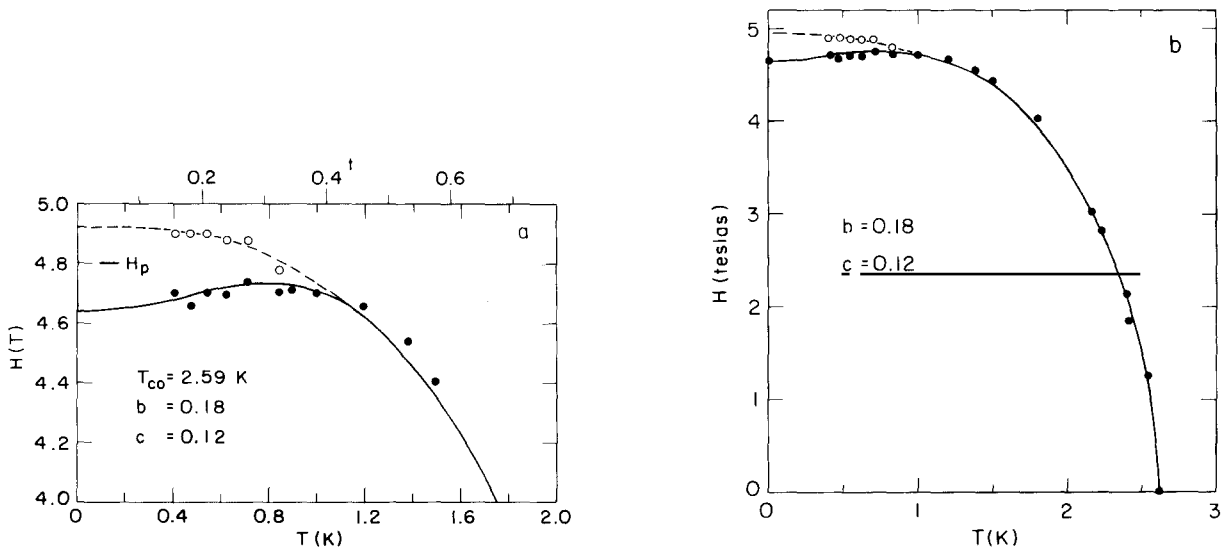

Fig. 10. The measured parallel first-order (open circles) and second-order (full circles) critical fields for the same film as in fig. 9. (a) The low-temperature region showing the supercooling portion of the second-order critical field. (b) The full critical field curve. The solid lines in both (a) and (b) are the theoretical results for $b = 0.18$ and $c = 0.12$ [60].

spin scattering the order parameter and the energy gap should remain essentially constant until the first-order transition is reached at H_{c2}, as shown by the top curve in fig. 7 [50]. The first tunneling experiment to observe this effect found in addition something much more interesting, the Zeeman splitting of the quasiparticle density of states of the superconductor [61].

Generally, in a tunneling experiment in a magnetic field, the orbital depairing parameter dominates and the measured conductance simply reflects a broadening of the density of states with increasing field. In the case of a thin Al film with the magnetic field parallel to the film plane, the orbital response is largely suppressed, as we have seen earlier in connection with the discussion of the critical field. The effect of the spin interaction with the field can then be observed. The energy splitting of the quasiparticle density of states that was first observed by Meservey et al. [61] is shown in fig. 11 [62]. Although the splitting of the density of states was implied by the microscopic theory, the observability of this phenomenon was not anticipated. The unique properties of Al thin films were very important in allowing data such as those shown in fig. 11 to be obtained.

Figure 11 shows that this Zeeman splitting of the density of states peaks as reflected in the conductance of an Al–Al_2O_3–Ag junction at various values of magnetic field H. Figure 12 demonstrates that the energy difference between the split peaks is equal to $2\mu H$ [61], where μ is the magnetic moment of the electron. The semiconductor model diagrams of fig. 13 show how the two-peaked structure develops from the spin density of states in a way very similar to that described in fig. 2. The explanation of the results is that the paired quasiparticles must be in time-reversed states. Thus, when the field is applied, they keep their $k\uparrow, -k\downarrow$ pairing, but now the spin-up and spin-down members of the pair have different energy, one being raised in energy by μH, and the other lowered by μH. The excited states remain separated from the paired state by Δ, so that in a tunneling measurement the peaks of the BCS density of states appear at different voltages for quasiparticles of different spin. This Zeeman splitting of the spin states provided the basis for spin-polarized tunneling, since at an energy of $\Delta - \mu H$ the electrons in the tunnel current

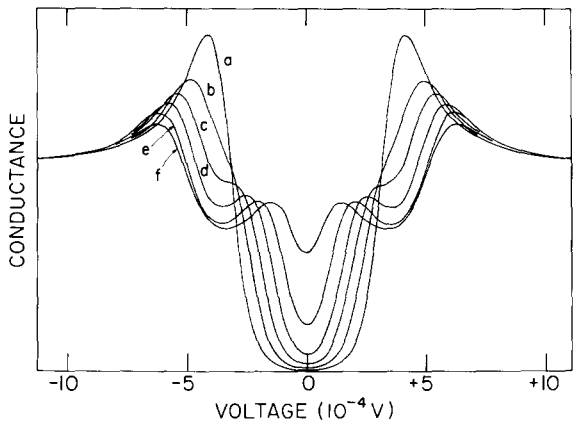

Fig. 11. Conductance versus voltage measurements for an $Al/Al_2O_3/Ag$ tunnel junction at various values of magnetic field H applied parallel to the plane of the films. The symbols on the curves correspond to the values of H in teslas: $a = 0$, $b = 1.5$, $c = 2.24$, $d = 2.99$, $e = 3.72$, and $f = 4.31$ [62].

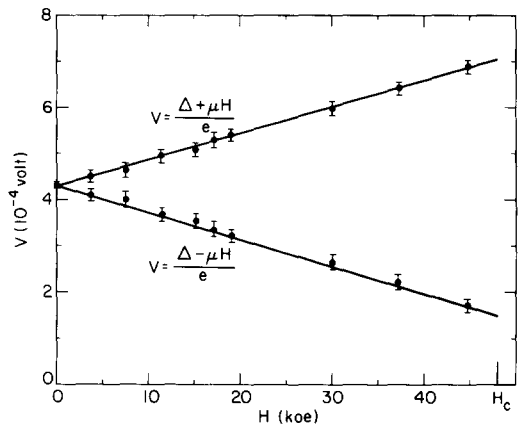

Fig. 12. Voltage corresponding to the maxima of the spin-up and spin-down density-of-states curves of a thin Al film as a function of magnetic field. The line represents the theoretically expected result that $eV = \Delta \pm \mu H$ [61].

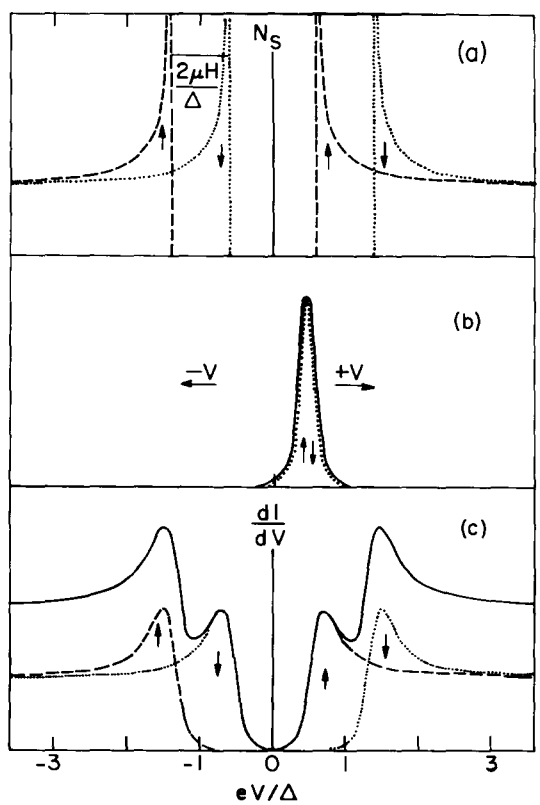

Fig. 13. (a) Magnetic field splitting of the quasiparticle states into spin-up (dashed) and spin-down (dotted) densities. (b) Spin- and temperature-dependent kernel in tunneling current integral. (c) Spin-up conductance (dashed), spin-down conductance (dotted), and total conductance (solid line). After [92].

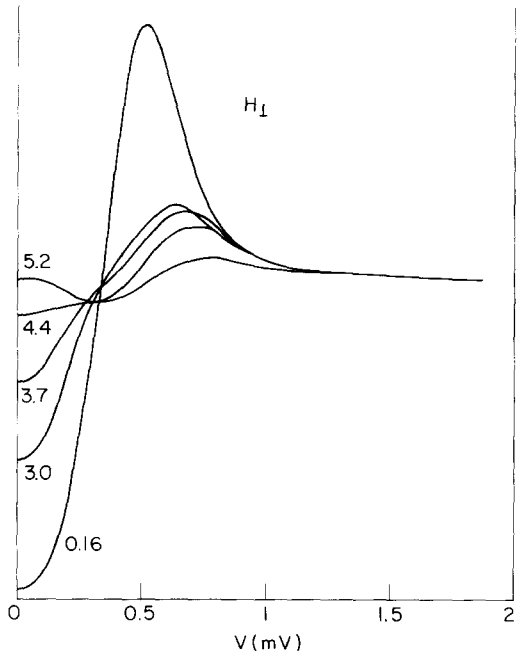

Fig. 14. Tunneling conductance dI/dV versus voltage of V–Ti alloy films for various magnetic fields applied perpendicular to the plane of the films [74].

will be almost entirely of one spin direction and at $-\Delta + \mu H$ almost entirely of the opposite spin direction. To observe this splitting, it is required that α be small in the direction of the applied field and that the spin lifetime of the quasiparticles not be too short.

The main limitation of spin lifetime in systems not containing magnetic impurities is spin–orbit scattering, which will be discussed below. In the absence of spin–orbit scattering and orbital depairing, the measured conductance is the sum of that for each spin in the form of eq. (7):

$$\frac{dI}{dV}(V) \sim \int_{-\infty}^{\infty} N_s(E + \mu H) K(E + eV)\, dE + \int_{-\infty}^{\infty} N_s(E - \mu H) K(E + eV)\, dE . \tag{16}$$

Incidentally, fig. 12 also demonstrates graphically that the transition to the normal state is first order because the order parameter Δ is constant until $H = 0.94 H_{c2}$ and then drops to zero at H_{c2}. Following the discovery of the splitting of the density of states of Al, this effect was observed in a number of other materials which satisfied the conditions mentioned above. An interesting special case involves VTi alloys, which are type II superconductors with small spin–orbit scattering. Here, spin splitting is observed even when the applied field is perpendicular to the plane of the film as shown in fig. 14 [63]. The very short mean free path in the alloy reduces the orbital depairing, allowing the spin splitting to be the dominant part of the magnetic field response.

2.4. *Spin–orbit scattering*

Spin–orbit scattering has already been mentioned in connection with the discussion of the Pauli-limited critical field, H_p. This interaction was first suggested by Ferrell [28] and Anderson

[29] as a way of accounting for the non-vanishing of the Knight shift in superconductors as T is lowered. It also explains why $H_{c2}(0)$ can be far larger than H_p. The qualitative model for the spin–orbit mechanism in superconductors is as follows. Consider an electron moving in a perfect lattice of a conductor. If a non-magnetic impurity is present in the otherwise periodic structure, a distortion of the periodic (in space) electric field will result. This distortion has the effect on the rapidly moving electron of a time-varying magnetic field which can then flip the electron spin. Note that this process is time-reversal invariant, in contrast to scattering by magnetic impurities. Abrikosov and Gorkov [30] (AG) calculated the strength of this process and found that the scattering rate $\tau_{so}^{-1} \sim (e^2Z/\hbar c)^4\tau^{-1}$, where $e^2/\hbar c$ is the fine structure constant and $1/\tau$ is the rate of momentum scattering. This Z^4 dependence explains why Al is a good material for studying spin-dependent properties, while In, Sn and Pb are not; its intrinsic spin–orbit scattering rate is very small. Meservey and Tedrow [38] showed by using a compilation of data for surface spin scattering that the AG expression is a reasonably good representation of the available data when boundary scattering predominates [64]. Gallagher [65] has done a more detailed calculation of $1/\tau_{so}$ and predicts a periodic dependence for the elements superimposed on a rising background.

An important consequence of spin–orbit scattering, the modification of the spin-dependent densities of states of excited quasiparticles, was pointed out by Engler and Fulde [48]. Figure 15 shows the effect of spin–orbit scattering on the spin-split density of states for different values of the normalized spin–orbit scattering rates $b = \hbar/3\Delta\tau_{so}$ in a constant applied field as calculated by Bruno and Schwartz [1, 50]. As b increases, some of the higher-energy spin states are moved down in energy by $\sim 2\mu H$. Thus the higher-energy peak is decreased relative to the lower-energy peak. This process continues as b grows larger, and, at the same time, the energy separation of the peaks decreases. When b exceeds 1 (when the spin–orbit scattering length $l_{so} \lesssim \xi$), the splitting vanishes, and the superconductor behaves as though the quasiparticles had no spin.

Because of the close relationship between the tunneling conductance and the superconducting density of states, spin-polarized tunneling is a powerful method of studying spin–orbit scattering. Detailed theoretical treatments are to be found in the review article by Fulde [1] and in the paper by Bruno and Schwartz [50]. Several types of experiments are possible. First, the tunneling conductance of an S/I/N junction can be measured for various applied fields and the results compared with theoretically computed conductances, allowing the value of b to be determined. Second, an S/I/S junction can be studied. In this case, features appear in the conductance which indicate directly the strength of the normalized spin–orbit scattering rate $b = \hbar/3\Delta\tau_{so}$. Finally, an S/I/F junction can be studied, F being a ferromagnetic metal. This type of experiment, described in detail in section 3, allows the separate spin conductances to be obtained experimentally which can then be compared with theoretical predictions to obtain b. A by-product of these procedures is to give a value for c, the normalized orbital depairing parameter, thus allowing the theoretical critical field to be calculated quantitatively without adjustable parameters using the WHH–Maki–Fulde theory [1, 31, 32, 48]. We will now describe in more detail the first two types of spin-polarized tunneling measurements of b.

The most extensive measurements of b have been made on Al because of the ease of making tunnel junctions, the small intrinsic value of b in Al, the convenient range of H and T involved, and the long coherence length which allows surface "doping" of the thin films. The general experimental procedure is the same as was described earlier for observing the splitting of the density of states. When the conductance of the S/I/N junction as a function of voltage has been obtained, a calculated curve is fitted to the measured one and the value of b is obtained. It is possible to add spin–orbit scattering sites to the superconducting film by evaporating a coating of the desired impurity less than an atomic layer thick onto the cooled substrate before evaporation of the Al film.

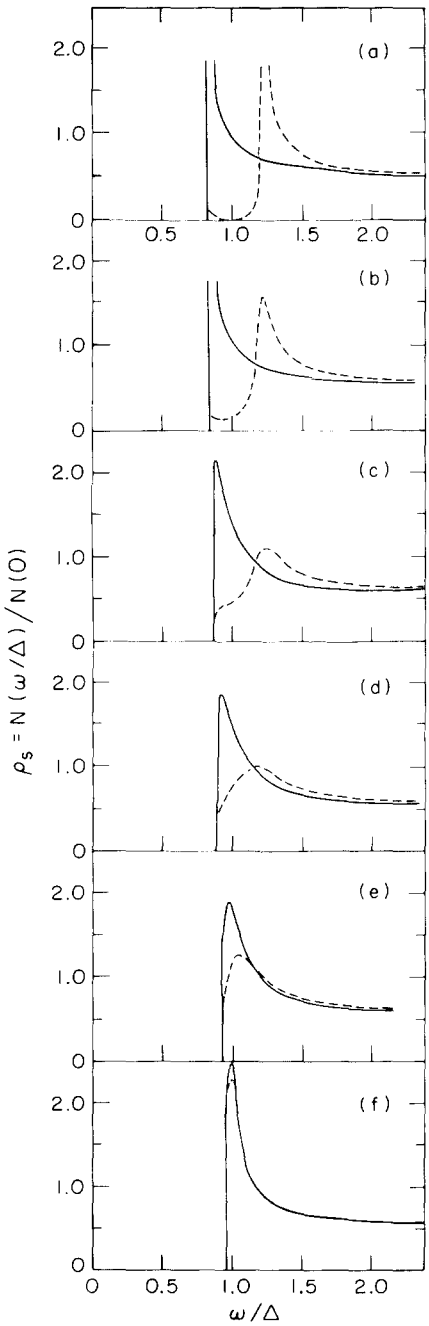

Fig. 15. Theoretical density of states for spin-down (solid line) and spin-up (dashed line) electrons in a magnetic field $H = 0.2\Delta/\mu$ with the spin–orbit parameter b as follows: (a) 0.02, (b) 0.1, (c) 0.3, (d) 0.6, (e) 1.5, and (f) 7.0 [62].

The results of such an experiment using Pt are shown in fig. 16 [66]. The sequence of dI/dV curves for increasing Pt thickness shows clearly the gradual disappearance of the spin splitting. Fitting these curves yields values of b which increase linearly with the number of Pt atoms added, as shown in fig. 17 [66].

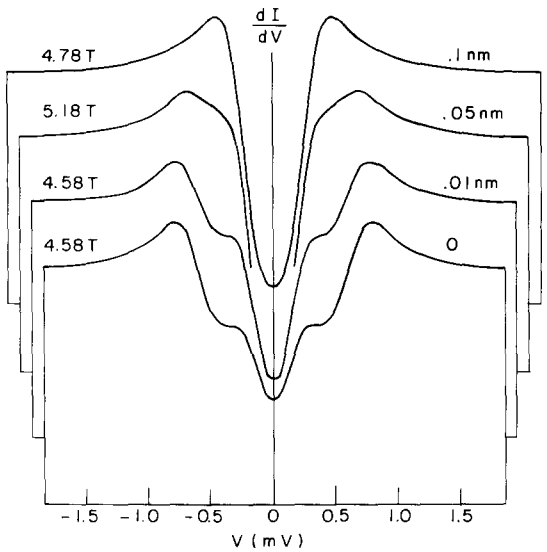

Fig. 16. Tunneling conductance curves dI/dV versus V for junctions made on Al films coated with Pt thicknesses of 0–0.1 nm. A magnetic field the magnitude of which is listed on the figure for each junction was applied parallel to the plane of the films [66].

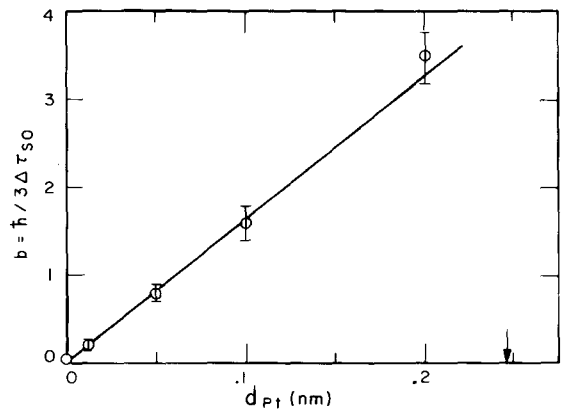

Fig. 17. Values of spin–orbit scattering parameter b versus average Pt thickness. The arrow marks the value of d_{pt} corresponding to one monolayer [66].

The theory also predicts an increase of H_{c2} if spin–orbit scattering lifts the Pauli limitation. Figure 18 shows that the critical field is more than doubled by about half of a monolayer of Pt [67]. For thicker layers the proximity effect of the Pt starts to dominate and T_c and H_c decrease. Using the parameters obtained by fitting fig. 18, H_{c2} can be calculated from the WHH theory and compared with the measured values in fig. 18. These calculated values of H_c are much lower than the measured values, implying a serious discrepancy of the theory of H_c. It had been pointed out by Orlando and Beasley [68] that, in order to fit $H_c(T)$ of Nb_3Sn with the WHH theory [69], it was necessary to use a spin–orbit scattering length shorter than the momentum scattering length, a choice that makes no physical sense. A way out of this dilemma was found by Rainer [70] through the introduction of a Fermi-liquid correction to the quasiparticle spin magnetic moment. This correction then produces quantitative agreement with experiment. The correction can also be measured using spin-polarized tunneling and will be described in section 4.

Measurements of b have been obtained by tunneling for the superconductors Be [71], Al [62, 72], V [73], V–Ti alloys [63, 74], V_3Ga [75], VN [76], Ga [77], Al(Pt) [66] and the high-T_c materials $Ba_{1-x}K_xBiO_3$ [78]. The values are listed in table 1. Only the values for Al, V and Ga have been corrected for Rainer's Fermi-liquid renormalization. The effect of doping on the values of b for Al has been observed for a number of elements including Cu, Ag, Pd, Pt and several rare-earths [79]. The results are qualitatively as expected from the atomic numbers of the elements, but no quantitative analysis of the data has been done except in the case of Pt [66]. For superconductors other than those listed above, such as NbN, In, Sn and Pb, no sign of splitting is seen in the tunneling curves in high H, making the derivation of a b value difficult. Values of b have been obtained for many superconductors by fitting $H_{c2}(T)$; however, as we have seen, these values are qualitative at best.

A second type of tunneling study of spin–orbit scattering uses S/I/S junctions and graphically demonstrates the qualitative effect of b on the density of states. The conductance of an S/I/S

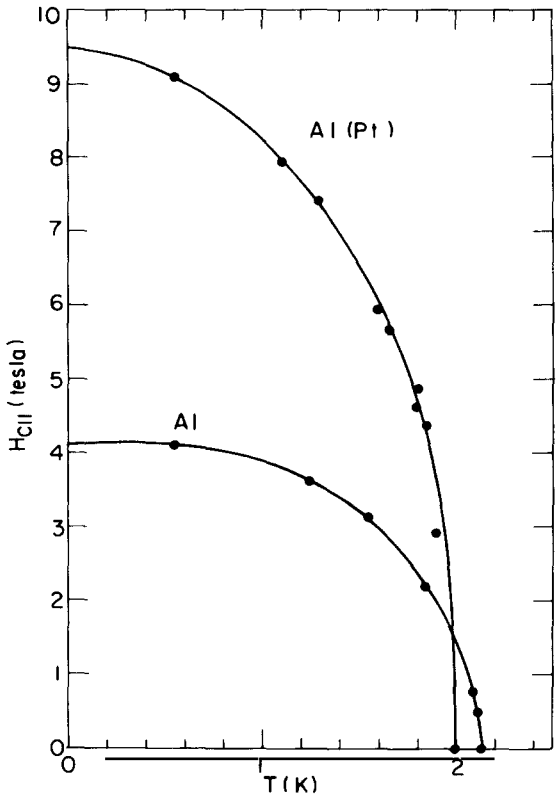

Fig. 18. The parallel critical field of identical Al films, one of which has been coated with 0.2 nm of Pt, demonstrating the effect of spin–orbit scattering on H_{c2}. After [67].

Table 1
Normal spin–orbit scattering rate b, spin scattering probability τ/τ_{so}, and Fermi-liquid parameter G^0 from tunneling measurements (reference numbers are in square brackets)

Superconductor	b[a]	$\tau/\tau_{so} \times 10^4$[b]	G^0
Al	0.05 [72]	5	0.3 ± 0.05 [144]
Be (amorphous)	~ 0 [71]	8	
Ga (amorpous)	0.16 [77]	7	0.81 ± 0.14 [146]
V	0.07 [73]	4	0.0 [73]
$Ba_{0.6}K_{0.4}BiO_3$	0.20 [78]	40	
V_3Ga	0.20 [75]	6	
VN	0.32 [76]	14	
V_xTi_{1-x}[c]	0.13 [74]	3	
A(Pt)[d]	0.05 + 15d [66]		
V_3Ga(Pt, Nb, Ti, Ta)	0.2 [80]		

[a] $b = \hbar/3\tau_{so}\Delta$.
[b] Calculated using the relation $\tau/\tau_{so} \approx l/\xi_0$ (τ = transport scattering time).
[c] $x =$ ≈ 0.6.
[d] d = Pt thickness in nm.

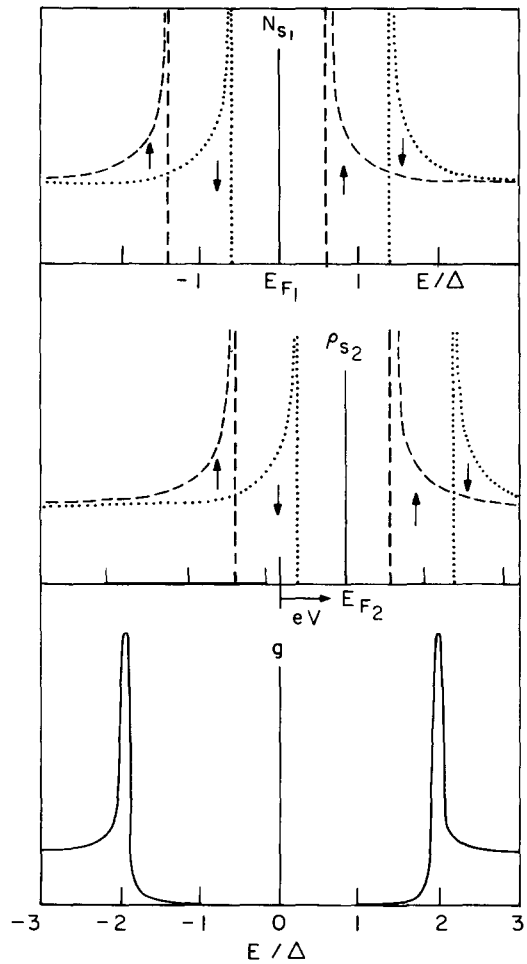

Fig. 19. Densities of states of two identical spin-paired superconducting films in a magnetic field are shown displaced by an amount corresponding to some applied voltage V. When V/e is increased to 2Δ, the quasiparticles can tunnel into states of the same spin and the large conductance peak shown at the bottom is expected in the absence of depairing by the magnetic field. After [62].

junction in zero field has a large sharp peak at the voltages $V = \pm(\Delta_1 + \Delta_2)/e$. These "sum of gaps" peaks are not affected by a magnetic field in the absence of spin–orbit scattering, except for gradual broadening due to orbital effects. This result can be understood from the diagram of fig. 19. The splitting of the density of states of the two superconductors does not affect the conductance because each splits by the same amount and spin is conserved in tunneling. Thus, the spin-up peak in the "filled" states of one superconductor at an energy of $-\Delta - \mu H$ and the spin-up peak in the "empty" states of the other at an energy of $\Delta - \mu H$ are separated by an energy of 2Δ, independent of H.

This situation changes when spin–orbit scattering is introduced. Now, for example, there will be some spin-up filled states at $-\Delta + \mu H$ (see fig. 15) [1, 50]. These states are now only $2\Delta - 2\mu H$ away from the empty spin-up states. Thus there will be a small peak in conductance at $V = \pm(2\Delta - 2\mu H)/e$, the height of which will be a measure of b. In fig. 20, a sequence of conductance curves at $V < 2\Delta$ of a junction between two nearly identical pure Al films for different field values is shown [62, 80]. The small peak representing the intrinsic strength of b in Al is shown

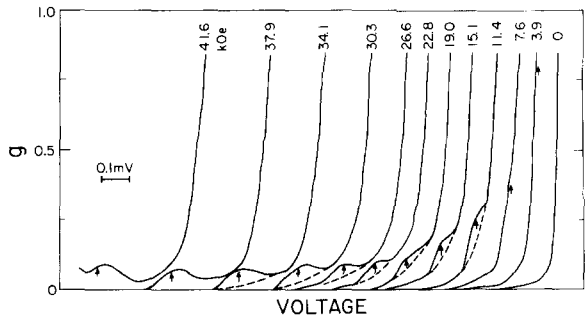

Fig. 20. Expanded plot of conductance g versus V of an Al–Al junction for various applied magnetic fields and for $V < (\Delta_1 + \Delta_2)/e$ showing the peak caused by the mixing of spin states. The arrows mark the position of $V = (\Delta_1 + \Delta_2 - 2\mu H)/e$ for each value of H. The curves have been displaced horizontally for clarity [62].

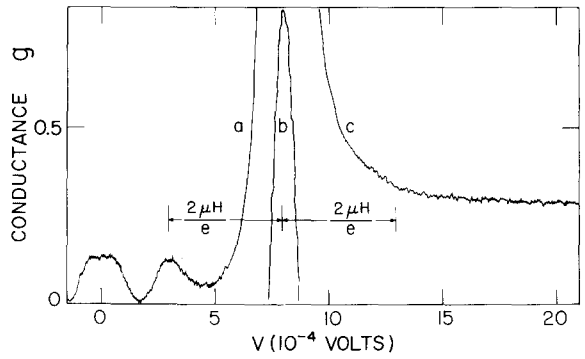

Fig. 21. Conductance g versus V for the same junction as in fig. 22. The peak at $V = (\Delta_1 + \Delta_2)/e$ (labeled b) has been displaced downward by 2.45 (in units of the normal-state conductance), while the portion labeled c has been displaced downward by 0.73 units. The absence of a peak at $V = (\Delta_1 + \Delta_2 - 2\mu H)/e$ shows that spin flipping does not take place during tunneling [62].

as it evolves with increasing H. Of course, as $b \to 1$, the separation of this peak from the sum-of-the-gaps peak will decrease. Note that in fig. 15 there is no peak predicted at $V = \pm(2\Delta + 2\mu H)/e$ because there are no states of opposite spin added to the density of states peaks at $\pm(\Delta + \mu H)$. In fact, the absence of a peak in tunneling conductance at $V = \pm(2\Delta + 2\mu H)/e$ verifies that spin is conserved in tunneling. If spins could flip while tunneling, a sort of anti-Stokes line would occur at these voltages. Figure 21 is an experimental verification that such a peak does not occur [62].

Figure 22 shows results of a similar experiment with Al doped with a few percent Mn to increase the spin–orbit scattering [62]. The increase in the size of the spin–orbit peak compared to that in fig. 20 is clearly seen. The Mn also lowers the T_{c0} of the Al, however, so the critical field is lower, reducing the range of the experiment. An interesting magnetic scattering effect was observed during the course of the Al (Mn) tunneling experiments. Figure 23 shows the conductance curves for an Al(Mn)–Al(Mn) junction with about 6% Mn [62]. At low fields, the conductance has characteristics of magnetic impurity scattering, with the sum-of-the-gaps peak broadening and no spin–orbit peak developing. However, at a field of about 1.5 T the conductance abruptly changes form to the shape of figs. 22 and 20: the sum-of-the-gaps peak sharpens and the spin–orbit scattering peak appears. Apparently, the Mn changes its role from that of a magnetic impurity at low fields to an ordinary non-magnetic scatterer at high fields.

Although the simple picture of spin–orbit scattering appears to work reasonably well for the case of impurities in Al, it cannot yield even qualitative predictions for more complicated systems. For example, the A15 superconductor V_3Ga is Pauli-limited even in bulk form [81]. The spin–orbit scattering parameter b is about 0.2, related presumably to the low atomic number of its constituents. The spin mean free path $l_{so} \approx \xi_0/b$ is about 10 nm, much greater than the atomic spacing. Thus, if a few percent of impurities with high Z are added to V_3Ga, the naive expectation might be that b would be increased. Such an experiment is attractive because, as Bending, et al. [75] first observed, the density of states of V_3Ga splits in an applied field, allowing the same tunneling techniques as applied to Al to be used. However, when the experiment was attempted, neither tunneling nor critical field measurements indicated any change in b [82]. Both, very thin films with surface layers of impurities and thick films with impurities co-deposited, were used. A wide range of

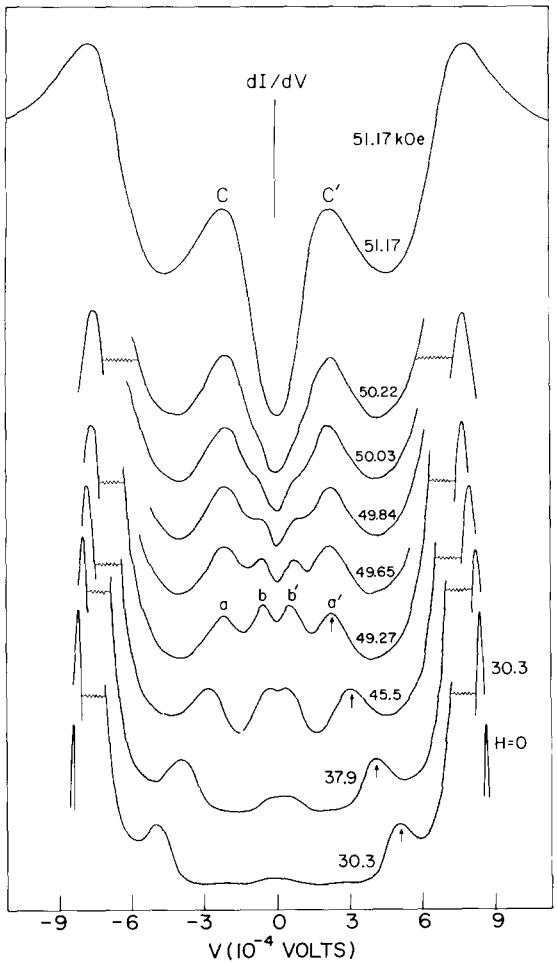

Fig. 22. Magnetic field dependence of the structure of dI/dV for an Al(Mn)–Al(Mn) junction as H approaches H_c. The peaks aa' are due to spin mixing, while bb' are the usual maxima which occur at $V = \pm(\Delta_1 - \Delta_2)/e$. The maxima at $V = \pm(\Delta_1 + \Delta_2)/e$ are shown displaced vertically for reference. With $H = 51.17$ kOe, film 2 is normal and the maxima cc' are the spin-split peaks described earlier for normal-metal–superconducting tunneling. The curves have been displaced vertically for clarity [62].

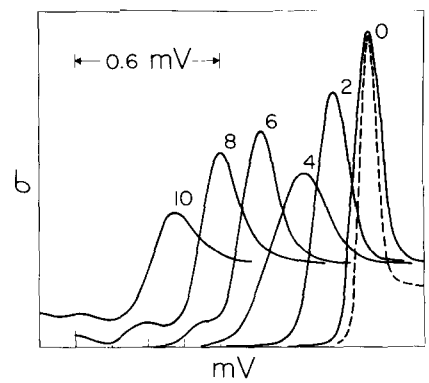

Fig. 23. Conductance of an Al(Mn)–Al(Mn) junction for several values of magnetic field. In low H (curves 0, 2, 4) the conductance peak at $V = (\Delta_1 + \Delta_2)/e$ is quite broad. In higher fields (curves 6, 8, 10) the peak becomes sharper and the spin–orbit interaction peak appears. The curves have been displaced horizontally. The value of H in teslas for each curve can be found by multiplying the number of the figure by 0.379 [62].

impurities was tried. The zero-field transition temperatures were affected, in agreement with published measurements on bulk samples, indicating that the impurities were being incorporated into the structure of V_3Ga. While it is possible that metallurgical problems could have influenced the results, it seems unlikely, because the zero-field properties corresponded to those observed in bulk investigations. A more complex view of the spin–orbit scattering process is probably needed.

Tkaczyk [79] summarizes attempts to put the theory of spin–orbit scattering on a firmer foundation. First, one assumes that a tight-binding model would better describe the process, since the interaction is strongest near the atom cores. Then the atomic matrix element of the

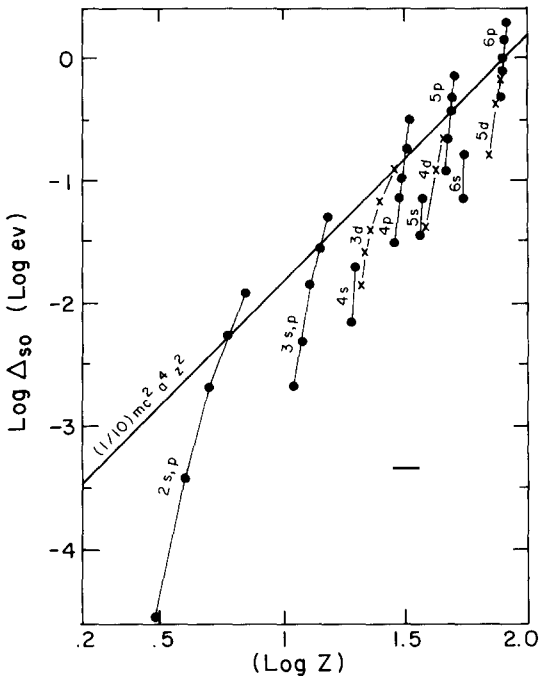

Fig. 24. The base-ten logarithm of the atomic valence p-orbital and metallic d-band splittings taken from Yafet [83] and Anderson [84], respectively. After Tkaczyk [79].

spin–orbit Hamiltonian

$$\Delta_{so} \equiv \int d\boldsymbol{r}\,\psi_n(\boldsymbol{r}) H_{so}(\boldsymbol{r}) \psi_n(\boldsymbol{r})$$

can be calculated, where $\psi_n(\boldsymbol{r})$ is an atomic orbital and the spin–orbit Hamiltonian

$$H_{so}(\boldsymbol{r}) = \frac{\hbar}{2m^2c^2}\, \boldsymbol{s} \times (\boldsymbol{\nabla} V(\boldsymbol{r})) \cdot \boldsymbol{\rho}\ ,$$

with $\boldsymbol{s}$ being the electron spin operator, $V(\boldsymbol{r})$ the electrostatic potential and $\boldsymbol{\rho}$ the momentum operator. The spin–orbit scattering rate

$$b \sim \frac{\hbar}{\tau_{so}} \sim C|\Delta_{so}|^2\ ,$$

where C is the impurity concentration. Values of Δ_{so} for atomic s, p electrons and metallic d-band splittings were assembled by Tkaczyk [79] from the work of Yafet [83] and of Mackintosh and Anderson [84], and are shown in fig. 24. These data indicate a general increase in Δ_{so} with Z^2 with a superimposed periodic variation depending on the valence of the atom. Thus b would have a general Z^4 dependence for a given impurity concentration as proposed by Abrikosov and Gor'kov [30].

Gallagher suggested that in samples with at least one dimension smaller compared to the mean free path, surface scattering will dominate and the effective impurity concentration is replaced by a quantity related to the ratio of the atomic spacing to the limiting sample dimension [65]. For example, a thin film made of grains whose diameter is roughly the film thickness d, an electron would encounter scattering events on that length scale, giving an effective "impurity" concentration of $(d/a)^2 \cdot 1/d^3 \sim 1/da^2$, where a is the atomic spacing. He found agreement with experiment for several simple metals within about a factor of 5.

Although the ideas of Gallagher may help quantify the spin–orbit interaction for s–p metals, they do not help in interpreting the V_3Ga results. However, taking the tight-binding approximation does point to a possible explanation. The superconducting paired electrons in A15 superconductors are of a strongly d character; consequently, their wave function is small at the scattering sites near the ion cores, resulting in severely reduced spin–orbit scattering.

2.5. *Spin–orbit scattering and weak localization*

Another useful technique for measuring spin–orbit scattering in very thin or disordered films involves measurement of the magnetoresistance at low temperatures in modest perpendicular fields (~ 1 T). The predictions of the theory of weak localization are then fitted to the data, yielding the spin–orbit rate as a fitting parameter. This technique has been used extensively by Bergmann and collaborators [85]. Alexander et al. [86] demonstrated that the rates measured by this technique and by spin–polarized tunneling are at least qualitatively the same.

Weak localization is a quantum phenomenon observed in disordered systems at low temperatures when the time between electron elastic scattering events becomes short compared to the time between inelastic events [85]. In this regime, the electron can traverse a closed path in a phase-coherent way by experiencing a series of elastic scattering events. An electron traveling the same path in a time-reversed way can interfere with the first one; the result is a loss of conductivity. This loss increases as the temperature is reduced because of the decrease in inelastic scattering rate. The application of a magnetic field destroys the phase coherence of the electron and its time-reversed partner restoring the lost conductivity. Thus a signature of weak localization in the absence of spin scattering is a negative magnetoresistance. This negative magnetoresistance was observed by Tedrow and Meservey in 1969 in thin Al films in a perpendicular field, but no theoretical explanation was then available [87].

The addition of spin scattering causes a qualitative change in the magnetoresistance. The perfect cancellation of time-reversed pairs no longer occurs in zero field. The application of a magnetic field then produces a positive magnetoresistance at low fields. The magnetoresistance can again become negative at higher fields, depending on the scattering rate. Fitting the theory to the data produces a magnetic field parameter characteristic of the scattering process. The derived rate of scattering is related to the characteristic field by the relationship

$$\tau_{so}^{-1} = 4H_{so}/\hbar e\rho N ,$$

where ρ is the resistivity, N is the density of states at E_F, and H_{so} is the characteristic magnetic field for spin–orbit scattering [88]. This relationship between scattering time and characteristic field led Bergmann to describe these experiments as time-of-flight measurements.

A series of measurements by Geier, Bergmann, and others [89] of the magnetoresistance of quench-condensed Mg films containing a submonolayer amount of a non-transition element metal demonstrates the utility of this technique. The authors deduced the spin–orbit scattering rate

caused by a number of s–p metals ranging from Cu to Bi in atomic number; they also calculated the spin–orbit cross section for sp impurities in Mg. The observed rates reflect the effect of the valence of the impurities as well as the effect of the atomic number in a way qualitatively similar to the theoretical expectation shown in fig. 24 [79]. The scattering cross section varies as $\sim Z^5$ for the noble metals.

3. Metallic ferromagnets

3.1. Measurements of 3d transition metals

After the discovery of spin splitting of the quasiparticle states in superconducting Al [61], it was apparent that using Al with a ferromagnetic counterelectrode should lead to interesting results. Nickel was chosen as the ferromagnet for the initial experiments, because it was believed that the majority spin (spin-up) d band was filled and was located below the Fermi energy, whereas the minority spin (spin-down) d band was partially filled and had a very large density of states at the Fermi energy as shown in fig. 25 [90]. In addition, the partially filled s band was expected to provide many of the tunneling electrons and because of s–d interactions it was believed that the conduction electrons should be polarized, but the amount and even the sign of the polarization were subject to controversy. It was expected that a polarization of the tunneling current would result in an asymmetry in the tunneling conductance to an Al film in a magnetic field and might reflect the relative density of spin states in the ferromagnet.

3.1.1. Early measurements and analysis

Measurements of tunnel conductance versus voltage were made at 0.4 K on $Al/Al_2O_3/Ni$ junctions in which the Al films were about 5 nm thick and the Ni was about 50 nm thick [91]. Because of the thinness of the Al films and their alignment with the magnetic field, fields up to 4 or 5 T could be applied as previously explained. In fields large enough to resolve the spin splitting of the density-of-states peaks, the domains of the Ni were completely aligned. Figure 26 shows

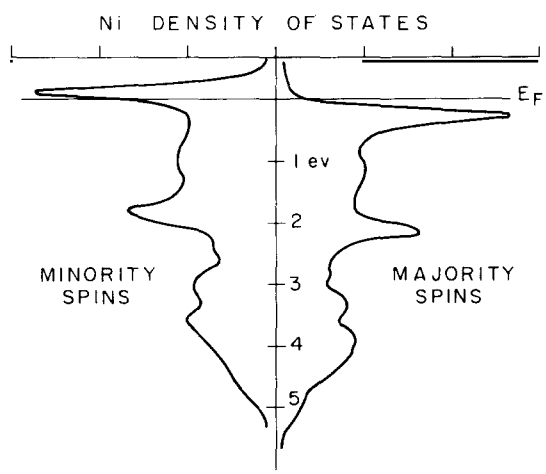

Fig. 25. Calculated Ni density of states adapted from ref. [90].

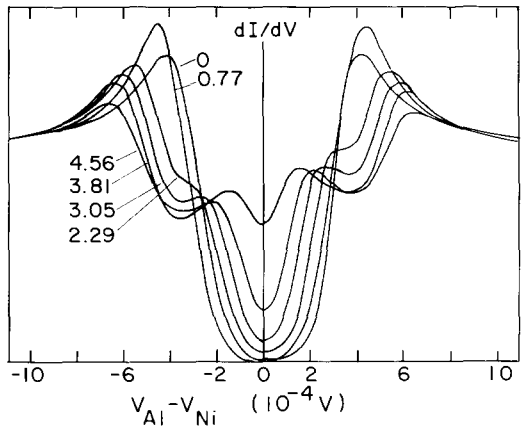

Fig. 26. Measured conductance versus voltage for an $Al/Al_2O_3/Ni$ junction in several values of magnetic field in teslas. Adapted from [92].

measurements of the tunneling conductance as a function of the voltage for various magnetic fields [92]. The spin splitting of the quasiparticle states becomes obvious at the higher fields and the asymmetry of the conductance about $V = 0$ is also apparent. This asymmetry implies that the tunneling electrons are partially spin polarized.

The results were initially analyzed by using essentially the same form as with a spin–split density of states as in eq. (16) but in which the conductance is the sum of contributions by spin-up and spin-down electrons:

$$\frac{\mathrm{d}I}{\mathrm{d}V} = \sigma(V) \sim \int_{-\infty}^{\infty} aN_s(E + \mu H) \frac{\beta \exp[\beta(E + eV)]}{\{1 + \exp[\beta(E + eV)]\}^2} \mathrm{d}E + \int_{-\infty}^{\infty} (1 - a)N_s(E - \mu H) \frac{\beta \exp[\beta(E + eV)]}{\{1 + \exp[\beta(E + eV)]\}^2} \mathrm{d}E \,. \tag{17}$$

Here $\beta = 1/kT$ and a is the fraction of the electrons whose magnetic moment is in the direction of the applied magnetic field. The spin polarization P is then defined as

$$P \equiv \frac{n\uparrow - n\downarrow}{n\uparrow + n\downarrow} = 2a - 1 \,. \tag{18}$$

Here $n\uparrow$ and $n\downarrow$ are the number of electrons whose magnetic moments are parallel and antiparallel to the field, respectively. This analysis is based on two assumptions: (1) The density of states of the superconductor for each spin direction in a given magnetic field has the same functional form and is merely displaced in energy by $\pm\mu H$. This assumption neglects effects of spin–orbit or spin-flip scattering in the superconductor, which is a good first approximation for pure Al films, as was previously shown. (2) There are no spin-flip tunneling processes, which was shown to be true for Al films with Al_2O_3 barriers [62]. With these assumptions, the results in fig. 26 can be understood qualitatively by referring to fig. 27. The dashed curve in fig. 27(a) shows the spin-up density of

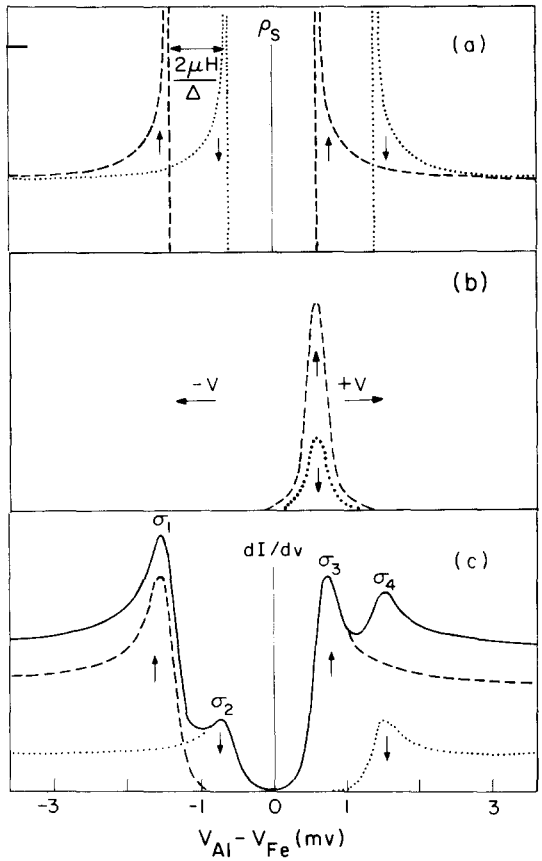

Fig. 27. Superconductor–ferromagnetic-metal tunneling. (a) BCS density of states of a superconductor as a function of voltage in a magnetic field. (b) Temperature-dependent kernels for each spin direction in the integral expressions for conductance. (c) Theoretical normalized conductance for each spin direction (dotted and dashed curves) and the total conductance (solid line). After [92].

states; the dotted curve shows the spin-down one, identical but displaced in energy by $2\mu H$. In fig. 27(b) derivatives of the two spin densities of states in the ferromagnet are shown near the Fermi energy with a larger amplitude for spin-up electrons than for spin-down. In the phenomenological theory the convolution of one spin function in fig. 27(a) with the corresponding spin function in fig. 27(b) gives the conductance at the voltage V shown in fig. 27(c). The sum of the two spin contributions gives the total conductance. In this figure the voltage is measured from the Fermi energy of the ferromagnetic film and the fact that the inner peak at positive voltage is larger than the peak at the corresponding negative voltage shows that electrons with their magnetic moments in the field direction (spin-up) predominate in the tunneling current.

It is important to note that in refs. [92, 93] and in some other publications the voltage was measured from the Fermi energy of Al film rather than that of the ferromagnetic one, as in figs. 26 and 27. However, all data and analysis in this review are presented in a manner conforming to the two conventions currently adopted. The first is that "spin-up" designates the electron spin direction in which the electron magnetic moment is in the direction of the applied magnetic field and has a lower energy than the "spin-down" electron whose magnetic moment is directed oppositely to the field. The second convention is that the voltage is to be measured with respect to the ferromagnetic electrode. With these conventions, a ferromagnetic metal whose tunneling

current is predominantly made up of majority electrons (that is, "spin-up") will give a result qualitatively like fig. 27.

More quantitatively, we can analyze the conductance curve to obtain the spin densities of states of the Al and the spin polarization of the tunneling current provided assumptions (1) and (2) made above are valid. Referring to fig. 27(c), if $g(V)$ is the unsplit conductance function, we assume that $ag(V-h)$ is the conductance contributed by spin-up electrons shifted in voltage by the Zeeman splitting $h = \mu H/e$. Here a is the fraction of spin-up electrons in the tunnel current and the spin-down fraction has a conductance $(1-a)g(V+h)$. The total measured conductance $G(V)$ is then the sum of the two spin contributions and is shown as the solid curve in fig. 27(c). We can write, for any value of V, four equations for the total (measured) conductance σ at the points $-V-h$, $-V+h$, $V-h$, and $V+h$ in terms of the unsplit function $g(x)$ [92]:

$$\sigma_1 = G(-V-h) = ag(-V) + (1-a)g(-V-2h)\,, \tag{19a}$$

$$\sigma_2 = G(-V+h) = ag(-V+2h) + (1-a)g(-V)\,, \tag{19b}$$

$$\sigma_3 = G(V-h) = ag(V) + (1-a)g(V-2h)\,, \tag{19c}$$

$$\sigma_4 = G(V+h) = ag(V+2h) + (1-a)g(V)\,, \tag{19d}$$

Assuming, as in the microscopic theory, that $g(V) = g(-V)$ for the unsplit function, we obtain from eqs. (19) the spin polarization P as a function of the measured conductances σ_1, σ_2, σ_3, and σ_4:

$$P = 2a - 1 = \frac{(\sigma_4 - \sigma_2) - (\sigma_1 - \sigma_3)}{(\sigma_4 - \sigma_2) + (\sigma_1 - \sigma_3)}\,. \tag{20}$$

Using this analysis, it was found that the curves in fig. 26 gave a value of $P = 11 \pm 1\%$ [92,93] signifying that the electrons in the tunneling current were predominantly spin-up, with their magnetic moments parallel to the magnetization in the Ni films. Later measurements [21,94,95] have given a larger value of P for Ni because of better junction preparation, as will be discussed later.

From eqs. (19a) and (19d) we can obtain the conductance of one spin direction at any value of V in terms of the quantity a and the measured total conductances $G(V)$ and $G(-V)$.

$$g(V-h) = [aG(-V) - (1-a)G(V)]/(2a-1)\,. \tag{21}$$

It should be realized that, since there is finite depairing in the Al film from the applied field, the function $g(V)$ will be different for different values of the magnetic field and temperature. If the assumptions on which the decomposition of the tunneling curves is based are valid, we can obtain the conductance in each spin direction, although, as described below, the resolution into separate spin states must be slightly generalized in the presence of spin–orbit scattering.

Equations (19) imply that any arbitrary value of voltage V and magnetic field could be selected to obtain P from eqs. (19) and (20). In practice, the values of V and H which are chosen are important

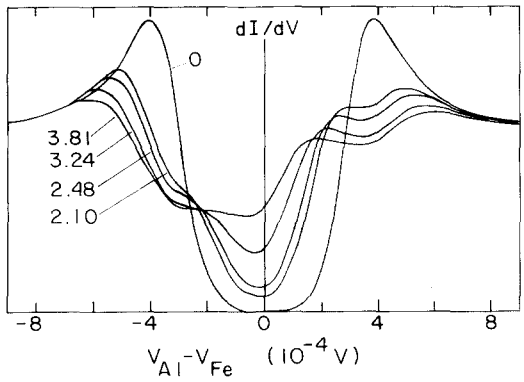

Fig. 28. Measured conductance versus voltage for a typical $Al/Al_2O_3/Fe$ junction at several values of magnetic field in teslas. After [92].

Table 2
Spin polarization of electrons tunneling from ferromagnetic metals

Metal	Spin polarization (%)
Fe	+ 40 ± 2
Co	+ 35 ± 3
Ni	+ 23 ± 3
Gd	+ 14 ± 3
Ho	+ 7.5 ± 1
Tb	+ 6.5 ± 1
Er	+ 5.5 ± 1
Dy	+ 7.0 ± 1
Tm	2.7 ± 1

in that they determine the accuracy of the result. For very low values of H the fringing field of the incompletely saturated ferromagnetic film depairs the Al film and the small amount of splitting decreases the accuracy. The effect of this depairing because of the fringing field of Ni can be seen in fig. 26, in which the density-of-states peaks at small but finite fields is sharper than that at $H = 0$, showing the decreased depairing with this increase in H. For values of H very close to the critical field of the Al film, the depairing of Al broadens the density-of-states curves and eventually obscures the effect of the magnetic field splitting. Selecting values of V so that σ_1, σ_2, σ_3, and σ_4 are close to the maxima of the conductance curves or at least in regions where the absolute value of the slope is small makes the results much less sensitive to random experimental errors. The values of V chosen standardly in calculating P are shown in fig. 27.

In addition to the results on Ni, measurements were made on Fe, Co, and Gd [92, 93]. For Fe the conductance is shown for various magnetic fields in fig. 28. The polarization for Fe is evidently much larger than for Ni. In these early measurements the values obtained for the spin polarization of Fe, Co, Ni, and Gd were, respectively, +44, +34, +11, and + 4.3% [92]. Although there was considerable scatter in the results, there was no evidence that the polarization varied with magnetic field. Perhaps the most important result is that for all of these metals the polarization was positive, that is, that the majority spin electrons in all cases were predominant in the tunnel current, a result which had not been predicted. Since these early measurements, the techniques of junction formation and measurement as well as the theoretical analysis of the results have been improved. With these changes some values of polarization have changed numerically [94], although the overall qualitative results remain unchanged. These later values for the 3d metals (corrected for spin–orbit scattering) are shown in table 2.

The early measurements relied on oxidizing the Al films in laboratory air saturated with water vapor to form the tunnel barrier and resulted in low values of P for Ni. Later, barriers were formed in situ with a glow discharge in pure oxygen, a technique which was introduced by Rogers [96], who obtained values of polarization for Ni from 17 to 25%. This improved technique increased our value of P for Ni from about 11% to about 23% (when corrected for spin–orbit scattering) and also increased the reproducibility. It was conjectured that in the older method, OH ions were present in the Al_2O_3 and led to a contamination of the Ni surface. The lower values of the early results on the rare-earth metals and their scatter are also probably the result of surface contamination.

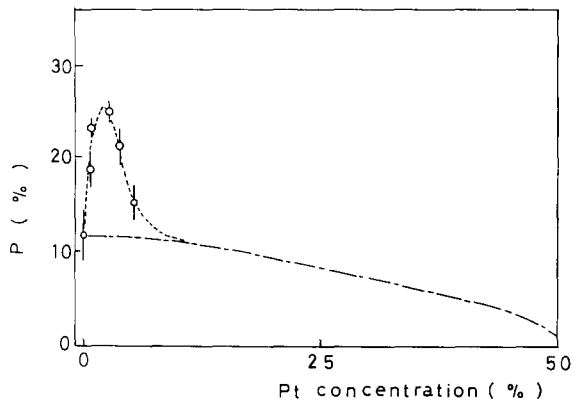

Fig. 29. Spin polarization P and the normalized magnetic moments of Ni–Pt and Ni–Pd alloys as a function of Pt concentration. After Akimitsu et al. [97].

An interesting result by Akimitsu et al. [97] was found in Ni/Pt and Ni/Pd alloys. Figure 29 shows P versus Pt concentration. The Al film was oxidized in a refrigerator at 10°C and pure Ni counterelectrodes gave rather scattered results averaging $P = 11\%$. For Ni alloys there was a sharp maximum in P of 25% at about 3% Pd or Pt. In addition, the values of P for the alloys was much less variable than for pure Ni. The results showed that in this case the value of P was not proportional to the saturation moment of these alloys in bulk, unlike other 3d ferromagnets. Akimitsu [97] suggested that the explanation of these results is that alloys containing Pt or Pd alter the Ni surface so that it is not contaminated as a result of impurities in Al_2O_3. Additional Pt is expected to reduce the magnetic moment and the value of P much more rapidly than additional Pd, a result found in the measurements. This discovery may be useful in the protection of ferromagnetic surfaces.

3.1.2. Effect of spin–orbit scattering

The simple analysis given above is no longer exactly correct when there is spin–orbit scattering in the superconducting film because the density of states (and the conductance) of the two spin states is not the same function of energy. The separate spin densities of states in a magnetic field have been derived by Engler and Fulde [1,48] from the microscopic theory including spin–orbit scattering. Figure 15 shows such densities of state as calculated by Bruno and Schwartz [50] for various values of spin–orbit scattering, assuming no orbital depairing. It is to be noted that with spin–orbit scattering the separate spin densities of states are not symmetrical about the Fermi energy, but that the spin-up density of states $N_s(E)\uparrow$ is equal to the spin-down density of states $N_s(-E)\downarrow$ and that for the corresponding conductances,

$$g(V)\uparrow = g(-V)\downarrow , \tag{22}$$

as shown schematically in fig. 30. For a ferromagnetic counterelectrode, if we know the value of a, we can use eq. (22) to calculate $g(V)\uparrow$ or $g(V)\downarrow$ algebraically from the measured total conductances $G(V)$ and $G(-V)$ at any two values of voltage symmetrical about

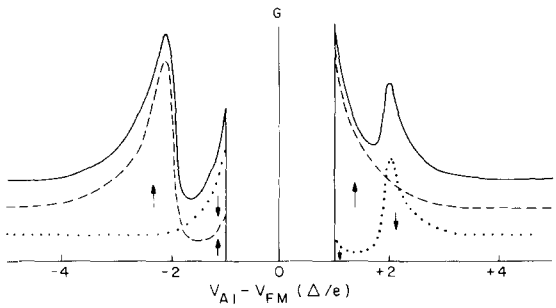

Fig. 30. Theoretical total density of states and individual spin densities of states in a magnetic field $H = 0.6\,\Delta/\mu$ for spin–orbit interaction parameter $b = 0.2$. Spin-up density of states shown by dashed curves, spin-down by dotted curves, and total density of states by solid curves.

$V = 0$ to be [92, 98]

$$g(V)\uparrow = \frac{a}{(2a-1)}[aG(+V) - (1-a)G(-V)]\,, \tag{23}$$

$$g(V)\downarrow = \frac{1-a}{(2a-1)}[aG(-V) - (1-a)G(+V)]\,. \tag{24}$$

It should be noted that this resolution of the spin conductances depends only on the assumed value of a and does not depend on the theory of superconductivity. This fact has proved to be particularly valuable near the critical field where the curves are greatly depaired, as will be discussed in section 4.

To obtain values of P from the conductance curves we have used the Maki–Fulde theory. In practice we assumed values for the polarization P and the spin–orbit scattering parameter b and calculated the conductance for the known temperature, magnetic field, and transition temperature of the superconductor using the theory. Using the best fits to the experimental data as a criterion, the values of P, b and the magnetic field depairing parameter were determined. By using different values of magnetic field these parameters could be determined with little ambiguity. Another method of determining the value of a or P from the spin-resolution method of eqs. (23) and (24) suggested by Rogers and Sullivan [99] is also based on the Engler–Fulde density-of-states theory. It is assumed that the correct value of P is one which resolves the density of spin states so that there is no observable peak in the spin-up density of states at a higher voltage than that corresponding to the main peak, a characteristic predicted by the theory. In practice, we have found that with sharply peaked tunneling conductances, small experimental errors can make this criterion somewhat ambiguous.

From numerical calculations it was found that for the aluminum film thickness used in these studies, the true value of P calculated from the full theory was always less than the value obtained from the simple analysis that neglected spin–orbit scattering that was given in the last section, which we will designate P^*. In fact for values of $b < 0.15$, the empirical equation $P = P^*(1 - 1.67b)$ agreed with the numerical calculation of P within the errors encountered in fitting the measured curves. Since this correction is independent of the magnitude of P in the range investigated, ratios of the values of P for different materials can be obtained from the ratios of the values of P^* without

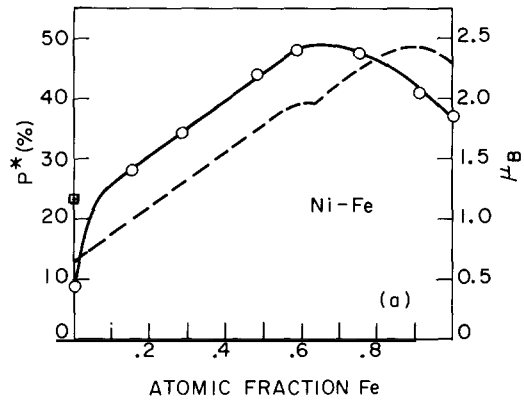

Fig. 31. Electron spin polarization P for various Ni–Fe alloys (circles and solid line). Dashed line gives accepted values of saturation magnetization per atom in Bohr magnetons at T = 0 (right-hand ordinate) for similar alloys. Square point is current value of P for pure Ni. Adapted from [100].

correction, provided the value of b remains constant. This result proved useful in the study of ferromagnetic alloys [100], but must not be used for values approaching 100% and will be discussed in section 5.2. For the Al films used in most of these studies of ferromagnets $b = 0.05$ and the value of P was about 8% less than P^*. In the most recent experiments we have used the theory of Rainer [101] which includes a Fermi-liquid correction. However, these corrections are of no importance for $T \ll T_c$ where the polarization measurements are made.

3.1.3. Results for 3d metals and alloys

The best current values for the measured electron spin polarization for tunnel currents from thin films of Fe, Co, and Ni are summarized in table 2. These measurements were all made on junctions whose barriers were formed by oxidizing Al with a pure oxygen glow discharge immediately before the ferromagnetic film was deposited. The values of P given have been corrected for the effects of spin–orbit scattering in the Al film. For Fe there is little change from the original measurements, for Co there is perhaps a slight increase in P, and for Ni, P is approximately twice that obtained in early measurements. With Ni the change is certainly attributable to the change in the technique in forming the junctions. The inclusion of H_2O in the Al_2O_3 and the subsequent contamination of the Ni surface is probably the cause of the decrease.

In the early results there was a rough proportionality between the value of P and the known saturation magnetic moment M of the ferromagnet. Even with the improved values of P there seems to be an almost linear relation between P and M. To study the relation between P and M, measurements of P were made for various 3d alloys. Results for Fe–Ni alloys are shown in fig. 31 [100]. Here the values of P and μ_B, the magnetic moment per atom of the bulk alloys, are plotted as a function of the atomic fraction of Fe. The dashed line corresponds to μ_B at $T = 0$ K and is taken from ref. [102]. The circles are the originally measured values of P; the revised value of P for pure Ni is included (shown as a square). Using this revised point for pure Ni, both P and μ_B are linear in the Fe concentration between 0% and 60% Fe. In this range Ni and Fe are known to form a continuous series of solid solutions and the magnetic anisotropy constant K_1 is close to zero for both crystalline and polycrystalline alloys. μ_B and P each has a maximum at less than 100% Fe, but the maxima do not coincide. Whether this is the result of structural differences between the films and the annealed bulk alloys is not known. The revised value of P for pure Ni makes the correlation

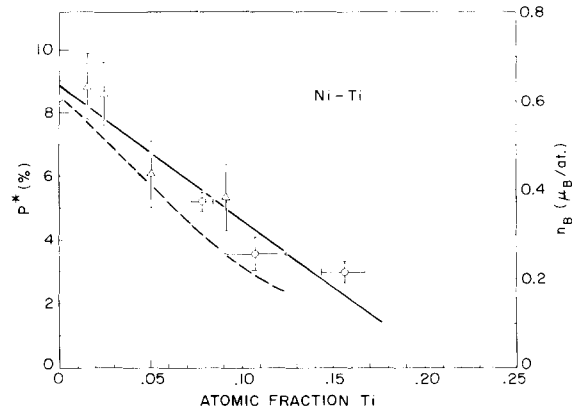

Fig. 32. P^* as a function of atomic fraction of Ti in Ni–Ti alloys is shown by the points and solid lines. The dashed line shows the saturation magnetic moment μ for these alloys as measured by others [100].

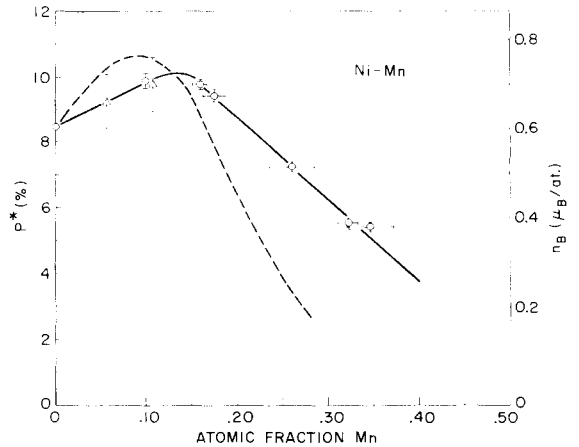

Fig. 33. P^* as a function of atomic fraction of Mn in Ni–Mn alloys is shown by the points and solid lines. The dashed line shows the known values of μ for these alloys [100].

better, and it is probable that the results for alloys with small amounts of Fe should be increased because of the sensitivity of the Ni surface to the old method of junction formation.

Alloys of Mo, Ti, Cu, Cr, or Mn in Ni were also measured [100]. The results for Ti and Mn are shown in figs. 32 and 33. The dashed curves in these figures are magnetization versus concentration results taken from the literature for bulk alloys. The maxima in fig. 33 in both P and M are strong evidence of the close relationship of these properties. In these figures the normalized polarization $P^* = (P^*_{\text{alloy}}/P^*_{\text{Ni}})\langle P^*_{\text{Ni}}\rangle$ and the bulk magnetic moment are plotted as a function of concentration. $\langle P^*_{\text{Ni}}\rangle$ is the value of P for Ni averaged over many depositions. This normalization is very useful for alloys with low concentrations of the element alloyed with Ni and for low polarizations. Absolute changes in polarization caused by variations in the film preparation method tend to be eliminated, as well as the effect of spin–orbit scattering and magnetic field depairing.

Sullivan and Rogers have measured the spin polarization in the Heusler alloy system Mn_xSb_{1-x} for Mn fractions of $x = 0$–100% [103]. Figure 34 shows the variation of P with Mn concentration. The maximum value of P (corrected by spin–orbit scattering) was about +25%. A correlation was found between the bulk magnetic moment per Mn ion and P.

3.2. *Interpretation of the 3d tunneling results*

When it became clear that the spin polarization P was positive in all tunneling measurements of 3d ferromagnetic metals, various theoretical explanations were proposed. In the context of field emission, it had been suggested [104] that in Ni the tunneling probability of the s electrons was 100–1000 times that of the d electrons and thus explained the lack of a very high negative spin polarization in Ni field emission. Hertz and Aoi [105] also argued that the s electrons are favored over d electrons in tunneling and that with the addition of s–d hybridization and spin-wave self-energy effects could, with "reasonable guesses" of band properties, give values of P of +8, +26, and +37% for Ni, Co, and Fe, respectively. Chazalviel and Yafet [106] assumed s–d hybridization and first, by completely neglecting the contribution of the d electrons, found values of P in different crystalline directions between +25 and +45% for Ni. They then suggested that

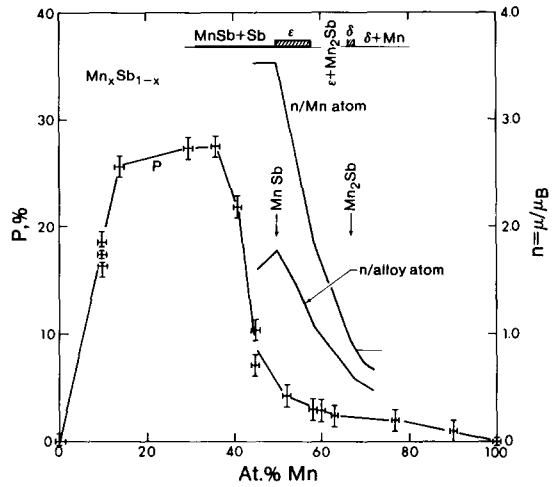

Fig. 34. Spin polarization results compared to bulk magnetization data of MnSb alloys. After [103].

a contribution from the large density of spin-down states could decrease P to a small and negative value and thus approximately agree with field emission results.

Stearns [107] extended these concepts into a very simple quantitative model in which the nearly free-electron-like s–d hybridized bands are assumed to provide essentially all of the tunnel current. The predictions of this model use known band data and lead to reasonably unambiguous results, unlike previous theories that had flexible parameters. This model uses the expression for the tunneling current I and conductance $\mathrm{d}I/\mathrm{d}V$ used by Giaever [16] to analyze his results for superconductors:

$$\frac{\mathrm{d}I}{\mathrm{d}V} = A \int_{-\infty}^{\infty} N_1(E) \cdot N_2(E) \cdot D[f(E) - f(E + eV)] \, \mathrm{d}E \,, \tag{25}$$

where D is the tunneling probability.

Harrison [108] had predicted that for independent particles in *one dimension*, the density-of-states (DOS) factor in the above expressions, which is proportional to $1/k$, would be exactly cancelled by a factor in the tunneling probability D, which is proportional to k. To explain the appearance of the DOS in the superconducting tunneling results, Bardeen [18] showed, by using the tunneling Hamiltonian method, that the tunneling probability factor comes from the overlap of the wave functions deep in the barrier region, where the superconducting many-particle interaction is not present. As a result, the tunneling probabilities D of the metals in the normal and superconducting state are identical and the tunneling current is proportional to the superconducting DOS.

In the ferromagnetic case Stearns [107] used Harrison's analysis but, citing Bardeen's many-body argument, assumed that the one-dimensional DOS for the two spin directions, $k_f^{-1}\uparrow$ and $k_f^{-1}\downarrow$, are identical and therefore drop out of the spin polarization, leaving

$$P = (k_f\uparrow - k_f\downarrow)/(k_f\uparrow + k_f\downarrow) \,. \tag{26}$$

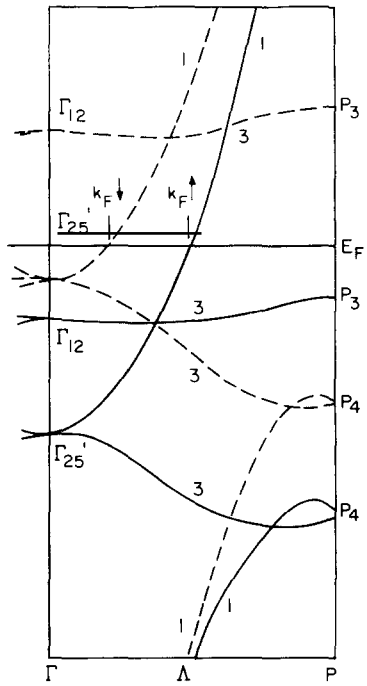

Fig. 35. Band structure of Fe in the (111) direction abstracted from calculations of Callaway and Wang [110].

This expression for P is the same as that obtained by assuming that P is determined by the polarization of the three-dimensional DOS of the ferromagnet, if we assume the tunneling electrons come from a parabolic band. It should be pointed out that according to Bardeen [18] it is the tunneling probability, proportional to k_f, which cancels out and the density of states factor which survives. When this argument is applied to the one-dimensional case, whose density of states is proportional to $1/k_f$, eq. (26) would not result. However, in the three-dimensional case, eq. (26) would seem to result from the Stearns argument.

The predictions of eq. (26) are especially clear in the [111] direction of Fe in which only the highly mobile s–d hybridized bands cross the Fermi energy and so are the only electrons contributing to the tunneling in this direction, as shown in fig. 35. Stearns designates these electrons as itinerant d electrons which lead to the RKKY interaction in the 3d metals [109]. Figure 35 is abstracted from a band structure calculation of Callaway and Wang and shows the bands in the [111] direction, where the situation is particularly clear [110]. By inserting the values of $k\uparrow$ and $k\downarrow$ from the figure into eq. (10), we obtain $P = +40\%$. To obtain an idea of the average value of the k vector for these bands over other directions, we can use the cross-sectional areas in k space around the [100], [110], and [111] directions as calculated by Callaway and Wang [110] for the ball-like parts of the Fermi surface (majority and minority spin are labelled I and VI in this reference). Table 3 shows the calculated values of P for Fe obtained by assuming that the average k vector is proportional to the square root of the area in k space for the nearly spherical areas. Also shown are results derived from areas obtained from de Haas–van Alphen measurements [111, 112].

These values of P compare very favorably with those obtained from tunneling and strongly support the view that the tunneling currents for the two spin directions are proportional to $k\uparrow$ and $k\downarrow$. Although this model fits the data for Fe and the original data for Ni, the recent measurements

Table 3
Spin polarization of electrons tunneling from Fe calculated according to the Stearns model [107] using band structure information from Callaway and Wang [110]

Crystal direction	$A\uparrow$ = area[a] of surface I[b]		$A\downarrow$ = area of surface VI[c]		$P = (\sqrt{A}\uparrow - \sqrt{A}\downarrow)/(\sqrt{A}\uparrow + \sqrt{A}\downarrow)$	
	Theory[d]	Experiment[e]	Theory[d]	Experiment[e]	Theory[d]	Experiment[e]
100	412	436	76	64	0.40	0.42
110	310	349	64	58	0.375	0.42
111	373	370	59	52.2	0.43	0.45
		369		51.8		
Average of 3 directions					0.40	0.43

[a] Area expressed in frequency units (mG) appropriate to de Haas–van Alphen measurements.
[b] Fermi surface cross-sectional area of large Γ-centered majority-spin electron surface (surface I of ref. [110]).
[c] Fermi surface cross-sectional area of central minority-spin electron surface (surface VI of ref. [110]).
[d] Callaway and Wang [110].
[e] de Haas–van Alphen measurements, refs. [111, 112].

of Ni in which $P = 23\%$ (corrected for spin–orbit scattering) is almost twice that expected from the model based on band structure calculations. The value of P for Co is roughly what is expected from this simple model based on the band structure, which unfortunately is not known as well as that of Ni and Fe.

According to Stearns [107], the approximate proportionality of the polarization to the saturation moments in 3d metals and alloys is also to be expected. Since the exchange splitting of the s–d electrons is about the same as that of the localized d electrons (which probably provide 95% of the magnetic moment), it follows that the polarization of the s–d electrons is approximately proportional to the saturation magnetic moment of the 3d ferromagnetic metal. As a first-order approximation, eq. (26) provides strong evidence in its favor, but more detailed coincidence of predictions from band structure and polarization measurements are needed to test it further.

3.3. *Rare-earth metals*

Measurements of P were made in the heavy rare-earth metals Eu, Gd, Tb, Dy, Ho, Er, Tm, Yb, and Lu [113]. The technique used was the same as with the 3d metals described above. For Yb and Lu, which are not ferromagnetic, $P = 0$; for the other elements, values of P were all found to be positive, as in the case of the 3d ferromagnets. For the ferromagnetic 4f metals, the magnetic moment is mainly provided by the 4f electrons, which are much too localized to contribute to the tunnel current. An indirect interaction between the 4f and 6s and 5d conduction electrons causes the conduction electrons to be positively polarized. Figure 36 shows that the values of P for the various elements are positive and are roughly proportional to the known values of the saturation moment of the *conduction* electrons of these elements. It should be noted that the original value of P for Gd [92] was rather uncertain and much lower than later values, presumably because of the later improvement in preparation techniques. One result of these measurements on the rare-earth metals was that it was definitely shown that positively polarized electrons in the ferromagnet gave a positively polarized tunnel current, a result which eliminated certain conjectures about spin flips in the tunneling process that had been advanced to explain the results in the 3d metals. Further experiments using rare-earth metals and their compounds are discussed in section 5.

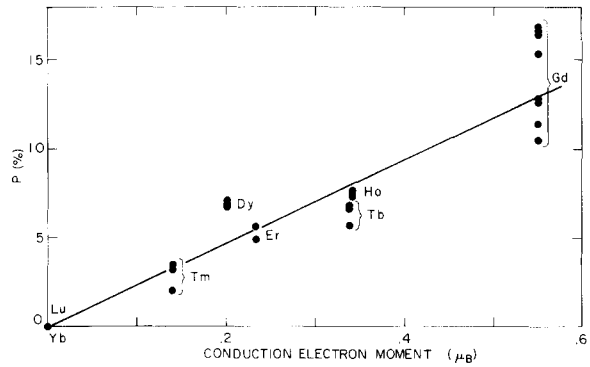

Fig. 36. Measured polarization P as a function of the magnetic moment of the *conduction electrons* for the heavy rare-earth elements. Each value of P represents a different evaporation. The solid line is the least-squares fit to the average of the points of each ferromagnetic element and is constrained to pass through zero. For Tb the older value of μ_{CE} is used in fitting; the newer value is shown displaced to a higher value. Slight lateral displacement of points is for clarity [113].

3.4. Ultra-thin films of ferromagnets

Spin polarization measurements of ultra-thin films was undertaken in response to claims that the surface of a ferromagnet might not be ferromagnetic, that is, might have a surface "dead layer" [114, 115]. On the other hand, Shinjo et al. [116] found a small amount of ^{57}Co to be ferromagnetic on bulk Co. Spin-polarized photoemission of very thin layers of Ni on Cu gave no evidence of dead layers [117]. Actually, the fact that spin polarization was observed in tunneling seemed to preclude such dead layers, at least when in contact with Al_2O_3, since the tunneling process depends on the wave function of the first atomic layer. However, the characteristics of ultra-thin layers of ferromagnets were not known and could evidently be studied by tunneling.

In the first experiments tunnel junctions were formed by depositing a thin layer of Co over oxidized Al films held at about 80 K and immediately covering the Co with Al [118]. The average thickness of the Co varied from 0.1 to 2 nm (a monolayer being about 0.22 nm) and down to 2 monolayers the value of P decreased according to the area covered by the Co film as calculated by assuming a Poisson distribution of the Co atoms as they were deposited. By one monolayer, P was close to zero, a result which probably means the breaking of continuity in the monolayer film and with it the suppression of the exchange interaction. The results gave no indication of a decrease of the ferromagnetism with thickness. Further measurements of ultra-thin layers of Ni and Fe were stimulated by anomalous Hall effect studies by Bergmann [119], who found that Ni less than three monolayers thick on a Pb substrate was not ferromagnetic. Tunneling measurements [120, 121] gave similar results for Ni on Al as shown in fig. 37 [121]. Below 3 monolayers $P \approx 0$, whereas above 3 monolayers, P increases rapidly, but only approached the bulk value at a thickness of 3 nm. In great contrast to these results with Ni on Al were those with Ni on Au; $P = 3\%$ was measured at 1 monolayer and $P = 70\%$ of its bulk value was found at two monolayers [121]. Ni backed by Mn or Cr also depressed P to almost zero at up to 2 monolayers. This behavior contrasted sharply with that of Fe (see fig. 38) [120], in which the value of P at 1 monolayer was about 30% and by 2 monolayers had reached 85% of its bulk value. With Co [118], and with Gd and Tm [122], the behavior was similar to that of Fe and there was no clear indication of non-ferromagnetic behavior down to one monolayer when in contact with Al. These results also agreed with those of Bergmann [119, 123].

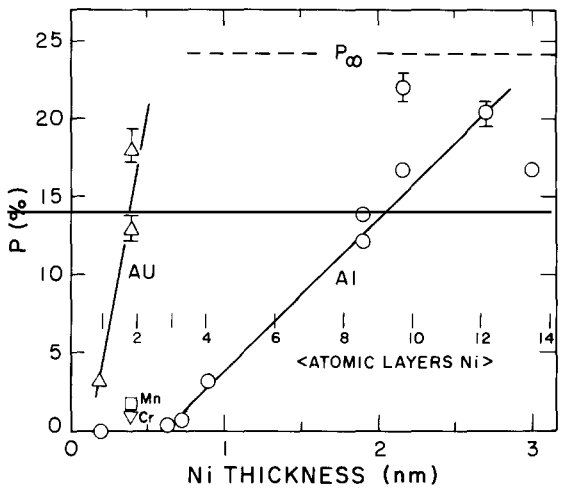

Fig. 37. Measured electron spin polarization P for Ni of various thicknesses in contact with Al, Au, Mn, and Cr [121].

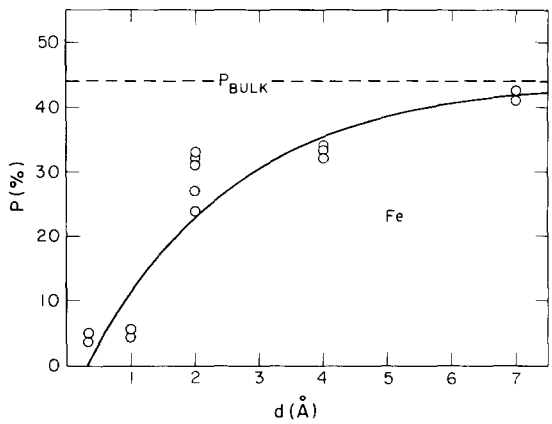

Fig. 38. Measured polarization of electrons tunneling from a layer of Fe of average thickness d on Al [94].

The tunneling [120–122] and anomalous Hall effect measurements [119, 123] both are consistent with the following interpretation. Polyvalent metals such as Al, Pb, Sn, and In suppress the magnetic interaction in Ni so that the first 2 to 3 layers of Ni are non-magnetic. On the other hand, monovalent metals such as Au, Ag, and Cu have much less or no effect in suppressing the magnetic interaction of Ni. A previous photoemission measurement of Ni on Cu by Pierce and Siegmann [117] had found no suppression of the Ni moment. Fe is affected little, if any, by the backing metal; for Co the value of P appears to be slightly suppressed by Al.

The results for the minimum onset thickness for P in Ni backed by Al, Au, Mn, and Cr fit very well with the theoretical picture as proposed by Tersoff and Falicov [124] and by Cox et al. [125] based on the hybridization of s–p electrons of the backing metal with d electrons in the ferromagnet. It was suggested by Tersoff and Falicov [124] that the operative mechanism which suppresses the ferromagnetism in Ni films on non-magnetic metal substrates is substantially the same as that which suppresses impurity magnetism in a non-magnetic host and that which determines the magnetism in alloys of Ni. The suppression of the magnetic moment in Ni alloys increases only slowly with Au, Ag, and Cu; the suppression is much more rapid with polyvalent metals. One experimental result that is inconsistent with the above theoretical picture is the slowness with which P derived from the tunneling converges toward its bulk value with increasing Ni thickness when it is backed with Al [120, 121]. The suppression of P and presumably the magnetic moment to more than 10 atomic layers cannot be explained by the usual range of an exchange interaction. Diffusion of the normal metal into the Al might create such an effect, but the experimental evidence is against this explanation.

3.5. Single-crystal experiments and artificial tunnel barriers

Although the band structure explanation of the measured values of P has considerable experimental support, particularly for Fe, a more detailed agreement between theory and experiment is needed before this model can definitely be confirmed. Tunnel measurements on single crystals as a function of crystal direction as compared with the known band structure should confirm or

disprove this model. Some initial experiments were tried with Ni single crystals. When NiO was used as a barrier with an Al counterelectrode, the Al film was evidently depaired, little or no spin splitting was observed, and no interpretable results were obtained. Consequently deposition of Al_2O_3 onto the Ni crystal was attempted as a tunnel barrier. The difficulty of forming such an artificial barrier on the surface of an existing crystal is very much greater than using the barrier which forms naturally on the Al surface when it is exposed to oxygen. In fact we produced only one tunnel junction which did not have anomalous features on the conductance curves which made their interpretation ambiguous. This one junction on the Ni (110) face, which had been ion-milled before coating with the Al_2O_3 tunnel barrier, gave a value of $P = +13\%$ [126]. The conclusion of this program was that improved equipment was needed in which the surface could be cleaned and annealed before the junction was formed with the whole process carried out in ultra-high vacuum.

3.6. Tunneling between ferromagnets

3.6.1. Experimental results

A logical extension of the tunneling between ferromagnetic metals and superconductors is the tunneling between two ferromagnetic metals. A simple model proposed by Julliere [127] assumes that the spin is conserved in the tunneling process and that the conductance of each spin direction is proportional to the densities of states of that spin in each electrode. In this model one expects that the tunnel current will be larger when the magnetizations of the two metals are parallel than when they are antiparallel. Analyzing the results in much the same way as with tunneling between a ferromagnet and a superconductor, the conductances in the parallel and antiparallel arrangements G_P and G_{AP} are then

$$G_P = a_1 a_2 + (1 - a_1)(1 - a_2) , \tag{27}$$

$$G_{AP} = a_1(1 - a_2) + (1 - a_1)a_2 , \tag{28}$$

where a_1 and a_2 are the fractions of majority spin electrons in the DOS of the two ferromagnets. The fractional difference in conductivity was defined by Maekawa and Gäfvert [128] to be

$$\Delta G/G = 2P_1 P_2 , \tag{29}$$

where the polarizations of the two metals are $P_1 = 2a_1 - 1$ and $P_2 = 2a_2 - 1$.

Julliere [127] formed Fe/Ge/Co junctions and measured the conductance at $T = 4.2$ K in different magnetic fields as function of applied voltage. At $V = 0$, $\Delta G/G$ was about 14%. This change in conductance decreased rapidly with increased voltage and at 6 mV was about 2%. Apparently, $\Delta G/G$ was an effect of a zero-bias anomaly [2], which is believed to be caused by magnetic moments in the barrier, but whose precise nature is still not entirely understood. In later studies by Kabani et al. [129] using Fe/amorphous Ge/Co junctions, $\Delta G/G < 0.1\%$. There is considerable evidence that amorphous Si and amorphous Ge barriers lead to spin scattering in the tunneling process [130].

Maekawa and Gäfvert [128] measured the conductance of Ni/NiO/ferromagnet junctions with Ni, Fe, or Co as the ferromagnetic electrode. For Ni/NiO/Co at 4.2 K a value of $\Delta G/G$ equal to about 2% was observed, which correlated well with the parallel and antiparallel orientations as shown by the hysteresis in the magnetic induction of the Ni and Co films, which have different coercive fields (fig. 39). Since the resistance of the junction was about 1000 Ω as compared to about

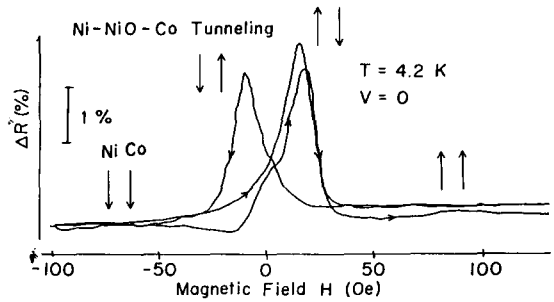

Fig. 39. Magnetoresistance of Ni/NiO/Co junction versus magnetic field. After Maekawa and Gäfvert [128].

1 Ω for the resistance of the films, the effect of the magnetoresistance in the films was neglected. $\Delta G/G$ decreased rapidly with temperature, but was still observable at 77 K for Ni/NiO/Co junctions. The observed effects with Ni and Fe counterelectrodes were smaller and more complex. Further measurements of Ni/NiO/Co junctions were made by Suezawa and Gondo [131] in which the films were deposited to give very square hysteresis curves. Magnetic field dependence of the resistance was observed at 77 and 300 K, but because of the low resistance of the junctions, the effect of the magnetoresistance of the leads may have been important.

For higher resistance junctions, Kabani et al. [132] have obtained results on Ni/NiO/Co junctions similar to those of Maekawa and Gäfvert [128]. The largest value of $\Delta G/G = 2\%$ observed was at 4.2 K and 0.11% was found at 77 K. For these junctions whose resistance was about 900 Ω, the effect of magnetoresistance in the leads was not more than one tenth of junction effects. For low-resistance junctions the magnetoresistance effects in the leads can dominate and give curves quite similar to those of the junctions. One result which may be pertinent to such junctions is that in Ni/NiO/Al junctions no spin polarization was observed and in fact the superconducting gap structure of the Al film was seen only as a rather shallow depression near zero voltage, and the junctions were often unstable [133]. It was conjectured that there was inelastic spin scattering in tunneling through the NiO barrier. In this regard, it is interesting that magnon effects in NiO have been seen by tunneling. [134].

Nowak and Rauluszkiewicz [135] have measured the hysteresis of the tunneling resistance of $Gd/GdO_x/Fe$ and $Fe/GdO_x/Fe$ junctions in a magnetic field. The domain structures and magnetization reversal process were investigated using defocused electron microscopy. These authors concluded that the hysteresis of the resistance with field was attributable to a spin-filter effect in the GdO_x barrier rather than to the parallel and antiparallel alignment of the electrodes. The spin-filter effect will be discussed in section 5.

An experiment using the technique of the scanning tunneling microscope has been reported by Johnson and Clark [136]. A magnetically aligned Ni crystal is brought close to a permalloy torus whose magnetization vector can be made parallel or antiparallel to that of Ni by a coil on the torus. The experiment is carried out in air, so that presumably there is a coating of oxide on each electrode. It was thought that the coatings of NiO and iron oxides were in contact during the measurement. The authors report values of $\Delta G/G$ ranging from 24 to 70% at room temperature. The sensitive modulation technique shows promise, but further experiments in high vacuum with clean surfaces are needed to clarify the results.

A recent experiment by Wiesendanger et al. [137, 138] used a scanning tunneling microscope with a CrO_2 tip to investigate the spin polarization of the tunneling electrons into the terraced surface of Cr(001). The terraces were separated by monatomic steps and were of alternating

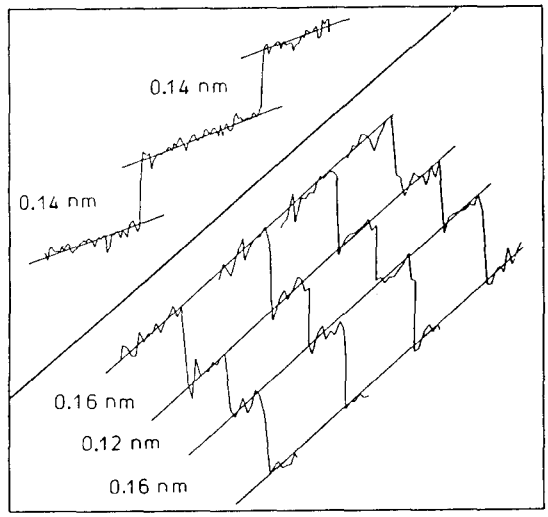

Fig. 40. Cr single-line scans over the same three monatomic steps of Cr (001) with a CrO_2 tip (lower right) showing alternation of magnitude of tunnel current for spin-up and spin-down terraces. Upper left shows two steps scanned with a W tip showing equal current for each terrace. After [137].

magnetic moment. The tunneling distances for alternate layers were different when scanned in the constant-current mode, implying that the tunneling current was larger for one spin direction than for the other (fig. 40). Using the measured values of the tunnel barrier and the height of the monatomic steps, a value of the polarization of the tunneling electrons was calculated to be $P = 20 \pm 10\%$. Assuming that the electrons emitted by the CrO_2 are nearly 100% polarized as measured by photoemission by Kämper et al. [139], this measurement can be interpreted in the Stearns model [107] as measuring the relative densities of spin states of the itinerant electrons in Cr at E_F.

More recently, Wiesendanger et al. [140, 141] have shown that the spin configuration of an Fe^{2+} or Fe^{3+} ion in Fe_3O_4 could be detected using an Fe tunneling tip. This is the first time that spin-polarized tunneling has been successful on an atomic level. The methods of preparation of tunneling tips of Fe and Cr are described by Wiesendanger et al. [140] and provide a comparatively simple way of attaining spin-sensitive tunneling with atomic resolution. An important feature of this development is that the spin polarization can be measured as a function of energy from the Fermi energy by changing the voltage bias. This may allow detailed spectroscopy of magnetic materials on an atomic level.

3.6.2. Interpretation and theory

The simple model of Julliere [127] was based on the Stearns [107] argument that the ferromagnetic many-body interactions would be turned off at the ferromagnetic–barrier interface and that the wave functions in the barrier region would be the same for spin-up and spin-down electrons. This model, which assumed that the tunnel current is proportional to the density of states of each spin of the highly itinerant electrons in the ferromagnet, seemed to explain the superconducting–ferromagnetic results. However, many of the ferromagnetic–ferromagnetic tunneling results to date have not correlated well with this simple model. Slonczewski [142] has suggested a different model to explain the F/I/F results. Electrons are treated as independent particles with spin-up and spin-down electrons having different wave vectors $k\uparrow$ and $k\downarrow$ inside the ferromagnet, but the same attenuation coefficient k in the barrier region. The wave function matching at the

ferromagnet–insulator boundaries is done separately for each spin direction and the total current is the sum of these two independent currents. The resulting relative change in conductance for parallel and antiparallel moments is the same as eq. (29) with two additional factors:

$$\frac{\Delta G}{G_0} = 2\left(\frac{k_1\uparrow - k_1\downarrow}{k_1\uparrow + k_1\downarrow}\right)\left(\frac{k^2 - k_1\uparrow k_1\downarrow}{k^2 + k_1\uparrow k_1\downarrow}\right)\left(\frac{k^2 - k_2\uparrow k_2\downarrow}{k^2 + k_2\uparrow k_2\downarrow}\right)\left(\frac{k_2\uparrow - k_2\downarrow}{k_2\uparrow + k_2\downarrow}\right). \tag{30}$$

Depending on the relative magnitudes of k, $k\uparrow$ and $k\downarrow$, the predicted value of $\Delta G/G$ can vary greatly and can be of opposite sign. Data which appear to fit this pattern are presented in ref. [143].

At present the data are too conflicting to decide if either of these models corresponds to the physical situation. Conductance anomalies (which are usually considered to be the result of spin scattering of electrons from localized magnetic moments in the barrier region) have been present in many of the experiments and may be essential to some of the results. In the Julliere [127] experiments, the effect seems to be present only in the conductance anomaly region and apparently neither model should apply. The Slonczewski assumption [142] that wave functions which result from a many-body exchange interaction can be matched at the boundary of a ferromagnet as if they were independent particles with identified spin needs more quantitative backing by F/I/F experiments as well as explanation of the S/I/F results. The polarization obtained by Johnson and Clarke [136] is larger than predicted by either of these theoretical models. The new techniques introduced by Wiesendanger et al. with ultra-high vacuum tunneling and characterized surfaces should help to resolve these uncertainties.

4. Fermi-liquid effects

Since its introduction into the theory of H_{c2} by Ferrell [28] and Anderson [29], the spin–orbit scattering rate b had been used as a fitting parameter to obtain agreement between measured values of $H_{c2}(T)$ and the WHH theory [32]. The apparent success of the theory was thus only qualitative. Unphysically high rates were required to obtain agreement in many cases, as was pointed out by Orlando and Beasley [68]. Further, values of b obtained from spin-polarized tunneling with Al films were a factor of 5 smaller than those obtained from fitting the WHH theory to $H_{c2}^{\parallel}$ of the same films [67]. Consequently, the critical fields calculated using parameters obtained from tunneling were about 40% lower than the measured ones. Orlando and Beasley also pointed out that inclusion of many-body effects, in particular enhanced spin paramagnetism, could reduce the amount of spin–orbit scattering needed to fit the critical fields of some transition metal superconductors. The theoretical answer to this problem was supplied by Rainer [70], who pointed out that Fermi-liquid corrections to the quasiparticle spin magnetic moment had to be included, if the theory was to be quantitative. In addition, he showed that the tunneling density of states is changed qualitatively by the inclusion of Fermi-liquid effects, allowing quantitative measurements to be made of the underlying Fermi-liquid parameter, G^0. Here G^0 is the $l = 0$ antisymmetric Fermi-liquid parameter and is equal to $N(\gamma)/N(\chi) - 1$, where $N(\gamma)$ is the density of states obtained from the normal-state electronic specific heat and $N(\chi)$ is that obtained from the spin susceptibility. The application of Rainer's ideas to thin-film superconductors was demonstrated experimentally by Tedrow et al. [144] and Alexander et al. [101, 145] Rainer's theory is described in ref. [101].

The singlet pairing of electrons in a BCS superconductor makes such a material useful for studying normal-state Fermi-liquid effects which involve the electron spins. At low temperatures, $T \ll T_c$, the spins are all paired and the Fermi-liquid effects are turned off. As $T \to T_c$, however, quasiparticles are excited and their density approaches the normal-state carrier concentration.

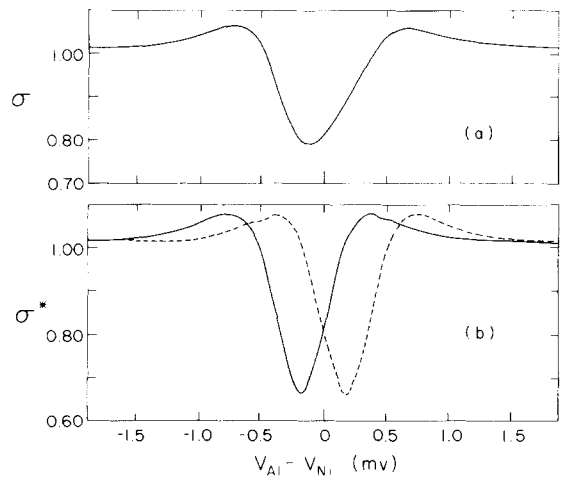

Fig. 41. In (a) and (b) the measured conductance and the resolved spin conductances are shown for a temperature of 1.53 K (reduced temperature = 0.61) [98].

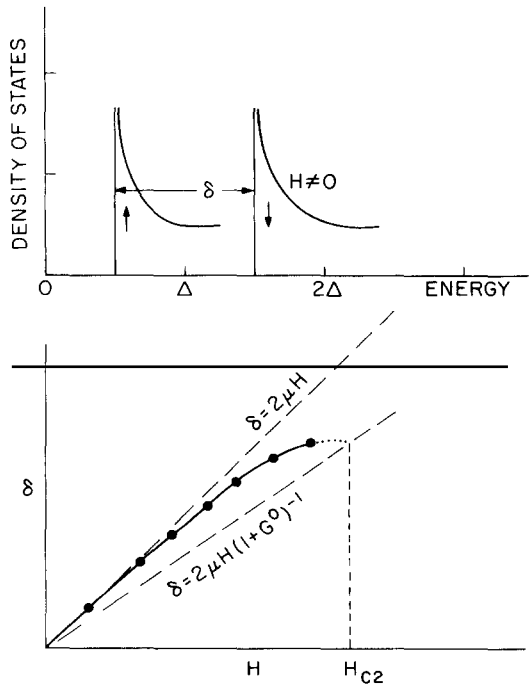

Fig. 42. The splitting δ defined in (a) deviates from $2\mu H$ if $G^0 \neq 0$, as shown in (b).

Thus, right at the (second-order) superconductor-to-normal state phase boundary, the Fermi-liquid effects are fully turned on and become equal in strength to those in the normal state. The energy splitting of the quasiparticle density of states of a thin superconducting film in a parallel magnetic field is a measurable quantity which exhibits this "turn-on" effect, and, further, it is easily measured by spin-polarized tunneling. If the splitting δ is measured at low temperatures in a small field, the result is $\delta = 2\mu H$. However, if the field is increased at constant temperature to near $H_{c2}(T)$, δ is found to be $2\mu H(1 + G^0)^{-1}$. At higher temperatures, $\delta \neq 2\mu H$, even in small fields. The values of $\delta(T, H)$ are predicted by the theory and fitting of the measured data gives a value for G^0. This procedure has been carried out for Al by Tedrow et al. [144] and Alexander et al. [101, 145], for Ga by Gibson et al. [146], and for V by Gibson and Meservey [73].

Two methods can be used to extract $\delta(T, H)$ from the tunneling data. First, if S/I/F junctions can be made, and if b is not too large, the algebraic separation [92, 98] of the conductance versus voltage curves into spin-up and spin-down parts can be obtained from eqs. (23) and (24) and used to determine the splitting, provided we know the polarization of the ferromagnet. No recourse need be made to the theory of superconductivity. Figure 41 shows the separation into spin-up and spin-down conductance functions for an $Al/Al_2O_3/Ni$ junction at a field close to $H_{c\parallel}$. This method is usable even when there is large orbital depairing as is found near $H_{c\parallel}(T)$. If b is not small or if technical reasons preclude the making of a S/I/F junction, then δ can be obtained by fitting a theoretical conductance curve to the measured one [101]. In this case, values for the parameters b and c are also obtained, allowing calculation of $H_{c2}(T)$.

Values of δ for Al as a function of H and for various temperatures are shown in fig. 42 [144]. The diagonal line denotes $\delta = 2\mu H$. The data fall under this line for high H and T, showing that G^0 is

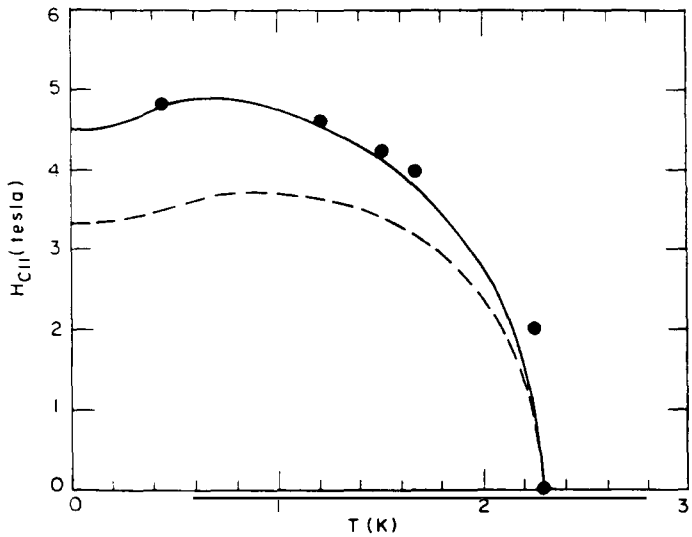

Fig. 43. Parallel critical field versus temperature (solid circles). Dashed line is the theoretical curve using the parameters $b = 0.04$ and $\zeta = 0.0043H^2$ derived from tunneling measurements. The solid curve is in the theoretical result using the renormalization suggested by Rainer [70] with $G^0 = 0.3$. The lowest temperature point is in the first-order transition region [66].

positive, i.e., the quasiparticles behave as though their magnetic moments were reduced relative to that of free electrons. Equivalently, the results indicate that the local field experienced by a quasiparticle is reduced from the value of the applied field by the antiparallel alignment of neighboring quasiparticles. We can now understand why the calculated critical field for Al films was too low when the correct value of b was used but Fermi-liquid effects were neglected. With the effective magnetic moment decreased by the Fermi-liquid effects, a higher applied field is required to produce the equivalent energy difference between spin-up and spin-down states.

We remember that spin–orbit scattering also decreases δ; however, in this case, there is also a change in the shape of the density of states for each spin direction. Thus, although one can increase the calculated H_{c2} by increasing b, one cannot simultaneously fit the tunneling conductance curves because increasing b produces a different shape from that produced by introducing G^0. Figure 43 shows a comparison of theoretical H_{c2} curves calculated using the tunneling values for b and c with and without $G^0 = 0.3$ included [66]. The curve including the G^0 parameter fits quite well. Rainer's inclusion of G^0 in the theory of H_{c2} makes it quantitatively correct.

As mentioned before, the parameter G^0 is related to the ratio between the density of states at the Fermi level $N(\chi)$ obtained from a measurement of the spin susceptibility and $N(\gamma)$ obtained from the specific heat. A spin-fluctuation model prediction gives $1 + G^0 \simeq (1 + \lambda_{ep} + \lambda_s)(1 - \bar{I})$, where the first parenthesis represents the enhancement of the specific heat due to the electron–phonon interaction and spin fluctuations while the second is from the Stoner enhancement of the spin susceptibility [146]. For Al, both these enhancements are small with $1 + G^0 \simeq 1.4 \cdot 0.9 \simeq 1.3$ in agreement with the tunneling measurements. Two superconductors with more extreme properties and which were studied using the spin-polarized tunneling technique are vanadium [73] and amorphous gallium [146]. Vanadium has a modest electron–phonon coupling constant of about 0.8, and its Stoner factor is about 0.6. Thus, the predicted value of G^0 is near zero. Amorphous gallium, on the other hand, has one of the largest values of $\lambda_{ep} = 2.25$ while its Stoner factor is estimated to be ~ 0.5. Thus, $G^0 \simeq 0.7$.

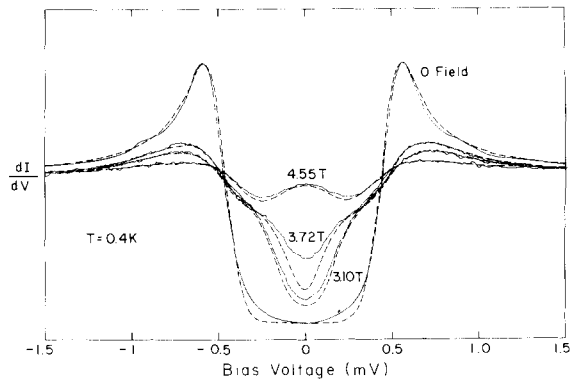

Fig. 44. Dynamic conductance versus bias voltage for an $Al/Al_2O_3/V$ tunnel junction at a number of fields. The dashed curves are fit to the theory. Here we have used $G^0 = 0$, $C_F = 0.9$, and $\alpha_0 = 0.1$. The vanadium film is 100 Å thick [73].

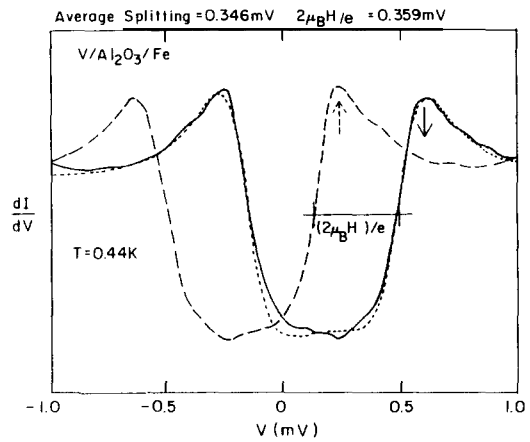

Fig. 45. Individual spin conductances of the 3.10-T curve from fig. 7 of ref. [73]. The dotted line is the prediction of the theory using the same parameters used to fit the curves in that figure. Horizontal bar represents $2\mu_B H/e$ for the applied field [73].

The vanadium junctions were made conventionally by depositing Al, oxidizing it, and then depositing 10 nm of V. Although bulk V has a T_c of 4.5 K, in very thin films the T_c is reduced, presumably due to the magnetic oxides which form readily. Figure 44 shows the measured tunnel conductance fitted by Rainer's theory. The value of G^0 obtained from the four junctions analyzed at various fields and temperatures was $G^0 \simeq 0$. Additional measurements were made with Fe counterelectrodes and were analyzed by separating the conductances for the two spin directions using eqs. (23) and (24). The results of this separation are shown in fig. 45 at one value of the magnetic field and give a value of $G^0 \simeq 0.2$, which is of the expected magnitude.

Amorphous Ga presents a different experimental problem because the films, and hence the junctions, must be made on the substrate cooled below 15 K and must be kept cold until measured or the Ga will crystallize [147, 148]. A special evaporator [146, 149], constructed to allow in situ deposition of a film onto a substrate cooled to 1 K in the bore of a Bitter solenoid, is shown in fig. 46. The substrate was first prepared with Au contact pads and the Al counterelectrode and then was mounted in the evaporator. After the junctions were formed by evaporating the Ga onto the 1 K substrate, the substrate was rotated into the parallel orientation for the high-field measurements. The films had T_c's near 8 K and $H_{c2}(0)$ near 20 T.

The tunneling data were fitted using a program based on Rainer's extension of the theory of high-field superconductivity [1, 31, 32] to include Fermi-liquid interactions [101]. The input parameters to the theory are the Fermi-liquid parameter G^0, the spin–orbit scattering rate b_{so}, and two depairing parameters [146]. Fulde's parameter [1] is $c = De^2d^2\Delta_0/\mu_B^2\hbar$ (where the diffusion constant $D = \ell V_F/3$) and α_0 is a field-independent parameter, which was found to be necessary to fit tunneling data on Al [62] and V [73]. The total depairing is then given by $\alpha = De^2d^2H^2/\Delta_0\hbar + \alpha_0$. For these films measured in high fields, α_0 was found to be negligible in the determination of G^0. Table 4 lists the properties of the Ga films. Figure 47 shows the fitting of the tunneling conductance. Because of the extreme disorder of these amorphous very thin films, effects of weak localization and Coulomb repulsion were observed and had to be corrected for before analyzing the tunneling data. Critical-field measurements and calculations are compared in fig. 48.

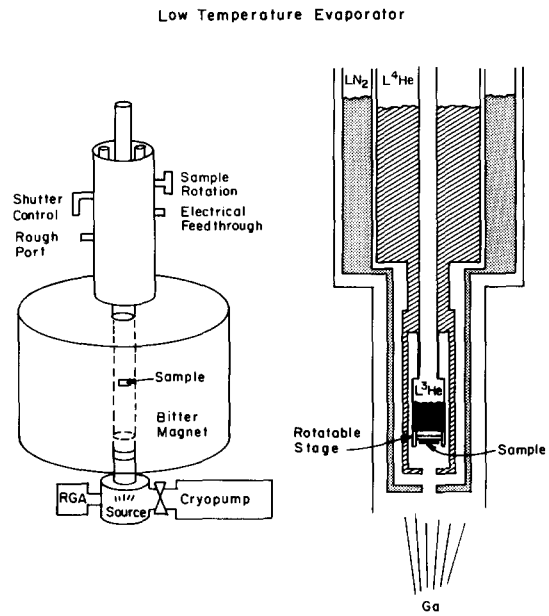

Fig. 46. Schematic view of low-temperature evaporator used to make Al/Al_2O_3/a-Ga tunnel junctions (left). Cross-sectional view of modified Janis dewar in which sample was mounted [146].

Table 4
Fitting parameters for five best amorphous gallium/aluminium junctions

Junction	G^0	b_{so}	C_F	α_0	T_c	T_{c0}
1	0.724	0.17	0.17	0.155	7.22	8.25
2	0.667	0.21	0.235	0.055	7.27	7.6
3	0.818	0.19	0.35	0.04	7.75	8
4	0.818	0.16	0.325	0.11	7.66	8.4
5	0.95	0.16	0.13	0.07	6.8	7.2

Once again, the theory proved to be quantitatively consistent and the G^0 value was of the expected magnitude. The measurements give $G^0 = 0.8$ compared to the estimate of 0.7, and the calculated critical field is in good agreement with the measured $H_{c2}(T)$.

To summarize, the high-field tunneling measurements on three disparate superconductors demonstrate the usefulness and versatility of using the superconducting state to measure parameters of the normal state which otherwise are difficult to obtain. Also, the model equation for G^0 appears to work reasonably well for this broad spectrum of materials. One might imagine that a similar study could be made by simply measuring the normal-state spin susceptibility and electronic specific heat. Unfortunately, the measured quantities contain contributions not depending on the spin densities of states, such as orbital contributions to the susceptibility and lattice contributions to the specific heat. Separating out the various contributions is not straightforward. The tunneling method has the advantage of using very little theoretical input to obtain a unique value of G^0.

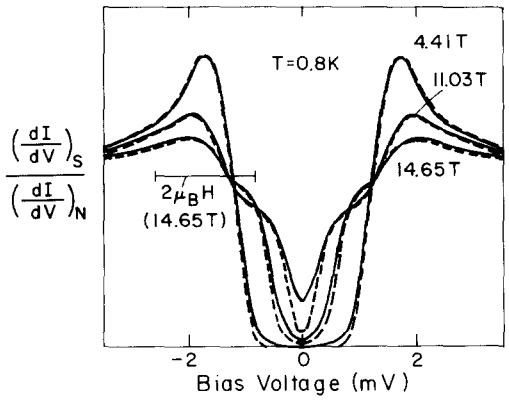

Fig. 47. Data of fig. 7 in ref. [146] with measured background conductance divided out. The horizontal bar represents $2\mu_B H$ at 14.65 T. The splitting observed at this field is clearly much less than $2\mu_B H$ [146].

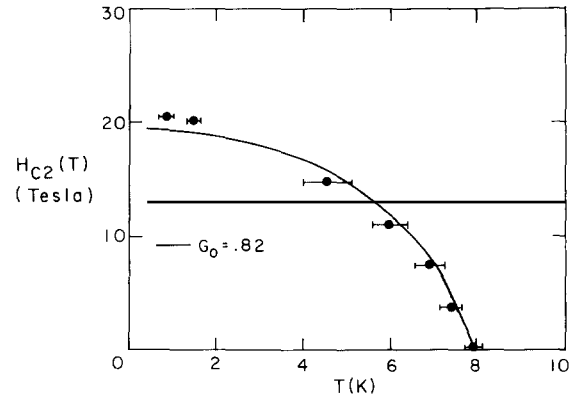

Fig. 48. Critical-field data for gallium film of junction used in figs. 7 and 9 of ref. [146]. The solid curve is the prediction of Rainer's theory using the parameters obtained from the tunneling data. ($G^0 = 0.818$, $b_{so} = 0.16$, $C_F = 0.325$, and $\alpha_0 = 0.11$) [146].

5. Exchange effects at interfaces and barriers

5.1. *Exchange interaction proximity effects*

Because magnetic order and superconductivity are often incompatible, the interaction between superconductivity and magnetism has been a topic of interest for many years. The depairing effect of magnetic impurities in conventional superconductors was understood through the work of Abrikosov and Gor'kov [150] and others [151]. Exotic magnetic field behavior has been found in superconductors with rare-earth components such as the rhodium borides [152] ternary molybdenum chalcogenides [153], and $CePb_3$ [154]. A tunneling experiment using a $Ho(OH)_3$ barrier between two Pb films has been interpreted as showing the formation of a bound state in the Pb because of the ferromagnetism of the barrier [155]. The observations of interest here, which we call the exchange proximity effect, stem from the discovery that a thin Al film in contact with a ferromagnetic semiconductor behaves like a BCS superconductor with a uniform exchange field [156]. This discovery, supported by an earlier theoretical description by de Gennes, [157], provided the impetus for a number of tunneling experiments exploring the ramifications of the behavior of a thin-film superconductor in contact with a plane of magnetic material.

5.1.1. *First demonstration of the exchange proximity effect*

Experiments were performed first on thin Al films in contact with EuO in tunnel junctions of the form EuO–Al/Al_2O_3/Al (or Ag, or Fe) [156]. Europium metal (5 nm thick) was first deposited on a glass substrate at 77 K and, after warming to 300 K, was treated with an oxygen glow discharge to form EuO. The Al film (4–10 nm thick) was then deposited at 77 K, warmed to 300 K, and partially oxidized in a glow discharge to make the tunnel barrier. The final Al film (4–10 nm thick) was then deposited at 77 K. The use of low-temperature depositions was necessary to produce reasonably uniform films at these thicknesses. EuO is a ferromagnetic semiconductor with a Curie temperature of 69 K, but it is probable that the more stable compound Eu_2O_3 (an antiferromagnet) was also present in the films.

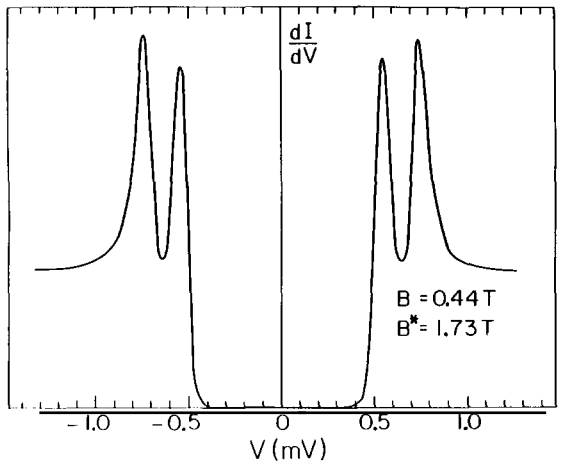

Fig. 49. Measured tunneling conductance versus voltage for a EuO–Al/Al_2O_3/Al junction with an applied field of 0.44 T and a voltage splitting equivalent to 1.73 T. After [156].

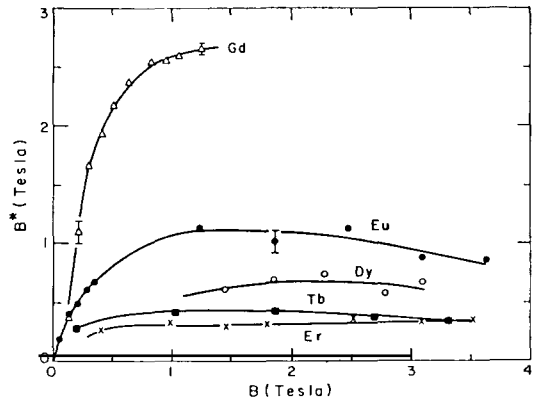

Fig. 50. Enhancement B^* of the applied field B as obtained from spin-polarized conductances for several rare-earth oxides. After [158].

For an Al/Al_2O_3/Al junction without the EuO, the tunneling conductance at low temperatures shows only two sharp peaks at voltages $V = \pm 2\Delta/e$, as shown in fig. 19, even in a magnetic field which spin-splits the densities of states. The reason is that, as explained in section 2.3, the spin splitting in the two films is identical. (The very small spin–orbit peak shown in fig. 20 is too small to be seen at this scale). On the other hand, fig. 49 shows the tunnel conductance versus voltage for a EuO–Al/Al_2O_3/Al junction in a parallel magnetic field of $B = 0.44$ T [156]. There are two distinct peaks in each voltage direction, which imply that the EuO–Al film has a spin splitting equivalent to that of an applied field of $B + B^* = 0.44 + 1.73$ T! In addition, the sharpness of the peaks indicates that the magnetic field depairing is no greater than that due to the actual applied field.

This result can be interpreted by referring to fig. 19, but with the superconductor in contact with the EuO acted on by an additional effective field B^*, resulting in a splitting of each conductance peak by $2\mu B^*$. A plot of this additional field acting on the electron spins as a function of the applied field is shown in fig. 50 for EuO and other rare-earth oxides [158]. The fact that the value of B^* in high fields is fairly close to the saturation magnetization M of the ferromagnet appears to be a coincidence, and it is thought that this effect is caused by an exchange interaction between conduction electrons in the Al and the EuO moment. This view is supported by the fact that the high-field value of B^* is inversely proportional to the film thickness d as predicted for an exchange model proposed by de Gennes [157]. The model can also account for the size of the splitting within an order of magnitude. Also, the fact that the tunnel curves of the superconductor with enhanced splitting are not additionally depaired (see fig. 49) shows that this superconductor is not subjected to an additional real magnetic field. Finally, measurements with EuS showed that the value of B^* actually could exceed M [159]. The slight decrease of B^* at high applied fields (fig. 50) is attributable to the well-understood Fermi-liquid corrections to the magnetic moment of the Al quasiparticles [144] (see section 4). It was found that 2 nm of Al_2O_3 between the rare-earth oxide and the Al destroys the effect as one would expect from an exchange interaction model. Rainer and co-workers [160] also have analyzed this system on the basis of an exchange interaction.

As summarized by Tkaczyk [79], there are three physical effects which are observable consequences of the exchange proximity effect. If the rare-earth moments are aligned, there is an

interaction of the form $\langle k\sigma/H_{ex}/k\sigma\rangle$ which has the effect of splitting the density of states of the superconductor just as an applied magnetic field does. Here H_{ex} is the s–d exchange Hamiltonian. This effect is what was observed in the initial experiments. There are also non-spin-flip first-order contributions of the form $\langle k'\sigma/H_{ex}/k\sigma\rangle$ which lead to the well-known RKKY [109] response causing a spin polarization of the conduction electrons proportional to $\int d\boldsymbol{r}'\chi(\boldsymbol{r}-\boldsymbol{r}')\,B_{ex}(\boldsymbol{r}')$, which is localized within about one Fermi wavelength of the interface. Here, χ is the spin susceptibility of the electron system and B_{ex} is the effective exchange field. Both of these effects are linear in the exchange coupling J. Finally, there is spin-flip scattering which depends on J^2. In zero applied field, the spin-flip scattering rate τ_{ex}^{-1} is that calculated by Abrikosov and Gor'kov [150]. Spin-flip scattering decreases T_c and broadens the density of states. Fitting the AG theory to the tunneling conductance is a good way to measure τ_{ex}^{-1}.

5.1.2. Exchange splitting with rare-earth oxides

One expects from de Gennes' theory [157] that the superconducting Al in contact with a ferromagnetic semiconductor would have Zeeman splitting of the density of states in zero applied field. In fact, in many experiments with EuO, no such splitting was observed when the field was first applied. However, in some cases, splitting was observed in zero field after the application and removal of a field of a few kG. These results are probably attributable to imperfections of the EuO films. Since EuO is not as stable as the non-ferromagnetic oxide Eu_2O_3, some Eu_2O_3 is presumably present. In addition, the thinness and low-temperature deposition are expected to give the films a fine-grained structure, which will limit the magnetic domain size. For domains smaller in size than the superconducting coherence length (which is about 50 nm for these Al films), cancellation of differently directed domains will leave a small net exchange field and little splitting. The application of a magnetic field can align these domains, allowing the proximity-induced splitting to be observed. We notice from these results that the splitting observed while the field is applied is not dependent on whether or not the magnetic material is ferromagnetic, as long as the field is large enough to align the moments. The increase of B^* shown for the (mostly antiferromagnetic) materials in fig. 50 is a manifestation of this alignment effect. The saturation value of B^* can be correlated to some extent with the properties of the particular rare-earth atoms involved. The largest effects are seen with Eu and Gd, which have the largest spins in the rare-earth series. The saturation value then dies off roughly with decreasing spin. Why Tb produces so small an effect is not understood at this time; however, the nature of the interface between the superconductor and the magnetic material is very important. If the contact is not sufficiently good, the proximity effect will not be observed.

For EuS, which can be deposited without major stoichiometric imperfections, Moodera et al. [159, 161] discovered that Zeeman splitting of the density of states of superconducting Al is often observed before any field is applied provided the Al/EuS interface is clean. Even in this case the splitting rapidly increases with applied field as the domains align and increase in size compared to the coherence distance in the superconductor. Experiments with EuS and EuSe will be described in section 5.2.

5.1.3. Rare-earth metals

Because the state of order of the rare-earth atoms does not affect the splitting with a magnetic field applied, Tkaczyk reasoned that one could use metallic rare-earths as well as the oxides. A further complication enters the experiment, however, because metallic magnetic atoms exert a strong detrimental effect on the superconducting state. The depairing effect of magnetic impurities was first demonstrated in tunneling experiments and in measurements of the depression of T_c

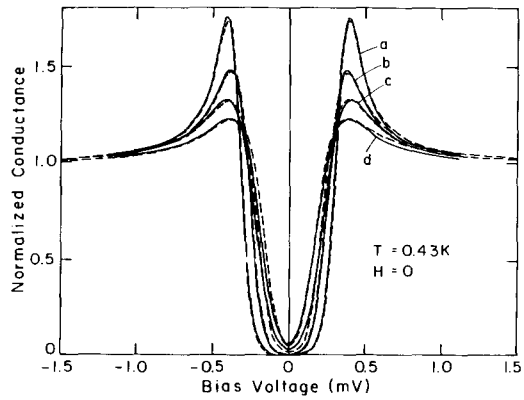

Fig. 51. The measured tunneling conductance (solid curve), and fits by the AG theory (dashed curves a–d) of Gd–Al/Al_2O_3/Ag junctions corresponding to Gd coverages of 0, 1, 2, and 3 nm^{-2}, respectively. After [164].

by Reif and Woolf [162]. The effects of magnetic impurities on superconductivity have since been studied in detail [163]. The physics of this strong dependence on spin-flip scattering was explained theoretically by Abrikosov and Gor'kov [150, 151], whose prediction of the density of states of the superconductor can be used to fit tunneling results in which spin-flip scattering is present. This form of the density of states must be used for understanding the following experiments in which a very small amount of the rare-earth metal itself is in contact with the Al film. Figure 51 illustrates the effect of different thicknesses of Gd metal and fits of the AG theory to the conductance curves [79, 164]. The tunneling conductance broadens with increasing Gd coverage and the shape of the curves is well described by the AG theory. The curves clearly show that a submonolayer of Gd 0.05 nm thick acts like a metallic impurity and completely different from the oxide.

A by-product of this fitting procedure is a value for the spin-flip scattering time. When these junctions are then subjected to a magnetic field, the resultant splitting of the density of states yields a value for B^*. Tkaczyk [79] developed a method for analyzing these two pieces of information by noticing that $B_{ex} \sim cJB_s(\eta)$ while $\tau_{ex}^{-1} \sim cJ^2$. Here c is the concentration of magnetic atoms, B_s is the Brillouin function and $\eta = \mu B/kT$. If one plots the saturation $B^*(\sim B_{ex})$ versus the scattering rate measured from the zero-field tunneling conductance, one should obtain for each magnetic material straight lines of constant J radiating from the origin, with the distance along a line a measure of the concentration c. Because the impurities are non-interacting, it is important to obtain the saturation value of B^*. This measurement must sometimes be made indirectly because B^* may exceed the critical field of the superconductor. One then fits the Brillouin function to the B^* data to get the saturation field. An example is shown in fig. 52, where B^* versus $B_{applied}$ is shown for three Gd concentrations [164]. The critical field of the Al is near 4 T, so that the extrapolated saturation value of $B_{ex} = 8.1$ T cannot be observed directly. An example of B_{ex} versus τ_{ex}^{-1} for Eu and Gd is shown in fig. 53 [79]. This figure also illustrates that the main difference between measurements using oxides and those using metallic impurities is the effective concentration.

5.1.4. Observation of the RKKY polarization

The experiments which we have discussed so far concerning the exchange proximity effect have involved tunneling into the side of the superconductor away from the magnetic layer. In this section, we review results of experiments in which the tunnel junction is formed on the same side of the film as the rare-earth dopants [79, 165]. This geometry allows the polarization of the

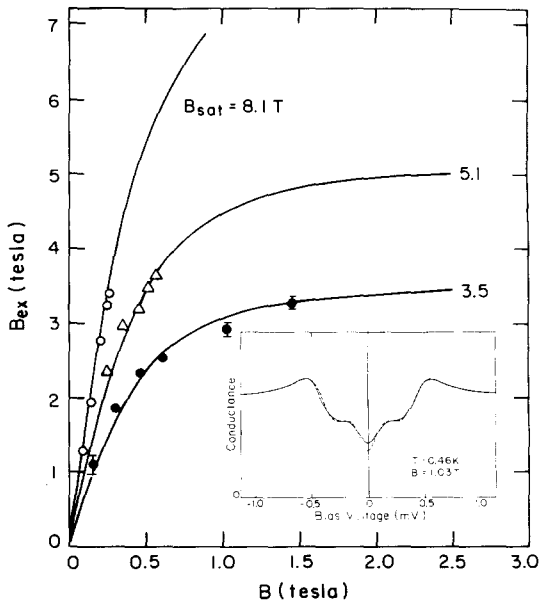

Fig. 52. The uniform exchange field as a function of the applied magnetic field obtained from the Zeeman splitting of the conductance for the junctions corresponding to curves b, c, and d in fig. 51. The curve drawn through the points corresponding to the lowest Gd coverage saturates at $B_{ex} \simeq 3.5$ T. This curve was scaled by a constant factor to obtain the saturation curves for the greater coverages. Inset: The Zeeman splitting of the conductance for the lowest Gd coverage and a fit (dashed) by the theory with no spin-flip scattering [164].

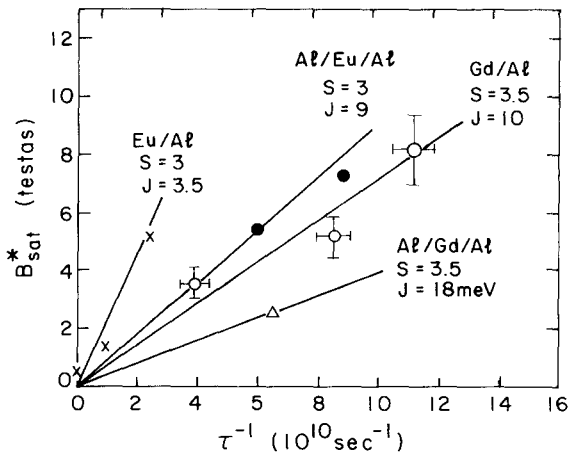

Fig. 53. The exchange constant is determined by plotting B^* versus τ_{ex}^{-1} for Eu at the surface (x), Eu inside (●), Gd at the surface (○), and Gd inside (△) of a 40 Å Al film. After Tkaczyk [82].

conduction electrons due to the RKKY [109] interaction to be observed. As was mentioned earlier, this interaction is localized at the interface between the superconductor and the magnetic layer and extends into the superconductor only a distance comparable to a Fermi wavelength. An added feature of the experiments arises from the fact that the spin susceptibility of the superconductor goes to zero when the spins are paired in the superconducting state. As we have seen, the polarization depends on the spin susceptibility, and thus must vanish in the superconducting state of a spin-paired superconductor. The junctions used in this part of the study are of the form $Al/Al_2O_3/Gd$–Al.

Figure 54 shows the conductance of such a junction at two different values of applied magnetic field. In curve (a), both Al films are in the superconducting state. The curve is symmetrical about zero voltage, and the peak at the sum of the gaps is split because the top Al film is in contact with the Gd. When the field is increased above the critical field of the Gd–Al film, however, the conductance (curve b) becomes asymmetric and looks similar to the curves we have seen earlier in the section on tunneling into ferromagnetic metals. In this case, the observed polarization is a few percent. This experiment bears out our expectation that the polarization caused by the RKKY interaction can be seen in the normal state but not in the superconducting state. To further investigate this phenomenon, we recall that we can alter the spin susceptibility of the superconductor by adding spin–orbit scattering with a submonolayer of Pt on the Al [66]. A junction of the form $Al/Al_2O_3/Al$–Pt (with no Gd) in a magnetic field has a conductance as shown in fig. 55 [165]. Now the peak at the sum of the gaps is split because the density of states of the Al–Pt film does not

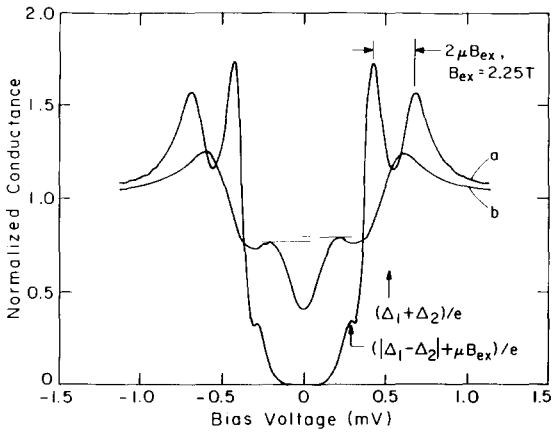

Fig. 54. The conductance of an $Al/Al_2O_3/Gd$–Al junction (3 Gd ions/nm^2) measured in an applied magnetic field for which the top electrode (Gd–Al) is (curve a) superconducting, $B = 0.17$ T, and (curve b) normal, $B = 3.72$ T [164].

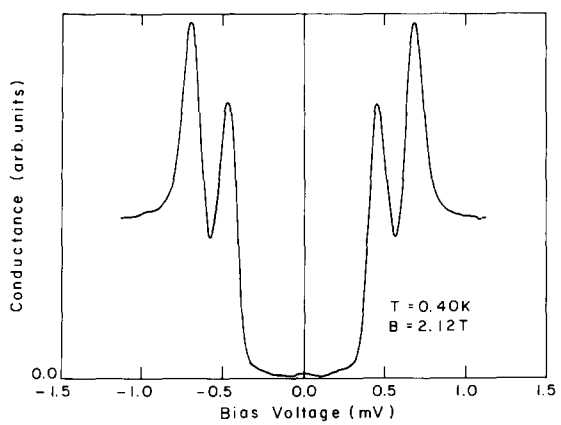

Fig. 55. The conductance of an $Al/Al_2O_3/Al$–Pt junction, where two monolayers of Pt mix the spin states of the electrons in the Al-Pt electrode. The voltage splitting of the sum-of-the-gaps peak corresponds to the Zeeman splitting of the electrons in the Al electrode, $2\mu B = 0.25$ meV [165].

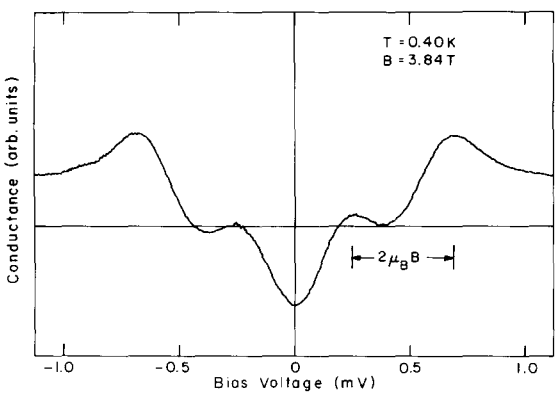

Fig. 56. The conductance of an $Al/Al_2O_3/Gd$–Al–Pt junction measured in a magnetic field where only the Al electrode is superconducting. The asymmetry with respect to zero bias is associated with a spin polarization of the electrons in the Gd–Al–Pt electrode [165].

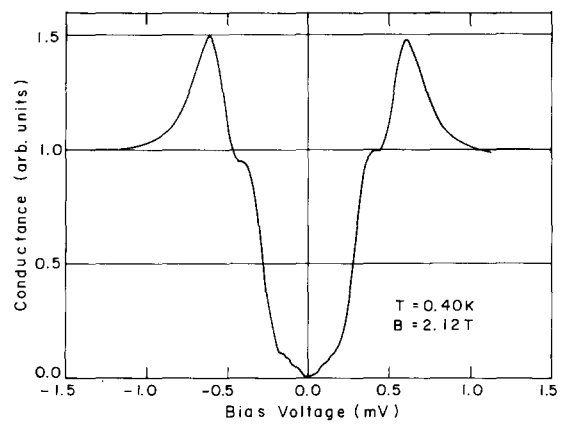

Fig. 57. The conductance of the same junction used in fig. 56 but at a lower magnetic field for which both electrodes are superconducting. The asymmetry indicates a spin polarization of the electrons in the Gd–Al–Pt electrode. The conductance of the corresponding control junction (i.e., no Gd) is shown in fig. 55 [165].

split in the applied field. Note that the peaks are sharper in this case compared to those in fig. 54, because there is no depairing due to the presence of a magnetic material in this case. Now if Gd is added to the junction of fig. 55, the conductance becomes as shown in fig. 56 [165]. When the field exceeds the critical value for the Gd–Al–Pt film, the asymmetrical polarized S/I/N conductance is observed as before. This time, however, when the field is reduced below the critical value, the conductance remains asymmetrical with the same value of polarization as shown in fig. 57 [165]. Thus, the theoretical expectations are in fact borne out by the experiments.

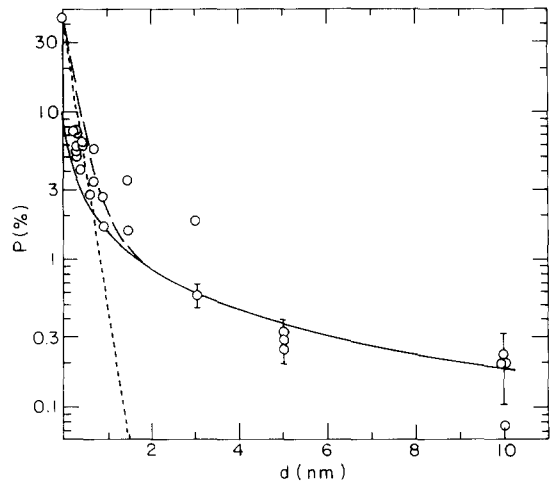

Fig. 58. Measured polarization P versus average thickness d of the Au layer covering Fe. Solid and long-dashed lines give P as calculated for two limits of the proposed model. The small dashed line is expected for random Au deposition and no spin leakage into the Au [166].

5.1.5. *Ferromagnetic-metal–nonmagnetic-metal interface*

In a different sort of experiment, Mooderal et al. [166] have used spin-polarized tunneling to conclude that, in a thin film of Au covering an Fe film, the conduction electrons in the Au are partially spin polarized by an exchange interaction at the Fe/Au interface. The values of P at the Au surface varied inversely as the Au thickness and could be detected to a thickness of 10 nm, as shown in fig. 58. The proposed explanation of the effect is that conduction electrons in the Au are polarized by the scattering at the Fe–Au interface and remain polarized until there is a spin-scattering collision, most probably at the Au surface. The polarization of the conduction electrons would therefore decrease inversely with the Au thickness for essentially the same reason as in the de Gennes [157] analysis of a ferromagnetic insulator–superconductor interface. It is to be emphasized that this is an equilibrium spin polarization of the *conduction* electrons in the Au, but implies no ferromagnetic interaction in the Au.

5.1.6. *Spin dependence of the superconductor–normal-metal proximity effect*

When a superconductor is placed in intimate contact with a normal metal, the superconductivity leaks into the normal metal for a distance whose scale is given by the coherence length. This intrusion of superconducting properties into the normal metal is called the proximity effect [2]. Gallagher et al. [167] have investigated the spin properties of the quasiparticles in a proximity-effect double layer. This effect is different from the exchange proximity effect described earlier in that both materials are metallic and no magnetic ions are involved. The phenomena predicted arise only from the superconducting interactions experienced by the quasiparticles as they move from one metal to the other. The motivation for the study was partly due to the existence of the tricritical point in the magnetic field behavior of thin superconductors with low spin–orbit scattering, mentioned in section 2.2. The theory of the proximity effect in a thin double layer in a magnetic field then was analogous to that of other systems in which a staggered field was present [167]. Properties such as spin susceptibility and densities of states were calculated for both sides of the sandwich. The most relevant result for this review was the prediction that the density of states of the normal metal would be split by the magnetic field in response to the splitting of the density of states

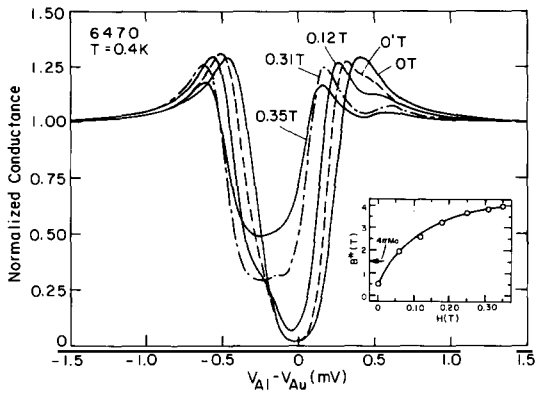

Fig. 59. Normalized dynamic conductance $(dI/dV_{SN})/(dI/dV_{NN})$ in various applied magnetic fields for a Au/EuS/Al junction. The curve taken in zero field (0 T curve) shows a small internal field which can be determined by fitting the curve to theory; B_i^* is found to be 0.5 T. Remanent Zeeman splitting corresponding to an internal field of about 2.0 T is seen in this junction (0′ T curve). The inset shows the dependence of the internal field on the applied field. The saturation magnetization of EuS, $4\pi M_0 = 1.5$ T, is indicated by an arrow [159].

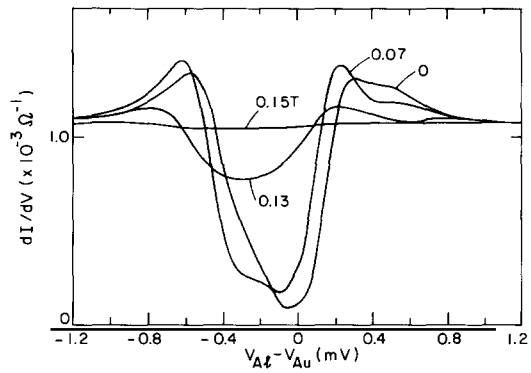

Fig. 60. Conductance versus voltage for a Au/EuS/Al junction at $T = 0.4$ K for various values of H. A fit of theory to the curves gives $P = 80\% \pm 5\%$. Note the high value of zero-field splitting. Curves were all taken in increasing field. Hysteresis was observed in decreasing H, but is not shown [161].

on the superconducting side, and, furthermore, that at high fields, the splitting could be large enough to cause states to cross the Fermi level. This crossing arises from the reduced gap on the normal side combined with the usual magnitude of the splitting. The superconductivity of the other half of the sandwich maintains the superconducting state throughout. Calculations of the resulting tunneling conductance were made, the salient feature of which is a peak in the conductance at zero bias as the magnetic field approaches H_{c2}. Experiments on Mg–Al sandwiches demonstrated the existence of this peak [167].

5.2. *Spin-filter tunnel barriers*

When EuS was used as a tunnel barrier in Au/EuS/Al junctions, not only was there splitting of the Al density of states, but the tunnel current was strongly spin polarized [159, 161]. This is illustrated in fig. 59 for a junction in which Au 11 nm thick was covered by EuS 3.3 nm thick, both deposited at room temperature, followed by deposition of the 4.2 nm Al counterelectrode at 77 K. When the tunneling conductance was measured at 0.5 K, there was initially a small spin splitting ($B_i^* = 0.5$ T) before any magnetic field was applied and a greatly enhanced splitting appeared at higher fields. When the field was again reduced to zero, shown in curve 0′, the remanent splitting ($B^* = 2$ T) was much larger than the initial value. The inset in fig. 59 shows the value of the enhanced field B^* as a function of the applied field. One result is that B^* exceeds greatly the value of the saturation magnetization of bulk EuS (= 1.5 T) and unambiguously confirms the assumption that the observed effect is that of an exchange interaction and cannot be attributed to the magnetic field of the ferromagnet.

The polarization obtained by fitting the curves of fig. 59 to theory is $P = 80 \pm 5\%$ [159]. A Ag/EuS/Al junction with $P = 85\%$ had the highest value of initial zero-field splitting, $B_i^* = 3$ T, as shown in fig. 60 [160]. In previous spin-polarized tunneling studies, polarization of the tunnel current comes from the different densities of spin-up and spin-down conduction electrons at the

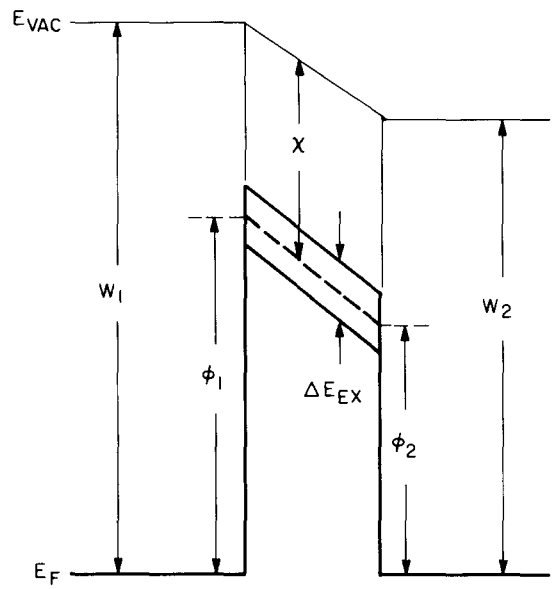

Fig. 61. Schematic representation of the tunnel barrier of a Au/EuS/Al junction. W_1 and W_2 are the work junctions of Au and Al, respectively. χ is the electron affinity of EuS. The barrier heights in the Au and Al interfaces are shown as ϕ_1 and ϕ_2 at the bottom of the EuS conduction band (dashed line) at $T > 16.7$ K. The bottom of the two bands shown at $T \ll T_c$ by the solid lines separated by $\Delta E_e x$ are the barriers seen by the two spin directions [161].

Fermi level in the ferromagnetic electrode. In the present case, the polarization arises from different barrier heights for electrons with different spin orientation, when the conduction band of EuS splits into spin-down sub-bands below the Curie temperature $T_c = 16.6$ K. In the schematic diagram of fig. 61, ϕ_1 and ϕ_2 are the barrier heights on the Au and Al sides of the barrier and the dashed line shows the bottom of the unsplit conduction band at $T = 20$ K. For $T \ll T_c$ the solid lines show the barrier height for the two spin directions split in energy by ΔE_{ex}. Since the tunneling process depends exponentially on the barrier height, the splitting of the EuS conduction band greatly increases the probability of tunneling for spin-up (majority) electrons and reduces that of the spin-down (minority) electrons.

Several previous studies of this spin-filter effect are closely related to the tunneling results. Esaki et al. [168] reported an internal-field-emission study of junctions having the magnetic semiconductors EuS and EuSe as barriers 20–60 nm thick. They observed an increase of internal field-emission current as the temperature was lowered to below the magnetic ordering temperature of the barrier and interpreted this change as caused by the decrease in barrier height when the conduction band is split by the exchange interaction below the Curie temperature (T_c). Other tunneling results were obtained by Thompson et al. [169]. Field-emission studies by Müller et al. [170] and Kisker et al. [171] on EuS-coated tungsten tips showed a high degree of polarization of the field-emitted electrons below the Curie temperature of EuS and were explained by a spin-filter effect in EuS caused by the exchange splitting of the conduction band.

The spin polarization of the tunneling electrons was obtained by fitting the conductance curves to the Maki–Fulde–Rainer theory as previously described. All of the curves for one junction were fitted with a single value of polarization P, but B^* was varied for different applied fields. Theoretical fits were made to three of the conductance curves shown in fig. 60. The value obtained for the polarization for this junction was $80 \pm 5\%$. Table 5 contains the values of the polarization

Table 5
Comparison of values of polarization. P_{meas} is obtained from the tunnel conductance asymmetry. P_{calc} is calculated from Simmons' theory and the optically measured ΔE

Junction	P_{meas} (%)	P_{calc} (%)	$\frac{R_J(2\,K)}{R_J(35\,K)}$	$R_J(2\,K)$ (kΩ)	S (nm)	ϕ_0 (eV)
Au/EuS/Al	80 ± 5	84.9	0.51	0.3	17.8	1.56
Ag/EuS/Al	85 ± 5	90.8	0.40	0.47	19.8	1.32
Al/EuS/Al	85 ± 5	91.6	0.38	2.2	20.4	1.32
Al/EuS/Al	85 ± 5	92.6	0.36	14.4	21.9	1.42
Al/EuS/Al	60 ± 5	80.4	0.58	3.0	17.6	1.96

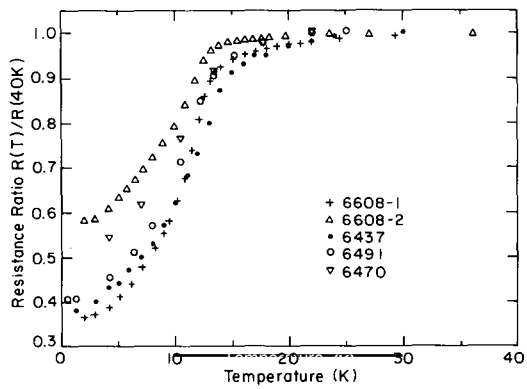

Fig. 62. Junction resistance as a function of temperature. The sharp decrease of R_J indicates the onset of the ferromagnetic transition in the EuS barrier, which is approximately between 14 to 15 K for these films [159].

obtained from this fitting process (which we have designated P_{meas}) for 5 different junctions for which resistance versus temperature was also measured (fig. 62) [159, 172]. For all of these junctions the EuS was deposited at 300 K; deposition of the EuS at 80 K gave lower values of P. It is important to realize that the values of P_{meas} depend entirely on the superconducting properties and contain no assumptions as to the barrier or other electrode except assuming that the tunneling is elastic, for which there is strong evidence [62].

Completely independent from the above analysis, we can obtain another value of the polarization (designated P_{calc} in table 5) based on Simmons' [173] approximate expression for the tunnel current density J as a function of the bias voltage V and the height ϕ and width s of a trapezoidal tunnel barrier as illustrated in fig. 62:

$$J = J_0(\phi - \tfrac{1}{2}eV)\exp[-A(\phi - \tfrac{1}{2}eV)^{1/2}] - J_0(\phi + \tfrac{1}{2}eV)\exp[-A(\phi + \tfrac{1}{2}eV)^{1/2}], \qquad (31)$$

where $J_0 = (e/2\pi h)S^{-2}$ and $A = (4\pi S/h)(2m)^{1/2}$ with S being the thickness of the barrier, h Plank's constant, and m the electron effective mass in the conduction band. In these calculations the free-electron mass was used. The values used for ϕ_0 and S to fit the current versus voltage curves well above T_c according to the Simmons theory are shown in table 5.

For $T \ll T_c$ the conduction band of EuS is split by the exchange interaction and the barriers for spin-up and spin-down electrons become $\phi\uparrow = \phi_0 - \frac{1}{2}\Delta E$ and $\phi\downarrow = \phi_0 + \frac{1}{2}\Delta E$. Using eq. (31)

and the bulk value of exchange splitting $\Delta E = 0.36\,\text{eV}$ [174], we can calculate the spin-up and spin-down current densities $J\uparrow$ and $J\downarrow$. The calculated polarization is then

$$P_{\text{calc}} = (J\uparrow - J\downarrow)/(J\uparrow + J\downarrow)\,. \tag{32}$$

The values of P_{calc} are listed in table 5 and are in reasonable agreement with P_{meas} obtained from superconducting tunneling theory. The values for ϕ_0 from fitting the current–voltage curves for $T \gg T_c$ are much lower than the values obtained from the known properties of bulk EuS. Using the values for the work functions $W_{\text{Al}} = 4.1\,\text{eV}$ and $W_{\text{Au}} = 5.0\,\text{eV}$ [175], and the electron affinity for EuS, $\chi_{\text{EuS}} = 2.5\,\text{eV}$ [176], we infer values of the barrier heights at the interfaces of $\phi_1 = 2.5\,\text{eV}$ and $\phi_2 = 1.6\,\text{eV}$. The average barrier height would be $\phi = (\phi_1 + \phi_2) = 2.05\,\text{eV}$. The average of the rather variable values of ϕ_0 in table 5 is 0.4 eV less than the theoretical value from bulk EuS. This difference probably reflects the structural imperfections of the 3.3 nm films of EuS and is generally found in barrier heights of vapor-deposited barriers.

As a result of the exchange splitting of the barrier height in EuS, there is a large decrease in the resistance of the tunnel junction at temperatures below T_c as shown in fig. 62. We can compare these measurements with the calculated fractional change in resistance obtained by using eq. (31),

$$R(T)/R(40\,\text{K}) = [J\uparrow(40\,\text{K}) + J\downarrow(40\,\text{K})]/[J\uparrow(T) + J\downarrow(T)]\,.$$

The resistance above T_c was taken at 35 or 40 K, which are above the region in which transition width and fluctuation effects are present. Values for this resistance ratio as measured and calculated are given in table 5. The agreement of the measured and calculated values can be considered good even though the theoretical decrease in resistance at 2 K is about 10% greater than the measured values.

Other metal electrodes that were used in place of Au are Ag, Al, and Fe. A film of VTi was used in place of thin Al. The results with Ag were very similar to those obtained with Au. An increase in polarization when using Fe was expected but not observed, although this result may be attributable to surface contamination. With an Al film deposited first at 80 K followed by a EuS film and another Al film, it was usually found that only the top Al film was Zeeman-split by the exchange interaction. Apparently a thin layer of Al_2O_3 was formed on the first-deposited Al film and prevented direct contact between the Al and the EuS which is needed for an exchange interaction. It was difficult to prevent the formation of the Al_2O_3 because, to form thin uniform Al films, the substrate was cooled and then warmed to 300 K for the EuS deposition, a procedure taking two hours and inviting condensation of water vapor at the 10^{-8}–10^{-7} torr system pressure. Since the layers of Al_2O_3 were at most a few monolayers, this result is consistent with the assumed exchange interaction. Further experiments in vacuums of 10^{-10}–10^{-11} torr are needed to complete this study. A Ag/EuS/VTi junction showed Zeeman splitting of the VTi as well as asymmetry from the spin-filter effect [159]. However, because of very high leakage current, no value of spin polarization could be obtained.

When both electrodes were Al, the tunneling conductance was characteristic of superconducting/superconducting junctions with the Al film deposited on the EuS having an enhanced Zeeman splitting. The conductance at $H = 0$ for two different junctions is shown in fig. 63 [159]. For a bias voltage of either sign there is one difference peak and two sum peaks predominantly of the spin direction indicated by the arrows. Varying the top Al thickness d from 4 to 14 nm allowed the

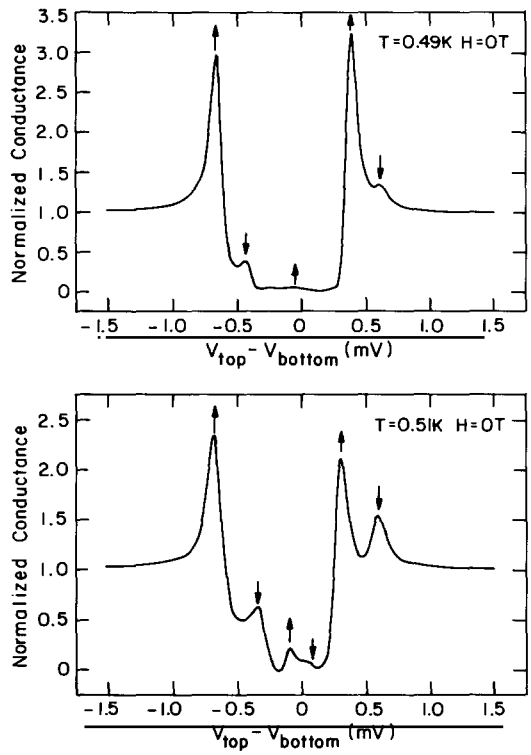

Fig. 63. Normalized S–I–S tunnel conductance curves for two Al/EuS/Al junctions (made in the same evaporation) in zero applied magnetic field. The spin directions of the peaks are labeled by the up or down arrows. $B_i^* = 1.9\,T$ and $P = 85\%$ for sample 4 (table 5), and $B_i^* = 2.6\,T$ and $P = 60\%$ for sample 5 [159].

magnitude of the saturation exchange field B^* to be measured as a function of d as shown in fig. 64 [177]. The approximate variation of B^* proportional to $1/d$ agrees with the prediction of de Gennes [157] for a superconducting film between two ferromagnetic insulators and with data of Tkaczyk using EuO [79].

By fitting the tunneling conductance curves to the Maki–Fulde theory, values for the superconducting order parameter were obtained as a function of the total applied effective field acting on the Al quasiparticles. Figure 65 shows a plot of the square of the reduced order parameter as a function of the square of reduced effective field [177]. For the thinner films, the rapid decrease of Δ near T_c is indicative of a first-order transition caused by the exchange field, whereas the behavior of the thicker films is consistent with a second-order transition to the normal state. Additional evidence for a first-order transition in the thinner films is seen in the sudden appearance of a peak at zero voltage in the conductance curves just before the Al becomes normal with applied field. This peak is the result of the partial coincidence near H_c of the two inner peaks formed by the Zeeman splitting as previously shown by measurements of V–Ti alloys in fig. 14 [63] and of vanadium [73]. These results show that a first-order transition can be induced by the exchange field acting only on the electron spins and can be observed at greater thickness of the superconductor than with only an applied magnetic field and could perhaps be applied to the study of the spin properties of other superconductors at very low applied fields

EuSe, another magnetic semiconductor, has in bulk single-crystal form a rather complicated phase diagram at low temperatures at $H = 0$, having a transition to antiferromagnetism at 4.6 K,

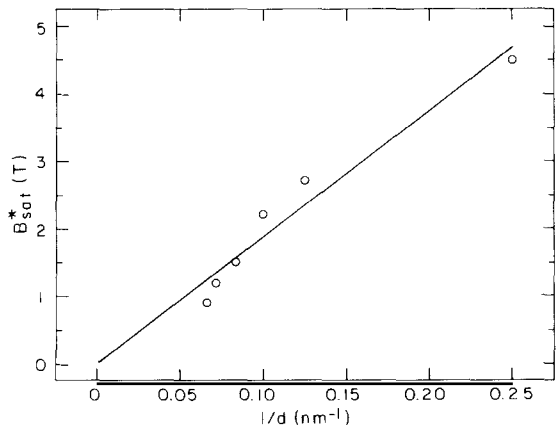

Fig. 64. The dependence of the saturation internal field on the Al film thickness. The line in the figure is a least-squares fit to the data points [177].

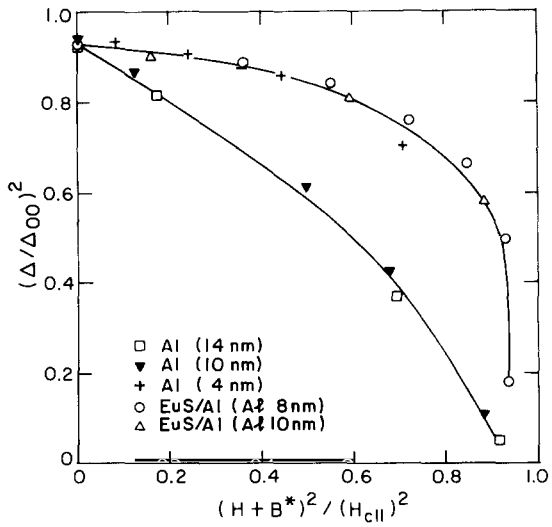

Fig. 65. The square of the reduced order parameter plotted against the square of the reduced field. The data points show that the 10 and 14 nm thick Al films become normal through a second-order transition, which is expected from theoretical calculations. The superconductor–normal transition in the EuS/Al bilayers (each with 8 and 10 nm of Al, respectively) and in a 4 nm thick Al film is of first order as indicated by the sharpness of the transition near the critical field [177].

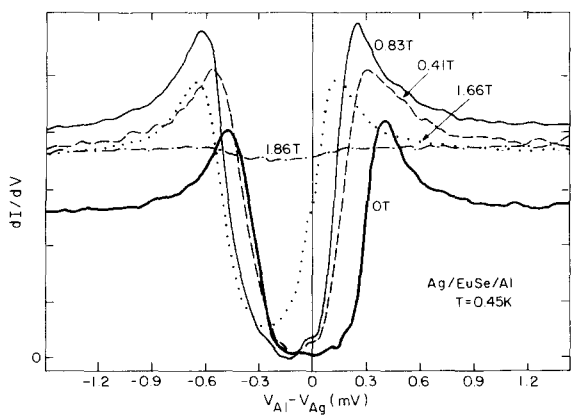

Fig. 66. Conductance versus voltage bias in a Ag/EuSe/Al junction for various applied magnetic fields for a high resistance tunnel junction showing only spin-up peaks, indicating near 100% electron spin polarization [179].

a transition to a ferrimagnetic state at 2.8 K [178], and a transition to another antiferromagnetic state at 1.8 K [178]. Recent experiments with thin films have demonstrated Zeeman splitting of Al films in contact with EuSe in all but the lowest applied fields in which the EuSe is presumably antiferromagnetic. At fields above 0.1 T, EuSe is ferrimagnetic below about 1.8 K and polarizations as high as 97% have been observed in a field of 1.2 T [179]. The very high values of spin polarization sometimes observed are perhaps the result of a low effective tunnel barrier height, which accentuates the effect on the barrier height by the exchange splitting. Figure 66 shows the

conductance of a EuSe barrier in which the spin-down peaks are only marginally visible and which has a polarization close to 100% [179].

With EuSe, the value of P increased with magnetic field, in contrast to EuS (or metallic ferromagnetic counterelectrodes) where the value of P remains essentially constant from very low fields, even though B^* increases with field [179]. EuS is a ferromagnet whose domains have a constant value of magnetization which is only aligned by the field. For EuSe the value of the domain magnetization apparently increases with field. On the other hand, if there is no ferromagnetic exchange interaction between moments as with a Gd_2O_3 barrier, which is antiferromagnetic, there is no polarization from the spin–filter effect even though there is Zeeman splitting in the superconductor from the field alignment of the Gd ions [179].

6. Relation to other techniques

Many different techniques have been used to study spin-polarized electrons emitted from solids. In this section we will mention some results from those techniques which are related to the tunneling results. Discussion of many of the techniques is also to be found in a book edited by Feder [180].

6.1. Field emission

In 1930 Fues and Hellman [181] suggested that application of a strong electric field to a ferromagnet should produce spin-polarized emitted electrons, but it was not until 1964 that Hofmann et al. [182] observed spin polarization in electrons field-emitted from Gd. The value of $P_{Gd} = +8\%$ agreed reasonably well with the theoretically predicted value [183]. Field emission measurements from Ni by Gleich et al. [184] found a maximum polarization of $+13\%$, whereas Müller [185] and Campagna and co-workers [186, 187] found polarization of less than 5% and of both signs. Measurements of Ni, Co, Fe, Gd, and other rare-earth metals and compounds made by Chrobok et al. [188] gave very different values of the electron spin polarization that were both positive and negative and often of large magnitude, and fitted no simple pattern. Measurements by Landolt and co-workers [187, 189] on Ni showed more consistent results and gave $P_{Ni}(100) = -3 \pm 1\%$, $P_{Ni}(110) = +5 \pm 2\%$, $P_{Fe}(100) = +25 \pm 5\%$, $P_{Fe}(111) = +20 \pm 5\%$, and $P_{Fe}(110) = -5 \pm 10\%$. These results are perhaps qualitatively understandable by the theoretical ideas that were applied to explain the tunneling results [190], but the analysis is complicated by the effect of the high electric field on the surface electronic structure. Field emission measurements from the Eu chalcogenide films on a metal tip gave high values of positive polarization [170, 171, 191].

6.2. Photoemission

Photoemission probes the electronic states in metals in a region about 1.2 nm from the surface and is thus less dependent on the final surface layer than field emission or tunneling. In 1969, the first photoemission experiment to observe spin-polarized electrons by Busch et al. [192] obtained a value of $P = +5.5\%$ for Gd. Shortly thereafter Banninger et al. [193] obtained a value of $P = +15.5\%$ for polycrystalline films of Ni. Busch et al. [194] measured the spin polarization of photoelectrons from Fe, Co, and Ni and found $P = +54$, $+21$, and $+15\%$, respectively. The value for Fe was in reasonable agreement with a simple band model. However, the value for Ni was puzzling because of the high density of states of minority spins at the Fermi energy. In 1976 Eib and

Alvarado [195], by increasing the sensitivity and the energy resolution, showed that very close to the threshold energy, a large preponderance of minority spins was found while at slightly higher energy P became positive. Qualitatively this measurement was as expected, but the results gave an exchange splitting of only about 0.33 eV that was smaller than expected from band theory calculations. This discrepancy has been explained as resulting from many-body interactions [196, 197]. For Fe and BCC Co the results of spin-polarized photoemission have been shown to agree reasonably well with single-particle band structure calculations. Recent photoemission technique with angle, energy, and spin resolution together with high-intensity light sources is a very powerful method of studying the band structure of the ferromagnets. The basic difference between photoemission and tunneling measurements seems to be that photoemission samples mainly the high density of states of localized bands in the 3d metals, whereas tunneling samples only the highly itinerant states. The agreement of the earlier results of photoemission and tunneling measurements of polarization was apparently coincidence. Reviews of spin-polarized photoemission studies are listed in ref. [198].

6.3. Electron capture spectroscopy

In electron capture spectroscopy 150 keV deuterium ions are reflected from a magnetic crystal at near the grazing angle. D^+ ions extract an electron during reflection from the surface and the spin of the electron is determined through the effect of the hyperfine interaction on a nuclear reaction. This technique was pioneered by Rau and Sizmann [199]. Details of the technique and many results are found in Rau's review article. [200]. The spin polarization of electrons captured from various crystal directions in Ni varied from $P = +15$ to -96%; for Co, $P = +33$ to -41%; for BCC Fe, $P = 31\%$ to 13%. These results have been interpreted as reflecting the tail of the wave function 0.2 nm outside the metal surface, but theoretical analysis is difficult because of the strong perturbations of the electronic system during the capture process. A variation of ECS uses two-electron capture, which detects local magnetic order rather than long-range order [200, 201]. Relative values of P versus temperature have been used to study phase transitions and fluctuations above T_c in ferromagnets.

6.4. Secondary electron emission

Unguris et al. [202] first demonstrated the detection of spin polarization of secondary electrons from a ferromagnet. Fe and Co were studied by Kisker et al. [203] and Ni by Hopster and others [204]. As a function of the energy of the emitted electrons, the spin polarization of the 3d metals is always positive, with a maximum value at the escape threshold energy and decreasing rapidly with increasing energy to a positive value which approximately reflects the average polarization of the bands for Fe, Co and Ni. At the threshold energy the experimental results are $P_{Fe} = +44 \pm 2\%$, $P_{Co} = +34 \pm 2\%$, and $P_{Ni} = +24 \pm 3\%$. Explanations of these results have been proposed in terms of a spin-dependent mean free path [205], the formation of Stoner excitations [206, 207], and the fact that the low-energy secondaries reflect the band structure near E_F [208]. It also has been suggested that the close agreement of the threshold polarizations of Fe, Co, and Ni with those measured by tunneling is the result of the highly mobile s–d electrons playing a dominant role in the transport of the emitted electrons to the surface [209]. Spin-polarized Auger electrons have the important property that the atom type from which the electrons originate can be identified [210]. Spin-polarized secondary electrons have been used to map magnetic domains with high resolution [211]. A related but different technique

is that of measuring the spin polarization of electrons scattered from surfaces and has been reviewed by Pierce and Celotta [212].

6.5. *Spin-polarized metastable-atom de-excitation spectroscopy*

SPMDS is a technique originated by Onellion et al. [213] in which spin-polarized metastable thermal-energy He(2^3s) atoms incident on a ferromagnetic metal surface eject secondary electrons by an Auger process. Changing the spin direction of the incident metastable atom with respect to the magnetization direction of the ferromagnet results in a change in the number of secondary electrons. A theory by Penn and Apell [214] when applied to the data on Ni (110) gave a value of spin polarization of -20% for the highest-energy secondaries that resulted from Auger neutralization at positions about 0.45 nm outside the metal. Hammond et al. [215] have added the use of a direct measurement of the polarization of the secondary electrons with a Mott detector and give results on an Fe (110) surface with and without oxygen contamination and discuss the analysis of results in detail. Results for Fe (110) can also be compared with the theoretical calculations of the density of states at E_F by Wu and Freeman [216]. SPMDS is a promising technique that is confined to the surface more than photoemission, but the complexity of the interactions and the large perturbation expected from an ion close to a metal surface make the interpretation of the results difficult. Whether the results are closely related to those obtained by tunneling is not clear at present.

6.6. *Photodetection of injected electron spins*

Alvarado and Renaud [217] have recently reported the result of measuring the spin polarization of electrons injected from a Ni tip into GaAs whose optical output acts as a spin detector. The spin polarization found for the field-emitted electrons at 0.3 V was $P = -31 \pm 5.6\%$. These results demonstrate the feasibility of this attractive technique of spin detection [218].

7. Summary

Spin-polarized electron tunneling is a technique that provides information about spin-dependent properties of superconductors, normal metals and ferromagnets at energies close to the Fermi energy. In addition to furnishing quantitative tests of theories concerning the density of states and critical magnetic field of superconductors, this method allows measurement of normal-state properties such as spin–orbit scattering rates and Fermi-liquid corrections to the electron spin magnetic moment which are difficult to determine by other experimental techniques. In addition, the consequences of the exchange interaction between magnetic ions and conduction electrons are shown in a very graphic way by tunneling experiments. The effective magnetic field is evident in the extra splitting of the density of states. The broadening of the BCS density-of-states peak measures the exchange scattering rate. Spin polarization due to the RKKY interaction can also be observed directly in the tunneling conductance. The spin-filter effect demonstrates quantitatively the effect of the exchange splitting of the barrier material on the tunneling current and also provides a source of highly polarized electrons. The application of spin-polarized tunneling to ferromagnetic metals uniquely yields quantitative information about the polarization of the conduction electrons very close to the Fermi surface in these materials. The application of this information to the case of ferromagnetic–ferromagnetic tunneling remains an uncompleted task from both experimental and

theoretical points of view. We hope that this overview demonstrates both the power of the tunneling technique and the transparent simplicity of interpreting the results of such measurements.

8. Future directions

Experimental results of tunneling from ferromagnets to superconductors are incomplete. Measurements using vacuum tunneling in the different crystal directions of ferromagnetic metals with well characterized surfaces should clarify the experimental situation. Ferromagnetic–ferromagnetic tunneling is an outstanding problem both experimentally and theoretically. Here again, vacuum tunneling and fabrication of planar tunnel junctions with modern epitaxial techniques promise experimental advances in this field. With more detailed experimental results in ferromagnetism, theorists may turn more attention to this field.

For superconductors, the whole areas of high-T_c and heavy-fermion materials remain to be explored, and here again progress will rely on improved junction formation or vacuum tunneling. Another interesting area that has not been addressed as yet is the spin dependence of non-equilibrium effects; for instance, how the recombination time is affected by non-equilibrium spin distributions. In addition, spin-filter sources of spin-polarized tunnel currents can be used in non-equilibrium studies of normal metals and semiconductors.

In a more general way, recent technical advances are leading to greatly broadened possibilities in spin-polarized tunneling. The scanning tunneling microscope [219] has allowed the study of topography and spectroscopy on an atomic scale at the surface of solids. Recently, spin-polarized vacuum tunneling was shown to be possible at room temperatures [137] and, more recently, atomic resolution of magnetic structures has been demonstrated [139, 140]. It appears that spin-polarized electron tunneling can be applied to solid surfaces with atomic resolution as a function of energy, magnetic field, temperature, and crystal direction. These developments should lead to many scientific advances in surface science, magnetism, solid state studies, and tunneling.

Acknowledgements

During the nearly twenty-five years of this experimental program, many people have contributed to its development. The authors are particularly grateful to Mr. Richard MacNabb, who made nearly all of the junctions described here, and Mr. Michael Blaho, who maintained the experimental equipment throughout most of the program. On theoretical issues, we have received excellent help and advice from B.B. Schwartz, P. Fulde, H. Engler, R. Bruno, K. Aoi, W. Gallagher, M.B. Stearns, and D. Rainer. The contributions of Dr. J.S. Moodera have been essential. The breadth of the program has been enormously enhanced by a series of very talented students: D. Paraskevopoulos, J.A.X. Alexander, J.E. Tkaczyk, X. Hao, G. Gibson, A. Kussmaul, G. Roesler and R. Kabani, and postdoctoral fellows V. Kalvey and M. Taylor. We also profited from a collaboration with professor T. Orlando. The assistance and tolerance of M. O'Meara and the rest of the staff of the Francis Bitter National Magnet Laboratory have been exemplary. Finally, we thank the NSF, DOE, AFOSR, ONR and CSE for their financial support.

References

[1] P. Fulde, Adv. Phys. 22 (1973) 667.
[2] E.L. Wolf, Principles of Tunneling Spectroscopy (Clarendon Press, Oxford, 1985).
[3] E. Burstein and S. Lundqvist (eds.), Tunneling Phenomena in Solids (Plenum Press, New York, 1969).
[4] C.B. Duke, Tunneling in solids, Solid State Physics (Suppl.) 10 (Academic Press, New York, 1969).
[5] M. Tinkham, Introduction to Superconductivity (McGraw-Hill, New York, 1975); reprinted (Krieger, New York, 1980).
[6] G. Rickayzen, Theory of Superconductivity (Wiley, New York, 1965).
[7] P.G. de Gennes, Superconductivity of Metals and Alloys (Benjamin, New York, 1966).
[8] J.R. Schrieffer, Theory of Superconductivity (Benjamin, New York, 1964).
[9] R. Parks (ed.), Superconductivity (Marcel Dekker, New York, 1969).
[10] L. Solymar, Superconductive Tunnelling and Applications (Wiley, New York, 1972).
[11] T. Van Duzer and O. Turner, Principles of Superconductive Devices and Circuits (Elsevier, New York, 1981).
[12] K.A. Delin and T.P. Orlando, Foundations of Applied Superconductivity (Addison-Wesley, Reading, MA, 1991).
[13] J. Bardeen, L.N. Cooper and J.R. Schrieffer, Phys. Rev. 108 (1957) 1175.
[14] V.L. Ginzburg and L.D. Landau, Zh. Eksp. Teor. Fiz. 20 (1950) 1064.
[15] W. Meissner and R. Ochsenfeld, Naturwissenschaften 21 (1933) 787.
[16] I. Giaever, Phys. Rev. Lett. 5 (1960) 147,464; I. Giaever and K. Megerle, Phys. Rev. 122 (1961) 110; I. Giaever, H. Hart and K. Megerle, Phys. Rev. 126 (1962) 941; D.H. Douglass Jr. and L.M. Falicov, in: Progress in Low Temperature Physics 4, ed. C.J. Gorter (North-Holland, Amsterdam, 1964) p. 97.
[17] S. Shapiro, P.H. Smith, J. Nicol, J.L. Miles and P.F. Strong, IMB J. Res. Dev. 6 (1962) 34.
[18] J. Bardeen, Phys. Rev. Lett. 6 (1961) 57.
[19] H. Engler, Z. Naturf. 26A (1971) 1763.
[20] D.A. Rudman and M.R. Beasley, Appl. Phys. Lett. 36 (1980) 1010.
[21] J.S. Moodera, R. Meservey and P.M. Tedrow, Appl. Phys. Lett. 41 (1982) 488.
[22] R.V. Coleman, R.C. Mooris and J.E. Christopher, in: Methods of Experimental Physics, Vol. 11 (Academic Press, New York, 1974) p. 123.
[23] K. Yosida, Phys. Rev. 110 (1958) 769.
[24] F. Reif, Phys. Rev. 106 (1957) 208.
[25] G.M. Androes and W.D. Knight, Phys. Rev. 121 (1961) 779.
[26] A.M. Clogston, Phys. Rev. Lett. 9 (1962) 266.
[27] B.S. Chandrasekhar, Appl. Phys. Lett. 1 (1962) 7.
[28] R.A. Ferrell, Phys. Rev. Lett. 3 (1959) 262.
[29] P.W. Anderson, Phys. Rev. Lett. 3 (1959) 325.
[30] A.A. Abrikosov and L.P. Gor'kov, Zh. Eksp. Teor. Fiz. 42 (1962) 1088; Sov. Phys. JETP 15 (1962).
[31] K. Maki, Physics 1 (1964) 127; Phys. Rev. 148 (1966) 362.
[32] N.R. Werthamer, E. Helfand and P.C. Hohenberg, Phys. Rev. 147 (1966) 295.
[33] R. Hammond and G.M. Kelly, Phys. Rev. Lett. 18 (1967) 156.
[34] H.L. Fine, M. Lipsicas and M. Strongin, Phys. Lett. A 29 (1969) 366.
[35] R. Meservey and P.M. Tedrow, J. Appl. Phys. 42 (1971) 51; P.M. Tedrow and R. Meservey, Phys. Rev. B 8 (1973) 5098.
[36] A.F. Mayadas and M. Shatzkes, Phys. Rev. B 1 (1970) 1382; O.A.E. Cherney and J. Shewchun, Can. J. Phys. 47 (1969) 1101.
[37] M. Strongin and O.F. Kammerer, Phys. Rev. Lett. 16 (1966) 456.
[38] R. Meservey and P.M. Tedrow, Phys. Rev. Lett. 41 (1978) 805.
[39] K. Maki, in: Superconductivity, ed. R. Parks (Marcel Dekker, New York, 1969) ch. 18.
[40] P. Fulde, in: Superconductivity, ed. R. Parks (Marcel Dekker, New York, 1969) ch. 29.
[41] G. Sarma, J. Phys. Chem. Sol. 24 (1963) 1029.
[42] K. Maki and T. Tsuneto, Progr. Theor. Phys. 31 (1964) 945.
[43] K. Maki, Progr. Theor. Phys. 32 (1964) 29.
[44] S. Frota-Pessoa and B.B. Schwartz, Solid State Commun. 20 (1976) 505.
[45] P.M. Tedrow, R. Meservey and B.B. Schwartz, Phys. Rev. Lett. 24 (1970) 1004.
[46] T. Suzuki, T. Tsuboi, H. Takaki, T. Mizusaki and T. Kusumoto, J. Phys. Soc. Japan 52 (1983) 981.
[47] A.L. Fetter and P.C. Hohenberg, in: Superconductivity, ed. R. Parks (Marcel Dekker, New York, 1969) p. 817.
[48] H. Engler and P. Fulde, Z. Phys. 247 (1971) 1; Phys. Kondens. Mater. 7 (1968) 150.
[49] H. Engler, J. Phys. F 3 (1973) L86.
[50] R.C. Bruno and B.B. Schwartz, Phys. Rev. B 8 (1973) 3161.
[51] R.R. Hake, Phys. Rev. 158 (1967) 356.
[52] L.J. Neuringer and Y. Shapira, Phys. Rev. Lett. 17 (1966) 81.
[53] K. Aoi, R. Meservey and P.M. Tedrow, Phys. Rev. B 9 (1974) 875 and references therein.
[54] D.H. Douglass Jr., Phys. Rev. Lett. 7 (1961) 14.
[55] L.G. Aslamazov and A.I. Larkin, Phys. Lett. A 26 (1968) 238; Fiz. Tverd. Tela 10 (1968) 1104; Sov. Phys.-Solid State 10 (1968) 875.

[56] K. Maki, J. Low Temp. Phys. 1 (1969) 513.
[57] K. Maki, Progr. Theor. Phys. 40 (1968) 193.
[58] R.S. Thompson, Phys. Rev. B 1 (1970) 327.
[59] P. Fulde and K. Maki, Z. Phys. 238 (1970) 233.
[60] P.M. Tedrow and R. Meservey, Phys. Lett. 63A (1977) 398; P.M. Tedrow and R. Meservey, Phys. Rev. B 16 (1977) 4825; P. Fulde and R.O. Ferrell, Phys. Rev. 135 (1969) A550.
[61] R. Meservey, P.M. Tedrow and P. Fulde, Phys. Rev. Lett. 25 (1970) 1270.
[62] R. Meservey, P.M. Tedrow and R.C. Bruno, Phys. Rev. B 11 (1975) 4224.
[63] P.M. Tedrow and R. Meservey, Solid State Commun. 27 (1978) 1397; Phys. Lett. A 69 (1978) 285.
[64] The Maki theory was used in obtaining the spin scattering rate from the superconducting data, K. Maki in: Superconductivity, ed. R. Parks (Marcel Dekker, New York, 1969) p. 1035; Phys. Rev. 148 (1966) 362.
[65] W.J. Gallagher, Ph.D. Thesis, Massachusetts Institute of Technology (1978) unpublished.
[66] P.M. Tedrow and R. Meservey, Phys. Rev. B 25 (1982) 171.
[67] P.M. Tedrow and R. Meservey, Phys. Rev. Lett. 43 (1979) 384.
[68] T.P. Orlando and M.R. Beasley, Phys. Rev. Lett. 46 (1981) 1598.
[69] T.P. Orlando, E.J. McNiff Jr., S. Foner and M.R. Beasley, Phys. Rev. B 19 (1979) 4543.
[70] D. Rainer, private communication, 1978.
[71] P.M. Tedrow and R. Meservey, Phys. Lett. 58A (1976) 237.
[72] R. Meservey, in: Low Temperature Physics-LT13, Vol. 13, eds K.D. Timmerhaus, W.J. O'Sullivan and E.J. Hammel (Plenum, New York, 1974) p. 345.
[73] G.A. Gibson and R. Meservey, Phys. Rev. B 40 (1989) 8705.
[74] P.M. Tedrow and R. Meservey, Solid State Commun. 27 (1978) 1397.
[75] S.J. Bending, M.R. Beasley and C.C. Tsuei, Phys. Rev. B 30 (1984) 6342.
[76] P.M. Tedrow and R. Meservey, Proc. 17th Int. Low Temperature Conf., eds V. Eckern, A. Schmid, N. Weber and H. Wuhl (Elsevier, Amsterdam, 1984) p. 837.
[77] P.M. Tedrow and R. Meservey, Phys. Letters 51A (1975) 57; R. Meservey, P.M. Tedrow and R.C. Bruno, Phys. Rev. B 17 (1978) 2915; G.A. Gibson, P.M. Tedrow and R. Meservey, Phys. Rev. B 40 (1989) 137.
[78] G. Roesler, P.M. Tedrow, E.S. Hellman and E.H. Hartford, IEEE Trans. Appl. Superconductivity 3 (1993) 1280.
[79] J.E. Tkaczyk, Ph.D. Thesis, Massachusetts Institute of Technology (1988) unpublished.
[80] P.M. Tedrow and R. Meservey, Phys. Rev. Lett. 27 (1971) 919.
[81] R.R. Hake, Appl. Phys. Lett. 10 (1967) 189; M.R. Beasley, in: Advances in Cryogenic Engineering (Materials) Vol. 28, eds R.P. Reed and A.F. Clark (Plenum, New York, 1982) p. 345.
[82] P.M. Tedrow and J.E. Tkaczyk, IEEE Trans. Magn. MAG-21 (1985) 1144.
[83] Y. Yafet, Solid State Phys. 14 (1963) 1.
[84] A.R. Mackintosh and O.K. Anderson, in: Electrons at the Fermi Surface, ed. M. Springford (Cambridge University Press, New York, 1980).
[85] G. Bergmann, Phys. Rep. 107 (1984) 1 and references therein.
[86] J.A.X. Alexander, P.M. Tedrow and T.P. Orlando, Phys. Rev. B 34 (1986) 8157.
[87] P.M. Tedrow and R. Meservey, Phys. Rev. B 8 (1973) 5098.
[88] G. Bergmann, Phys. Rev. B 28 (1983) 2914.
[89] S. Geier and G. Bergmann, Phys. Rev. Lett. 68 (1992) 2520; N. Papanikolaou, N. Stefanov, P.H. Dedericks, S. Geier and G. Bergmann, Phys. Rev. Lett. 69 (1992) 2110.
[90] Adapted from L. Hodges, H. Ehrenreich and N.D. Lang, Phys. Rev. 152 (1966) 505.
[91] P.M. Tedrow and R. Meservey, Phys. Rev. Lett. 26 (1971) 192.
[92] P.M. Tedrow and R. Meservey, Phys. Rev. B 7 (1973) 318.
[93] R. Meservey and P.M. Tedrow, Solid State Commun. 11 (1972) 333.
[94] R. Meservey, P.M. Tedrow and J.S. Moodera, J. Magn. Magn. Mater. 35 (1983) 1.
[95] R. Meservey, Phys. Scripta 38 (1988) 272.
[96] J.S. Rogers, private communication, 1978.
[97] J. Akimitsu, R. Kai and N. Kitamura, Solid State Commun. 48 (1983) 817.
[98] P.M. Tedrow, J.S. Moodera and R. Meservey, Solid State Commun. 44 (1982) 587.
[99] J.S. Rogers and P.C. Sullivan, Solid State Commun. 28 (1978) 397.
[100] D. Paraskevopoulos, R. Meservey and P.M. Tedrow, Phys. Rev. B 16 (1977) 4907.
[101] J.A.X. Alexander, T.P. Orlando, D. Rainer and P.M. Tedrow, Phys. Rev. B 31 (1985) 5811.
[102] R.M. Bozorth, Ferromagnetism (Van Nostrand, New York, 1950) p. 109 and references therein.
[103] P.C. Sullivan and J.S. Rogers, Solid State Commun. 45 (1983) 977.
[104] J.W. Gadzuk, Phys. Rev. 182 (1969) 416; B.A. Politzer and P.H. Cutler, Phys. Rev. Lett. 28 (1972) 1330.
[105] J.A. Hertz and K. Aoi, Phys. Rev. B 8 (1973) 3252.
[106] J.-N. Chazalviel and Y. Yafet, Phys. Rev. B 15 (1977) 1062.
[107] M.B. Stearns, J. Magn. Magn. Mater. 5 (1977) 167.

[108] W.A. Harrison, Phys. Rev. 123 (1961) 85.
[109] M.A. Ruderman and C. Kittel, Phys. Rev. 96 (1954) 99; T. Kasuya, Theoret. Phys. (Kyoto) 16 (1956) 45; K. Yosida, Phys. Rev. 106 (1957) 893.
[110] J. Callaway and C.S. Wang, Phys. Rev. B 16 (1977) 2095.
[111] D.R. Baraff, Phys. Rev. B 8 (1973) 3439.
[112] A.V. Gold, L. Hodges, P.T. Panousis and D.R. Stone, Int. J. Magn. 2 (1971) 357.
[113] R. Meservey, D. Paraskevopoulos and P.M. Tedrow, Phys. Rev. B 22 (1980) 1331.
[114] L.N. Liebermann, D.R. Fredkin and H.B. Shore, Phys. Rev. Lett. 22 (1969) 539.
[115] L.N. Leibermann, J. Clinton, D.M. Edwards and J. Mathon, Phys. Rev. Lett. 25 (1970) 232.
[116] T. Shinjo, T. Matsuzawa, T. Takada, S. Nasu and Y. Murakami, J. Phys. Soc. Japan 35 (1973) 1032; Phys. Lett. 36A (1971) 489.
[117] D.T. Pierce and H.C. Siegmann, Phys. Rev. B 9 (1974) 4035.
[118] P.M. Tedrow and R. Meservey, Solid State Commun. 16 (1975) 71.
[119] G. Bergmann, Phys. Rev. Lett. 41 (1978) 264.
[120] R. Meservey, P.M. Tedrow and V.R. Kalvey, Solid State Commun. 36 (1980) 969; J. Appl. Phys. 52 (1981) 1617; see also ref. [94].
[121] J.S. Moodera and R. Meservey, Phys. Rev. B 29 (1984) 2943.
[122] P.M. Tedrow and J.E. Tkaczyk, unpublished.
[123] G. Bergmann, J. Magn. Magn. Mater. 35 (1983) 68.
[124] J. Tersoff and L.M. Falicov, Phys. Rev. B 26 (1982) 6186.
[125] B.N. Cox, R.A. Tahir-Kheli and R.J. Elliott, Phys. Rev. B 20 (1979) 2864.
[126] R. Meservey, P.M. Tedrow, V.R. Kalvey and D. Paraskevopoulos, J. Appl. Phys. 50 (1979) 1935.
[127] M. Julliere, Phys. Lett. 54A (1975) 225.
[128] S. Maekawa and D. Gäfvert, IEEE Trans. Magn. 18 (1982) 707.
[129] R. Kabani, J.S. Moodera and R. Meservey (1990) unpublished.
[130] R. Meservey, P.M. Tedrow and J.S. Brooks, J. Appl. Phys. 53 (1982) 1563; G.A. Gibson and R. Meservey, J. Appl. Phys. 58 (1985) 1584.
[131] Y. Suezawa and Y. Gondo, in: Proc. Int. Symp. on Physics of Magnetic Materials, eds M. Takahashi, S. Maekawa, Y. Gondo and H. Nose (World Scientific, Singapore, 1987) p. 303.
[132] R. Kabani, J.S. Moodera, P.M. Tedrow and R. Meservey, Materials Research Society Proc. Symp. B (1990) 177.
[133] D. Paraskevopoulos and R. Meservey (1975) unpublished.
[134] J.G. Adler and T.T. Chen, Solid State Commun. 9 (1971) 501; D.C. Tsui, R.E. Dietz and L.R. Walker, Phys. Rev. Lett. 27 (1971) 1729.
[135] J. Nowak and J. Rauluszkiewicz, J. Magn. Magn. Mater. 109 (1992) 79.
[136] M. Johnson and J. Clarke, J. Appl. Phys. 67 (1990) 6141.
[137] R. Wiesendanger, H.-J. Güntherodt, G. Güntherodt, R.J. Gambino and R. Ruf, Phys. Rev. Lett. 65 (1990) 247.
[138] R. Wiesendanger, D. Bürgler, G. Tarrach, A. Wadas, D. Brodbeck, H.-J. Güntherodt, G. Güntherodt, R.J. Gambino and R. Ruf, J. Vac. Sci. Technol. B 9 (1991) 519.
[139] K.P. Kämper, W. Schmitt, G. Güntherodt, R.J. Gambino and R. Ruf, Phys. Rev. Lett. 59 (1987) 2788.
[140] R. Wiesendanger, D. Bürgler, G. Tarrach, T. Schaub, U. Hartmann, H.-J. Güntherodt, I.V. Shvets and J.M.D. Coey, Appl. Phys. A 53 (1991) 349.
[141] R. Wiesendanger, I.V. Shvets, D. Bürgler, G. Tarrach, H.-J. Güntherodt and J.M.D. Coey, Z. Phys. B Cond. Matter. 86 (1992) 1; J. Appl. Phys. 71 (1992) 5489.
[142] J.C. Slonczewski, Phys. Rev. B 39 (1989) 6995.
[143] J.C. Slonczewski, Symp. on Magnetism and Magnetic Materials, eds H.L. Huang and P.C. Kuo (World Scientific, Singapore, 1990) p. 285.
[144] P.M. Tedrow, J.T. Kucera, D. Rainer and T.P. Orlando, Phys. Rev. Lett. 52 (1984) 1637.
[145] J.A.X. Alexander, Ph.D. Thesis, Massachusetts Institute of Technology (1986) unpublished.
[146] G.A. Gibson, P.M. Tedrow and R. Meservey, Phys. Rev. B 40 (1989) 137.
[147] W. Bückel and R. Hilsch, Z. Phys. 138 (1954) 109.
[148] G.V. Minnigerode and J. Rothenberg, Z. Phys. 213 (1968) 397; [146] and references therein.
[149] P.M. Tedrow and R. Meservey, Phys. Lett. 51A (1975) 57.
[150] A.A. Abrikosov and L.P. Gor'kov, Zh. Eksp. Teor. Fiz. 39 (1960) 1781; Sov. Phys. JETP 12 (1961) 1242.
[151] S. Skalski, O. Betbedev-Matibet and P.R. Weiss, Phys. Rev. 136 (1964) A1500; P. Fulde and K. Maki, Phys. Rev. 141 (1966) 275; K. Maki, in: Superconductivity, ed. R. Parks (Marcel Dekker, New York, 1969) ch. 18.
[152] D.E. Moncton, D.B. McWhan, P.H. Schmidt, G. Shirane, W. Thomlinson, M.B. Maple, H.B. MacKay, L.D. Woolf, Z. Fisk and D.C. Johnston, Phys. Rev. Lett. 45 (1980) 2060; S.K. Sinha, G.W. Crabtree, D.G. Hinks and H. Mook, Phys. Rev. Lett. 48 (1982) 950.
[153] H.W. Meul, C. Rossel, M. De Croux, Ø. Fischer, G. Remanyi and A. Briggs, Phys. Rev. Lett. 53 (1984) 497; Ø. Fischer, H.W. Meul, M.G. Karkut, G. Remanyi, U. Welp, J.C. Piccoche and K. Maki, Phys. Rev. Lett. 55 (1985) 2972; J.W. Lynn, J.A. Gotaas, R.W. Erwin, R.A. Ferrell, J.K. Bhattacharjee, R.N. Shelton and P. Klavins, Phys. Rev. Lett. 52 (1984) 133; J.W. Lynn, G. Shirane, W. Thomlinson and R.N. Shelton, Phys. Rev. Lett. 46 (1981) 368.

[154] C.L. Lin, J. Teeter, J.E. Crow, T. Mihalisin, J. Brooks, A.I. Abou-Aly and G.R. Stewart, Phys. Rev. Lett. 54 (1985) 2541.
[155] F. Stageberg, R. Cantor, A.M. Goldman and G.B. Arnold, Phys. Rev. B 32 (1985) 3292.
[156] P.M. Tedrow, J.E. Tkaczyk and A. Kumar, Phys. Rev. Lett. 56 (1986) 1746.
[157] P.G. de Gennes, Phys. Lett. 23 (1966) 10.
[158] J.E. Tkaczyk and P.M. Tedrow, J. Appl. Phys. 61 (1987) 3368.
[159] X. Hao, J.S. Moodera and R. Meservey, Phys. Rev. B 42 (1990) 8235.
[160] T. Tokuyasu, J.A. Sauls and D. Rainer, Phys. Rev. B 38 (1988) 8823.
[161] J.S. Moodera, X. Hao, G.A. Gibson and R. Meservey, Phys. Rev. Lett. 61 (1988) 637.
[162] F. Reif and M.A. Woolf, Phys. Rev. Lett. 9 (1962) 315; M.A. Woolf and F. Reif, Phys. Rev. 137 (1965) A557.
[163] M.B. Maple, Appl. Phys. 9 (1976) 179; M.B. Maple, in: Magnetism: A Treatise on Modern Theory and Materials, Vol. V ed. H. Suhl (Academic Press, New York, 1973) ch. 10; C. Rizzuto, Rep. Prog. Phys. 37 (1974) 147.
[164] J.E. Tkaczyk and P.M. Tedrow, Phys. Rev. Lett. 61 (1988) 1253.
[165] J.E. Tkaczyk and P.M. Tedrow, Phys. Rev. 46 (1992) 8344.
[166] J.S. Moodera, M.E. Taylor and R. Meservey, Phys. Rev. B 40 (1989) 11980.
[167] W.J. Gallagher, Ph.D. Thesis, Massachusetts Institute of Technology (1978) unpublished; W.J. Gallagher, D.E. Paraskevopoulos, P.M. Tedrow, S. Frota-Pessoa and B.B. Schwartz, Phys. Rev. B 21 (1980) 962.
[168] L. Esaki, P.J. Stiles and S. von Molnar, Phys. Rev. Lett. 19 (1967) 852.
[169] W.A. Thompson, F. Holtzberg, T.R. McGuire and G. Petrich, in: Magnetism and Magnetic Materials (Chicago, 1971), Proc. 17th Annual Conf. Magnetism and Magnetic Materials, AIP Conf. Proc. No. 5, eds C.D. Graham Jr. and J.J. Rhyne (AIP, New York, 1972) p. 827.
[170] N. Müller, W. Eckstein, W. Heiland and W. Zinn, Phys. Rev. Lett. 29 (1972) 1651.
[171] E. Kisker, G. Baum, A.H. Mahan, W. Raith and K. Schröder, Phys. Rev. Lett. 36 (1976) 982; E. Kisker, G. Baum, A.H. Mahan, W. Raith and B. Reihl, Phys. Rev. B 18 (1978) 2256.
[172] X. Hao, Ph.D. Thesis, Massachusetts Institute of Technology (1990) unpublished.
[173] J.G. Simmons, J. Appl. Phys. 34 (1963) 1793.
[174] P. Wachter, CRC Crit. Rev. Solid State Sci. 3 (1972) 189.
[175] S.M. Sze, Physics of Semiconductor Devices, 2nd Ed. (Wiley, New York, 1981) p. 396.
[176] D.E. Eastman, F. Holtzberg and S. Methfessel, Phys. Rev. Lett. 23 (1969) 226.
[177] X. Hao, J.S. Moodera and R. Meservey, Phys. Rev. Lett. 67 (1991) 1342.
[178] R. Griessen, M. Landolt and H.R. Ott, Solid State Commun. 9 (1961) 2219.
[179] J.S. Moodera and R. Meservey, Phys. Rev. Lett. 70 (1993) 853.
[180] R. Feder (ed.), Polarized Electrons in Surface Physics, (World Scientific, Singapore, 1985).
[181] E. Fues and H. Hellmann, Z. Phys. 31 (1930) 465.
[182] M. Hofmann, G. Regenfus, O. Schärpf and P.J. Kennedy, Phys. Lett. 25 (1967) 270.
[183] N. Müller, H. Chr. Siegmann and G. Obermair, Phys. Lett. 24A (1967) 733.
[184] W. Gleich, R. Regenfus and R. Sizmann, Phys. Rev. Lett. 27 (1971) 1066.
[185] N. Müller, Phys. Lett. 54A (1975) 415.
[186] M. Campagna, T. Utsumi and D.N.E. Buchanan, J. Vac. Sci. Technol. 13 (1976) 193.
[187] M. Landolt and M. Campagna, Phys. Rev. Lett. 38 (1977) 663.
[188] G. Chrobok, M. Hofmann, G. Regenfus and R. Sizmann, Phys. Rev. B 15 (1977) 429.
[189] M. Landolt and Y. Yafet, Phys. Rev. Lett. 40 (1978) 1401.
[190] J.-N. Chazalviel and Y. Yafet, Phys. Rev. B 15 (1977) 1062.
[191] G. Chrobok and M. Hofmann, Phys. Lett. 57A (1976) 257.
[192] G. Busch, M. Campagna, P. Cotti and H.C. Siegmann, Phys. Rev. Lett. 22 (1969) 597.
[193] U. Bänninger, G. Busch, M. Campagna and H.C. Siegmann, Phys. Rev. Lett. 25 (1970) 585.
[194] G. Busch, M. Campagna and H.C. Siegmann, Phys. Rev. B 4 (1971) 746.
[195] W. Eib and S.F. Alvarado, Phys. Rev. Lett. 37 (1976) 444.
[196] P.W. Anderson, Philos. Magn. 24 (1971) 203.
[197] D.M. Edwards and J.A. Hertz, J. Phys. F 3 (1973) 2191.
[198] H.C. Siegmann, Phys. Rep. 17 (1975) 37; M. Campagna, D.T. Pierce, F. Meier, K. Sattler and H.C. Siegmann, Adv. Electron. Electron. Phys. 41 (1976) 113; H.C. Siegmann, F. Meier, M. Erbudak and M. Landolt, Adv. Electron. Electron. Phys. 62 (1984) 1; J. Kirschner, in: Polarized Electrons at Surfaces, Springer Trans. Modern Physics, Vol. 106 (Springer, Heidelberg, 1985); R. Feder ed. Polarized Electrons in Surface Physics, (World Scientific, Singapore, 1985).
[199] C. Rau and R. Sizmann, Phys. Lett. 34A (1973) 317.
[200] C. Rau, J. Magn. Magn. Mater. 31 (1982) 141.
[201] C. Rau, Appl. Phys. A 49 (1989) 579.
[202] J. Unguris, D.T. Pierce, A. Galejs and R.J. Cellota, Phys. Rev. Lett. 49 (1982) 72.
[203] E. Kisker, W. Gadat and K. Schröder, Solid State Commun. 44 (1982) 591.
[204] H. Hopster, R. Raue, E. Kisker, G. Güntherodt and M. Campagna, Phys. Rev. Lett. 50 (1983) 71; D.L. Abraham and H. Hopster, Phys. Rev. Lett. 58 (1987) 1352.

[205] D.R. Penn, S.P. Apell and S.M. Girvin, Phys. Rev. B 32 (1985) 7753.
[206] J. Glazer and E. Tosatti, Solid State Commun. 52 (1984) 905.
[207] J. Kirschner, in: Polarized Electrons in Surface Physics, ed. R. Feder (World Scientific, Singapore, 1985) p. 353.
[208] D. Mauri, Ph.D. Thesis, ETH, Zurich (1984) unpublished.
[209] R. Meservey, J. Appl. Phys. 61 (1987) 3709.
[210] M. Landolt, in: Polarized Electrons in Surface Physics, ed. R. Feder (World Scientific, Singapore, 1985) p. 385.
[211] J. Unguris, G. Hambree, R.J. Celotta and D.T. Pierce, J. Magn. Magn. Mater. 54–57 (1986) 1629 and references therein.
[212] D.T. Pierce and R.J. Celotta, Adv. Electron. Electron. Phys. 56 (1981) 219.
[213] M. Onellion, M.W. Hart, F.B. Dunning and G.K. Walters, Phys. Rev. Lett. 52 (1984) 380.
[214] D.R. Penn and P. Apell, Phys. Rev. B 41 (1990) 3303.
[215] M.S. Hammond, F.B. Dunning and G.K. Walters, Phys. Rev. B 45 (1992) 3674.
[216] R. Wu and A.J. Freeman, Phys. Rev. Lett. 69 (1992) 2867.
[217] S.F. Alvarado and P. Renaud, Phys. Rev. Lett. 68 (1992) 1387.
[218] D.R. Scifres, B.A. Huberman, R.M. White and R.S. Bauer, Solid State Commun. 13 (1973) 1615.
[219] G. Binnig, H. Rohrer, Ch. Gerber and E. Weibel, Phys. Rev. Lett. 49 (1982) 57.